New high-sensitivity searches for neutrons converting into antineutrons and/or sterile neutrons at the HIBEAM/NNBAR experiment at the

OPEN ACCESS
IOP Publishing
Journal of Physics G: Nuclear and Particle Physics
J. Phys. G: Nucl. Part. Phys. **48** (2021) 070501 (76pp)
https://doi.org/10.1088/1361-6471/abf429

Major Report

New high-sensitivity searches for neutrons converting into antineutrons and/or sterile neutrons at the HIBEAM/NNBAR experiment at the European Spallation Source

A Addazi[1,2], K Anderson[7], S Ansell[8], K S Babu[9], J L Barrow[10], D V Baxter[11,12,13], P M Bentley[14], Z Berezhiani[15,16], R Bevilacqua[14], R Biondi[15], C Bohm[17], G Brooijmans[17], L J Broussard[7], J Cedercäll[18], C Crawford[19], P S B Dev[20], D D DiJulio[14], A D Dolgov[21,22], K Dunne[17], P Fierlinger[3], M R Fitzsimmons[10], A Fomin[23], M J Frost[7], S Gardiner[7], S Gardner[19], A Galindo-Uribarri[7], P Geltenbort[24], S Girmohanta[4], P Golubev[18], E Golubeva[25], G L Greene[10], T Greenshaw[26], V Gudkov[27], R Hall-Wilton[14], L Heilbronn[10], J Herrero-Garcia[28], A Holley[29], G Ichikawa[30], T M Ito[31], E Iverson[7], T Johansson[32], L Jönsson[32], Y-J Jwa[17], Y Kamyshkov[10], K Kanaki[14], E Kearns[33], Z Kokai[14], B Kerbikov[34,35,36], M Kitaguchi[37], T Kittelmann[14], E Klinkby[38], A Kobakhidze[39], L W Koerner[40], B Kopeliovich[22], A Kozela[41], V Kudryavtsev[42], A Kupsc[31], Y T Lee[14], M Lindroos[14], J Makkinje[43], J I Marquez[14], B Meirose[17,18], T M Miller[14], D Milstead[17,*], R N Mohapatra[44], T Morishima[36], G Muhrer[14], H P Mumm[45], K Nagamoto[36], A Nepomuceno[46], F Nesti[16], V V Nesvizhevsky[24], T Nilsson[47], A Oskarsson[18], E Paryev[25], R W Pattie Jr[48], S Penttil[7], H Perrey[18], Y N Pokotilovski[18], I Potashnikovav[40], K Ramic[14], C Redding[49], J-M Richard[50], D Ries[51], E Rinaldi[52,53], N Rizzi[37], N Rossi[15], A Ruggles[49], B Rybolt[54], V Santoro[14], U Sarkar[55], A Saunders[14], G Senjanovic[56,57], A P Serebrov[23], H M Shimizu[36], R Shrock[4], S Silverstein[17], D Silvermyr[18], W M Snow[11,12,13],

[*]Author to whom any correspondence should be addressed.

A Takibayev[14], I Tkachev[25], L Townsend[58], A Tureanu[59], L Varriano[60], A Vainshtein[61,62], J de Vries[63,64], R Wagner[24], R Woracek[14], Y Yamagata[65], S Yiu[17], A R Young[66], L Zanini[14], Z Zhang[67] and O Zimmer[24]

[1] Center for Theoretical Physics, College of Physics Science and Technology, Sichuan University, 610065 Chengdu, People's Republic of China
[2] INFN, Sezione Roma Tor Vergata, I-00133 Rome, Italy
[3] Physics Department, Technical University Munich, 85748 Garching, Germany
[4] C.N. Yang Institute for Theoretical Physics and Department of Physics and Astronomy, Stony Brook University, Stony Brook, NY 11794, United States of America
[5] Department of Physics, Novosibirsk State University, 630090 Novosibirsk, Russia
[6] Fermi National Acceleraor Laboratory, Batavia, IL 60510-5011, United States of America
[7] Oak Ridge National Laboratory, Oak Ridge, TN 37831, United States of America
[8] MAX IV Laboratory, Box 118, 22100 Lund, Sweden
[9] Department of Physics, Oklahoma State University, Stillwater, OK 74078, United States of America
[10] Department of Physics and Astronomy, The University of Tennessee, Knoxville, TN 37996, United States of America
[11] Department of Physics, Indiana University, 727 E. Third St., Bloomington, IN 47405, United States of America
[12] Indiana University Center for Exploration of Energy and Matter, Bloomington, IN 47408, United States of America
[13] Indiana University Quantum Science and Engineering Center, Bloomington, IN 47408, United States of America
[14] European Spallation Source ERIC, Lund, Sweden
[15] INFN, Laboratori Nazionali del Gran Sasso, 67010 Assergi AQ, Italy
[16] Dipartimento di Scienze Fisiche e Chimiche, Università di L'Aquila, 67100 Coppito AQ, Italy
[17] Department of Physics, Stockholm University, Stockholm, Sweden
[18] Fysiska Institutionen, Lunds Universitet, Lund, Sweden
[19] Department of Physics and Astronomy, The University of Kentucky, Lexington, KY 40506, United States of America
[20] Department of Physics and McDonnell Center for the Space Sciences, Washington University, St. Louis, MO 63130, United States of America
[21] ITEP, Bol. Cheremushkinskaya 25, Moscow 117218, Russia
[22] Departamento de Física, Universidad Técnica Federico Santa María, Casilla 110-V, Valparaiso, Chile
[23] NRC 'Kurchatov Institute'—PNPI, Gatchina, Russia
[24] Institut Laue-Langevin, 38042 Grenoble, France
[25] Institute for Nuclear Research, Russian Academy of Sciences, Prospekt 60-letiya Oktyabrya 7a, Moscow 117312, Russia
[26] Department of Physics, The University of Liverpool, Liverpool L69 7ZE, United Kingdom
[27] Department of Physics and Astronomy, University of South Carolina, Columbia, SC 29208, United States of America
[28] SISSA/INFN, Via Bonomea 265, I-34136 Trieste, Italy
[29] Department of Physics, Tennessee Tech University, 1 William L. Jones Dr., Cookeville, TN 38505, United States of America
[30] High Energy Accelerator Organization (KEK), 1-1 Oho, Tsukuba 305-0801, Japan

[31] Los Alamos National Laboratory, Los Alamos, NM 87544, United States of America
[32] Department of Physics and Astronomy, University of Uppsala, Uppsala, Sweden
[33] Department of Physics, Boston University, Boston, MA 02215, United States of America
[34] NRC 'Kurchatov Institute', Institute for Theoretical and Experimental Physics, Moscow 117218, Russia
[35] Lebedev Physical Institute, Moscow 119991, Russia
[36] Moscow Institute of Physics and Technology, Dolgoprudny 141700, Moscow Region, Russia
[37] Nagoya University, Furocho, Nagoya 464-8602, Japan
[38] DTU Physics, Technical University of Denmark, 2800 Kgs. Lyngby, Denmark
[39] School of Physics, The University of Sydney, NSW 2006, Australia
[40] Department of Physics, University of Houston, Houston, TX 77204-5008, United States of America
[41] The Henryk Niewodniczański Institute of Nuclear Physics, Polish Academy of Sciences, ul. Radzikowskiego 152, 31-342 Kraków, Poland
[42] Department of Physics and Astronomy, University of Sheffield, Sheffield S3 7RH, United Kingdom
[43] Department of Physics, Columbia University, New York, NY 10027, United States of America
[44] Department of Physics, University of Maryland, College Park, MD 20742-4111, United States of America
[45] National Institute of Standards and Technology, Gaithersburg, MD 20899, United States of America
[46] Departamento de Ciências da Natureza, Universidade Federal Fluminense, Rua Recife, 28890-000 Rio das Ostras, RJ, Brazil
[47] Institutionen för Fysik, Chalmers Tekniska Högskola, Sweden
[48] Department of Physics and Astronomy, East Tennessee State University, Johnson City, TN 37614, United States of America
[49] Department of Nuclear Engineering, The University of Tennessee, Knoxville, TN 37996, United States of America
[50] Institut de Physique des 2 Infinis de Lyon, Université de Lyon, CNRS-IN2P3-UCBL, 4 rue Enrico Fermi, Villeurbanne 69622, France
[51] Institut für Kernchemie, Johannes-Gutenberg-Universität, Mainz, Germany
[52] RIKEN iTHEMS Program, Wako, Saitama 351-0198, Japan
[53] Arithmer Inc., R & D Headquarters, Minato, Tokyo 106-6040, Japan
[54] Department of Physics, Kennesaw State University, Kennesaw, GA 30144, United States of America
[55] Physics Department, Indian Institute of Technology, Kharagpur 721302, India
[56] International Centre for Theoretical Physics, Trieste, Italy
[57] Arnold Sommerfeld Center, Ludwig-Maximilians-Universität, Theresienstraßze 37, 80333 München, Germany
[58] Joint Institute for Nuclear Research, 141980 Dubna, Moscow Region, Russia
[59] Department of Physics, University of Helsinki, PO Box 64, FIN-00014 Helsinki, Finland
[60] Department of Physics, University of Chicago, Chicago, IL 60637, United States of America
[61] FTPI and School of Physics and Astronomy, University of Minnesota, Minneapolis, United States of America
[62] KITP, UCSB, Santa Barbara, United States of America
[63] Amherst Center for Fundamental Interactions, Department of Physics, University of Massachusetts, Amherst, MA, United States of America

[64] RIKEN BNL Research Center, Brookhaven National Laboratory, Upton, New York, NY, United States of America
[65] RIKEN, 2-1 Hirosawa, Wako 351-0801, Japan
[66] Department of Physics, North Carolina State University, Raleigh, NC 27695-8202, United States of America
[67] Walter Burke Institute for Theoretical Physics, California Institute of Technology, Pasadena, CA 91125, United States of America

E-mail: david.milstead@fysik.su.se

Received 10 February 2021
Accepted for publication 1 April 2021
Published 14 June 2021

Abstract

The violation of baryon number, $\mathcal{B}$, is an essential ingredient for the preferential creation of matter over antimatter needed to account for the observed baryon asymmetry in the Universe. However, such a process has yet to be experimentally observed. The HIBEAM/NNBAR program is a proposed two-stage experiment at the European Spallation Source to search for baryon number violation. The program will include high-sensitivity searches for processes that violate baryon number by one or two units: free neutron–antineutron oscillation ($n \to \bar{n}$) via mixing, neutron–antineutron oscillation via regeneration from a sterile neutron state ($n \to [n', \bar{n}'] \to \bar{n}$), and neutron disappearance ($n \to n'$); the effective $\Delta\mathcal{B} = 0$ process of neutron regeneration ($n \to [n', \bar{n}'] \to n$) is also possible. The program can be used to discover and characterize mixing in the neutron, antineutron and sterile neutron sectors. The experiment addresses topical open questions such as the origins of baryogenesis and the nature of dark matter, and is sensitive to scales of new physics substantially in excess of those available at colliders. A goal of the program is to open a discovery window to neutron conversion probabilities (sensitivities) by up to three orders of magnitude compared with previous searches. The opportunity to make such a leap in sensitivity tests should not be squandered. The experiment pulls together a diverse international team of physicists from the particle (collider and low energy) and nuclear physics communities, while also including specialists in neutronics and magnetics.

Keywords: baryon number violation, feebly interacting particles, European Spallation Source, baryogenesis

(Some figures may appear in colour only in the online journal)

1. Introduction

The observation of baryon number violation (BNV) in a laboratory experiment would be a discovery of fundamental importance to particle physics. Within the Standard Model (SM), baryon number, $\mathcal{B}$, is a good global symmetry for tests up to the TeV scale. However, BNV is anticipated. Nonperturbative instanton effects in the $SU(2)$ sector of the SM break $\mathcal{B}$ and total lepton number, $\mathcal{L}$, while conserving $\mathcal{B} - \mathcal{L}$ [1]. Although these are negligible at temperatures that are low compared with the electroweak scale of $\mathcal{O}(100)$ GeV, they gain dynamic

importance via sphaleron processes in the early Universe at temperatures of this order [2, 3]. Furthermore, precision tests of the equivalence principle [4–6] offer no evidence for a long-range force coupled to baryon number, a key requirement for any hypothetical local gauge symmetry forbidding BNV. Most compellingly, according to Sakharov's conditions [7], BNV is required to understand the matter–antimatter asymmetry of the Universe.

Processes of the neutron transition $n \to \bar{n}$ ($\Delta\mathcal{B} = 2$) into antineutrons [8–16], and/or a transition $n \to n'$ ($\Delta\mathcal{B} = 1$) into sterile (mirror) neutrons [17–20], offer unique and comparatively unexplored discovery windows for BNV. Some early studies of $n - \bar{n}$ transitions include [9, 11–15, 21]. A recent review is [10]. Neutron conversion processes, at potentially observable rates, are anticipated in scenarios of baryogenesis and dark matter [17, 19, 21–24], supersymmetry [25, 26], extra dimensions [27–29], cosmic rays (CRs) [30, 31], neutrino mass generation mechanisms [9, 21, 23, 24, 32, 33], extensions of the SM with certain types of scalar fields [34] and even in oscillations of (anti)atomic matter [35, 36].

In this article, the high intensity baryon extraction and measurement (HIBEAM)/NNBAR program is described, a proposed two-stage program of experiments at the European Spallation Source (ESS), which will perform high-precision searches for neutron conversions in a range of BNV channels, culminating in an ultimate sensitivity increase to $n \to \bar{n}$ oscillations of three orders of magnitude over that previously attained with free neutrons after a search at the Institut Laue-Langevin (ILL) [37]. This concept was developed based on an original proposal for a single $n \to \bar{n}$ search [38]. The expanded program described here enables a staged approach where early searches with world-leading experimental sensitivities for neutron conversion phenomenon into a dark (sterile neutron) sector [17] in HIBEAM also act as developmental stepping stones providing R & D toward the final $n \to \bar{n}$ search in NNBAR. Taken together, the HIBEAM/NNBAR program will enable the discovery and characterization of a mixing sector involving neutrons, antineutrons and sterile neutrons. Furthermore, by designing and exploiting a flexible and easily interchangeable set of different experimental configurations for sterile neutron searches on a single beamline, multiple potential discoveries across a single experimental apparatus could be supported.

The first stage of the program, the HIBEAM, will employ the planned fundamental physics beamline ANNI [39] during the first phase of ESS operation, as it does not require the planned full beam power to achieve its goals. This stage focuses principally on searches for neutron conversions to sterile neutrons n': (i) neutron disappearance ($n \to [n', \bar{n}']$), (ii) neutron regeneration ($n \to [n', \bar{n}'] \to n$), and (iii) neutron–antineutron conversion via regeneration from a sterile neutron state ($n \to [n', \bar{n}'] \to \bar{n}$).[68] The HIBEAM program will include a sensitivity increase to (i) of an order of magnitude compared with previous experimental work [40–47]. An early attempt to search for (ii) has resulted in weak and unpublished limits [48] while (iii) is hitherto unexplored. Stage one acts as a pilot for the second stage of the program, a high-sensitivity search for $n \to \bar{n}$ via direct mixing. HIBEAM will provide a test platform for detector and neutron transmission technologies, and allow *in situ* development of background mitigation techniques. The second stage, NNBAR, will exploit the large beam port (LBP), a unique component of the ESS facility, to search for direct $n \to \bar{n}$ oscillations, and will operate when the ESS is at full power. Due to the substantially higher flux and neutron propagation time compared to that available at other neutron facilities worldwide, as well as advances in

[68] To distinguish the two types of searches for neutrons converting to antineutrons conducted in the program, $n \to \bar{n}$ corresponds to free neutrons converting into antineutrons which can be parameterized by a single mass mixing term in the Hamiltonian, whereas $n \to [n', \bar{n}'] \to \bar{n}$ refers to a two-stage conversion mediated via sterile neutron states, as explained in sections 3.1 and 3.4, respectively.

neutronics and detector technology since the last search with free neutrons in 1990 [37]; an increase of three orders of magnitude in sensitivity is possible.

This article is organized as follows. A brief motivation for searches for neutron conversion processes is given in section 2, followed by descriptions of the phenomenology of neutron oscillations in section 3. The results of earlier complementary searches for both free and bound neutrons and the experimental principles underpinning these searches are given in section 4. The ESS moderator system, beamlines and shielding are described in section 5. The technical design of the ANNI beamline [39] at which HIBEAM would operate is outlined in section 6. The HIBEAM program of searches and their expected sensitivities are described for processes involving sterile-neutron phenomena in section 7 and for direct $n \to \bar{n}$ oscillations in section 8. Section 9 then outlines the proposed neutronics for the final-stage NNBAR experiment and its expected sensitivity for $n \to \bar{n}$ oscillations. A dedicated section on backgrounds to these searches (section 10) is also included. Future plans and research directions are then described in section 11, followed by a summary in section 12. Simulations of the prototype test set-up to be used in the neutron test beam at the ESS are given in an appendix.

2. Motivation for searches for free neutron conversions

Neutron conversions are unique observables able to probe the new physics which could address the deficiencies of the SM. A number of theoretical arguments motivate their existence, chief among them, arguably, is baryogenesis, a critical but poorly understood area in particle physics [21–24, 49]. Other motivations include the possible existence of observable low-scale BNV that can occur in models of extra dimensions [27], branes [50] and supersymmetry [25, 26, 51], as well connections to dark matter [23, 24, 49, 52], neutrino masses and neutrino mass orderings [23, 24, 32, 33]. In this section, the theoretical motivations for the existence of neutron–antineutron and neutron–sterile neutron conversion processes are outlined in detail.

In addition to the theoretical arguments described below, it is also important to note that a strictly experimentalist consideration highlights the importance of searches for neutron conversions. In such processes, baryon number can be violated independently of other quantities hitherto observed to be conserved. Single nucleon two-body decay searches (e.g. $p \to \pi^0 e^+$ or $p \to \pi^+ \nu$) always require lepton number violation. Neutron–antineutron transitions also give rise to matter instability via dinucleon decays, and these have been sought in a number of experiments, most recently at Super-Kamiokande [53–57]. However, searches for free neutron conversions offer a theoretically clean and high-precision sensitivity to BNV-only processes.

2.1. Baryogenesis, dark matter and neutron conversions

According to Sakharov [7], there must be baryon number violating processes to explain the Universe's baryon asymmetry as observed today. Early grand unified theories (GUTs) such as $SU(5)$ [58–61] that contained BNV do not provide a good source of baryogenesis. The original baryon asymmetry generated by such models conserves $\mathcal{B} - \mathcal{L}$ and violates $\mathcal{B} + \mathcal{L}$, just as in the SM, and any leftover asymmetry below the unification scale would be erased by electroweak sphaleron interactions. A more promising class of models attempting to explain the origin of matter are those focused on electroweak baryogenesis, which do not succeed in the SM but could work in some SM extensions (see, e.g. reference [62] and references therein). Alternatively, baryogenesis can be generated via leptogenesis [63], which utilizes the seesaw mechanism [64, 65] of neutrino masses and allows for an initial lepton asymmetry to be converted into a baryon asymmetry via the sphaleron processes [66]. The simplest examples of

such models require the baryogenesis scale to be very high and are very hard to test experimentally. More specific lepto–baryogenesis models include νMSM [67, 68] and co-leptogenesis models via the neutrino interactions with sterile neutrinos from a dark sector [69–71].

A subset of weak-scale baryogenesis models have the attractive feature of being experimentally testable. Explicit UV-complete models featuring post-sphaleron baryogenesis (PSB) [22, 72, 73] use interactions that violate baryon number by two units and predict magnitudes of observable phenomena such as $n \to \bar{n}$ oscillation [21] periods. These models also connect the neutrino's Majorana mass to $n \to \bar{n}$ transformations and present an upper limit for the $n \to \bar{n}$ oscillation time which can be accessible at next-generation facilities like NNBAR at the ESS. Other simplified models that could realize PSB with a connection to neutrino masses and dark matter, while simultaneously giving rise to an observable $n \to \bar{n}$ rate, have been studied in references [23, 24]. Scenarios of co-baryogenesis with a dark sector have been discussed in references [17, 20, 74].

These searches represent dedicated probes of selection rules ($\Delta\mathcal{B} = 1, \mathbf{2}; \Delta\mathcal{L} = 0$), which fulfill a Sakharov condition but have been comparatively overlooked in the program of experiments probing fundamental symmetries and lepto/baryogenesis.

The existence of a dark sector, interacting primarily gravitationally with our familiar visible sector, has long been postulated as a means of explaining astronomical data [75]. When such a dark (sterile) sector is assumed to have particles having gauge interactions similar to our own SM interactions, one easily implies the existence of, e.g. sterile neutrinos and sterile baryons which could represent asymmetric dark matter induced by a baryon asymmetry in the dark sector. Self-interacting and dissipative characteristics of such dark matter would have interesting astrophysical implications [76–80]. In principle, observable portals onto such a sector can occur, i.e. mixing phenomena between any stable or meta-stable electrically neutral particles, allowing for conversion into a dark partner particle. For example, photons may become 'dark photons' via kinetic mixing [81], while neutrinos can oscillate into sterile neutrinos of the dark sector [82, 83]. The neutron represents another possible generic portal.

One of the simplest examples of a hidden sector is the theory of mirror matter, a dark sector represented by a replica of the SM (for reviews see [79, 84, 85], for a historical overview see [86]). The assumption of this minimal model forms the basis of the phenomenological framework for the sterile neutron transition searches considered in this work, though these searches have some sensitivity to a more generic dark sector. Forms of $n \to n'$ transitions have been proposed [87, 88], to which HIBEAM is sensitive, that can also shed light onto the apparent anomaly present between experimental free cold and ultracold neutron 'beam' and 'bottle' measurements of the neutron lifetime [89].

2.2. Exploring the TeV–PeV regime with $n \to \bar{n}$ searches

BNV is a generic feature of GUTs [90] and many other proposed extensions of the SM [23–27, 49, 51].

Classic BNV signatures include proton and bound neutron decay, mediated by four-fermion operators, and $n \to \bar{n}$ oscillations [8], mediated by six-quark operators [21, 91]. In SM effective field theory, the lowest orders of these operators have mass dimensions $+6$ and $+9$, respectively; also, in supersymmetric models these can take dimensions $+4$ and $+5$. Thus, if there were only one mass scale $M_{\rm BNV}$ characterizing BNV processes, $n \to \bar{n}$ oscillations would be more highly suppressed (like $1/M_{\rm BNV}^5$) compared with proton and bound neutron decay, for which the effective Lagrangian would only involve a suppression by $1/M_{\rm BNV}^2$. However, there is no good reason to assume that BNV processes correspond to a single scale nor is it known which processes nature has chosen should there be one BNV scale. There are a number of

approaches where $n \to \bar{n}$ oscillations are the dominant manifestation of BNV, while proton decay is either absent or suppressed well below experimental limits [9, 21, 27, 92, 93]. Some early studies of $n \to \bar{n}$ oscillations include [9, 11–15, 21]; a recent review is [10].

Basic dimensional analysis based on the above considerations implies sensitivity to mass scales of $\mathcal{O}(10) - \mathcal{O}(1000)$ TeV, accessible via a precision $n \to \bar{n}$ oscillation search such as the experimental program proposed in this article. Such a scale is substantially in excess of the reach of current or planned colliders. This is complementary to the large-volume single nucleon decay experiments that are sensitive to a different set of BNV processes with scales near the GUT energy.

Examples of models predicting observable $n \to \bar{n}$ arising from BNV at TeV and PeV scales include R-parity violating supersymmetry scenarios [25, 26] and extra-dimensional models. Extra-dimensional scenarios arise from the leading candidate for quantum gravity, i.e. superstring theory [94], which predicts extra spatial dimensions beyond the three which are observed. Compactification radii characterizing these extra dimensions might be much larger than the Planck length. A model of this type [27, 28] provides an explicit example of how proton decay can be strongly suppressed, while $n \to \bar{n}$ transformations can occur at levels within reach of the new, high-sensitivity experiment proposed here. This is also true of an extra-dimensional model with a left–right gauge symmetry broken at the scale of $\mathcal{O}(10^3)$ TeV [29].

2.3. The connection of $n \to \bar{n}$ with neutrino masses and proton decay

Another topical issue in which the $n \to \bar{n}$ process may play a role concerns the origin of neutrino mass. There is a symbiosis between $n \to \bar{n}$ transitions and neutrinoless double β decays: they both violate $\mathcal{B} - \mathcal{L}$ (the anomaly-free SM symmetry) by two units and imply Majorana masses, and both processes are connected in unification models, such as the left–right-symmetric model [95–97] based on the gauge group $G_{\rm LRS} = SU(3)_{\rm c} \times SU(2)_{\rm L} \times SU(2)_{\rm R} \times U(1)_{B-L}$. In these models, the spontaneous symmetry breaking of $G_{\rm LRS}$ to the SM is produced by the vacuum expectation value (VEV) of a Higgs field transforming as $(1, 1, 3)_2$ under $G_{\rm LRS}$, so that its VEV breaks $\mathcal{B} - \mathcal{L}$ by two units. This gives rise to both an operator with $\Delta\mathcal{L} = 0$ and $\Delta\mathcal{B} = 2$, such as the six-quark operator mediating $n \to \bar{n}$ oscillations and to an operator such as the bilinear Majorana product of right-handed neutrinos, with $\Delta\mathcal{B} = 0$ and $\Delta\mathcal{L} = 2$ that is responsible for a seesaw mechanism leading to Majorana neutrino masses. Thus in theories with Majorana neutrino masses and quark–lepton unification, it is natural to expect both Majorana neutrinos as well as $n \to \bar{n}$ transitions [21]. In fact, there exist both left–right-symmetric and $SO(10)$ models with observable $n \to \bar{n}$ oscillation where this connection is explicit; there has also been recent work on these connections within $SU(5)$ effective field theory [98].

Setting aside specific theories of physics beyond the SM, the sphaleron interaction itself being a nine-quark–three-lepton interaction can be written as $QQQQQQ\,QQQL\,LL$. This implies that if any two of the following processes are seen, then the other should exist: $n \to \bar{n}$ transition (the first six-quark operator), proton decay (the second four-fermion operator) and $\Delta\mathcal{L} = 2$, lepton number violation. The last term implies low energy processes such as neutrinoless double-beta decay and direct lepton number violation in the form of same sign charged lepton pairs [99] at hadron colliders, possibly even at the Large Hadron Collider (LHC). The neutrinoless double-beta decay can result from the neutrino Majorana mass or the new physics [97] that leads to same sign dileptons at colliders, and in the left–right symmetric model of neutrino mass there is a deep connection between the two processes [100].

In summary, together with the discovery of proton decay, an observation of $n \to \bar{n}$ oscillations, could, therefore, establish evidence for the Majorana nature of neutrinos and/or probe the theory behind neutrino Majorana mass. Equivalently, discoveries of $n \to \bar{n}$ oscillations and

$\Delta\mathcal{L} = 2$ lepton number violation would imply proton decay. Searches for $n \to \bar{n}$ oscillations thus play a key and complementary role in a wider experimental program of $\mathcal{B}$ and $\mathcal{L}$ violation searches [101].

3. Phenomenology of the neutron conversion processes

That nature must violate the baryon number is a statement that can be made with confidence. However, should nature have chosen BNV-only processes, then not only does this imply that the channels which are available for high-precision study are limited, but also that a BNV signal is *fragile*. Each channel can require special experimental conditions in order for BNV to manifest itself. In this section, the formalism of neutron conversions and the conditions for a signal to appear are outlined. A description is also given of other relevant phenomenological aspects of the HIBEAM and NNBAR search programs, such as the modeling of the scattering of a neutron off a guide and antineutron–nucleon annihilation on a nucleus.

3.1. Neutron–antineutron conversions

In the SM frames, the neutron has only the Dirac mass term $m\bar{n}n$ which conserves $\mathcal{B}$. However, as mentioned in section 2.2, $n \to \bar{n}$ can proceed by effective six-quark (dimension 9) operators. These involve light quarks u and d and violate $\mathcal{B}$ by two units:

$$\mathcal{O}_{\Delta\mathcal{B}=2} = \frac{1}{\mathcal{M}^5}(udd)^2 \; + \; \text{h.c.}, \tag{1}$$

with $\mathcal{M}$ being a large cutoff scale originated from new physics beyond the SM. This can induce a Majorana mass term:

$$\frac{\epsilon_{n\bar{n}}}{2}(n^{\mathrm{T}}Cn + \bar{n}C\bar{n}^{\mathrm{T}}) = \frac{\epsilon_{n\bar{n}}}{2}(\bar{n_{\mathrm{c}}}n + \bar{n}n_{\mathrm{c}}), \tag{2}$$

where C is the charge conjugation matrix and $n_{\mathrm{c}} = C\bar{n}^{\mathrm{T}}$ stands for the antineutron field.[69] Thus, the $n \to \bar{n}$ matrix element/mixing mass term $\epsilon_{n\bar{n}}$ depends on the scale of new physics:

$$\epsilon_{n\bar{n}} = \frac{C\Lambda_{\mathrm{QCD}}^6}{\mathcal{M}^5} = C\left(\frac{500\ \mathrm{TeV}}{\mathcal{M}}\right)^5 \times 7.7 \cdot 10^{-24}\ \mathrm{eV}, \tag{3}$$

with $C = O(1)$ being the model-dependent factor in the determination of the matrix element $\langle\bar{n}|\mathcal{O}_{\Delta\mathcal{B}=2}|n\rangle$. This mixing between the neutron and antineutron fields gives rise to the phenomenon of $n \to \bar{n}$ oscillation [8, 9]. The direct bound on $n \to \bar{n}$ oscillation time $\epsilon_{n\bar{n}}^{-1} = \tau_{n\bar{n}} > 0.86 \times 10^8$ s [37], i.e. $\epsilon_{n\bar{n}} < 7.7 \times 10^{-24}$ eV, corresponds to $\mathcal{M} > 500$ TeV or so. By improving the experimental sensitivity by two orders of magnitude, one could test the new physics above the PeV scale.

Conversion of $n \to \bar{n}$ can be understood as the evolution of a beam of initially pure neutrons

$$|\Psi(t)\rangle = \psi_n(t)\,\psi_{\bar{n}}(t) = \mathrm{e}^{-\mathrm{i}\hat{\mathcal{H}}t}|\Psi(t=0)\rangle, \qquad |\Psi(t=0)\rangle = |n\rangle = 1\,0, \tag{4}$$

[69] Generically these operators induce four bilinear terms $\bar{n}n_{\mathrm{c}}$, $\bar{n}\gamma^5 n_{\mathrm{c}}$, $\bar{n_{\mathrm{c}}}n$ and $\bar{n_{\mathrm{c}}}\gamma^5 n$, with complex coefficients. However, by proper redefinition of fields, these terms can be reduced to just one combination (2) with a real $\epsilon_{n\bar{n}}$ which is explicitly invariant under transformations of the charge conjugation ($n \to n_{\mathrm{c}}$) and parity ($n \to i\gamma^0 n$, $n_{\mathrm{c}} \to i\gamma^0 n_{\mathrm{c}}$) [102, 103].

described by the 2×2 Hamiltonian

$$\hat{\mathcal{H}} = \begin{pmatrix} E_n & \epsilon_{n\bar{n}} \\ \epsilon_{n\bar{n}} & E_{\bar{n}} \end{pmatrix} \tag{5}$$

where E_n and $E_{\bar{n}}$ are the neutron and antineutron energies, respectively. While the neutron and antineutron masses are equal by CPT invariance, E_n and $E_{\bar{n}}$ are not generically equal due to the environmental effects which act differently on the neutron and antineutron states, as a presence of matter medium or magnetic fields, or perhaps some hypothetical fifth forces [104, 105].

The probability of finding an antineutron at a time t is given by $P_{n\bar{n}}(t) = |\psi_{\bar{n}}(t)|^2$ or explicitly:

$$P_{n\bar{n}}(t) = \frac{\epsilon_{n\bar{n}}^2}{(\Delta E/2)^2 + \epsilon_{n\bar{n}}^2} \sin^2 \left[t \sqrt{(\Delta E/2)^2 + \epsilon_{n\bar{n}}^2} \right] \, \mathrm{e}^{-t/\tau_n}, \tag{6}$$

where $\Delta E = E_n - E_{\bar{n}}$ and τ_n denotes the mean life of the free neutron. It thus becomes immediately clear that the probability of a conversion is suppressed when the energy degeneracy between neutron and antineutron is broken. In particular, for free neutrons, suppression occurs due to the interaction of the magnetic field ($B \simeq 0.5$ G on Earth) with the neutron and antineutron's magnetic dipole moments ($\vec{\mu}_n = -\vec{\mu}_{\bar{n}}$), equivalent to $\Delta E/2 = |\vec{\mu}_n \vec{B}| \approx (B/1 \text{ G}) \times 10^{-11}$ eV in equation (6). To prevent significant suppression of $n \to \bar{n}$ conversion, one must maintain the so called quasi-free regime $|\Delta E| t \ll 1$, which can be realized in vacuum in nearly zero magnetic field [106–108]. In this case, equation (6) reduces to:

$$P_{n\bar{n}}(t) = \epsilon_{n\bar{n}}^2 t^2 = \frac{t^2}{\tau_{n\bar{n}}^2} = \left(\frac{t}{0.1 \text{ s}} \right)^2 \left(\frac{10^8 \text{ s}}{\tau_{n\bar{n}}} \right)^2 \times 10^{-18}, \tag{7}$$

where $\tau_{n\bar{n}} = 1/\epsilon_{n\bar{n}}$ is the characteristic oscillation time. Since in real experimental situations the neutron flight time is small, $t \sim 0.1$ s or so, the exponential factor related to the neutron decay can be neglected in equation (6).

This necessitates magnetic shielding for searches utilizing a neutron beam [37, 109–111]. HIBEAM and NNBAR must employ such shielding, as will be discussed in section 8.1.

In the experiment performed at the ILL [37], the magnetic field was suppressed below 10 mG or so and the lower limit $\tau_{n\bar{n}} > 0.86 \times 10^8$ s (90% CL) was obtained. In turn, this translates into upper limit $\epsilon_{n\bar{n}} < 7.7 \times 10^{-24}$ eV, which still stands as the strongest limit on the $n \to \bar{n}$ mass mixing obtained with free neutrons. The effects of imperfect vacuum (residual gas pressure) on the observation of neutron to antineutron transformation were discussed in references [37, 112–114].

As for bound neutrons in a nucleus, the potential energy difference experienced between a neutron and antineutron in the strong nuclear field ($\Delta E \sim 10$–100 MeV, depending on nuclei) introduces a suppression of $\sim 10^{-31}$ with respect to the conversion of a free neutron. This of course inhibits the conversion of neutrons bound in nuclei, with sensitive searches only possible with large-volume detectors [53, 115–121], such as Super-Kamiokande [53, 57], SNO [122], DUNE [123–125] or Hyper-Kamiokande [126]. The comparatively large number of neutrons permits searches with currently complementary limits. However, event identification is obscured by atmospheric backgrounds, intranuclear scattering of the decay products and other nuclear physics effects.

A limit on $n \to \bar{n}$ conversion time in a specific nucleus (T) can be related to that of a free neutron ($\tau_{n\bar{n}}$) via a nuclear suppression factor, $R \sim 10^{22}$ s^{-1}, which can be calculated with

phenomenological nuclear models [124, 127–133] and predict quadratic scaling such that:

$$T = R \cdot \tau_{n\bar{n}}^2 \sim \left(\frac{10^8 \text{ s}}{\tau_{n\bar{n}}}\right)^2 \times 10^{31} \text{ yr}. \tag{8}$$

At present, the strongest limit obtained by Super-Kamiokande [57] for oxygen is $\tau_{n\bar{n}} > 4.7 \times 10^8$ s, or equivalently $\epsilon_{n\bar{n}} < 2.5 \times 10^{-24}$ eV. Super-Kamiokande has also carried out searches for $\Delta B = -2$ dinucleon decays to specific multi-meson and leptonic final states [54–56, 134]. More details on current limits and future sensitivities are in section 4.1.

Caution is required when comparing limits and sensitivities for free and bound neutron searches. Calculations relating T and $\tau_{n\bar{n}}$ rely on underlying model assumptions, such as a point-like conversion process, while the physics behind $n \to \bar{n}$ conversion is *a priori* unknown[70]. The visibility of a signal in a bound neutron search could therefore be arbitrarily suppressed compared to a free search, or vice versa. For example, a recently proposed model of low-scale BNV contains the possibility of a suppressed (or even enhanced) bound neutron conversion probability [33]. There can be also some environmental effects that can affect free $n \to \bar{n}$ oscillations even if the magnetic field is properly shielded. These effects can be related, e.g. with long-range fifth-forces induced by very light $\mathcal{B} - \mathcal{L}$ baryophotons. Present high-sensitivity limits on such forces [137] with Yukawa radius comparable to the Earth′s radius or to Sun–Earth distance still allow significant contribution to the neutron–antineutron energy level splitting, which in fact can be as large as $\Delta E \sim 10^{-11}$ eV or so [104, 105].

Consideration of free and bound neutron searches is thus complementary: neither makes the other redundant, and indeed they require one another to help constrain the underlying physical process.

Within the framework of an assumed ultraviolet extension of the SM that features $n - \bar{n}$ transitions, one has a prediction for the coefficients of the various types of six-quark operators in the resultant low-energy effective Lagrangian, and the next step in obtaining a prediction for the $n - \bar{n}$ transition rate of free neutrons is to estimate the matrix elements of these six-quark operators between $|n\rangle$ and $|\bar{n}\rangle$ states. Since the six-quark operators have dimension 6, their matrix elements are of the form Λ_{eff}^6. The relevant scale is set by the quantum chromodynamics (QCD) confinement scale, $\Lambda_{\text{QCD}} \sim 0.25$ GeV, so one expects, roughly speaking, that the matrix elements are of order $\sim \Lambda_{\text{QCD}}^6 \simeq 2.4 \times 10^{-4}$ GeV^6, and this expectation is borne out by both early estimates using the MIT bag model [14, 15] and recent calculations using lattice QCD (LQCD) [138–142], including approximate assessments of modeling uncertainties. The LQCD results in [139, 140] indicate that, for most operators, the corresponding Λ_{eff} is larger, by $\sim 10\%$–40%, than the Λ_{eff} characterizing the MIT bag model results, i.e. a factor ~ 2–8 for Λ_{eff}^6, and thus for the matrix elements themselves. This suggests that overall experimental sensitivities may reach higher than previously expected [138]. This being said, direct constraint of PSB and its predicted upper bound on $\tau_{n\to\bar{n}}$ [73] is slightly different, as this limit is derived not from tree-level amplitudes but instead from loop diagrams involving W-boson exchange. In [73], larger MIT bag-model estimates are used, and so the LQCD matrix element for this particular amplitude appears smaller by some $\sim 15\%$ [140]; this leads to an expectation that the upper limit for $\tau_{n\to\bar{n}}$ will be shifted slightly up by roughly the same proportion. The

[70] This being said, there has been great progress in a broad program of intranuclear suppression factor calculations across many nuclei which show rather remarkable similarity despite their quite disparate theoretical origins [124, 127, 135, 136]. One should also note that intranuclear experiments like SNO [122] have chosen specific targets (deuterium) and techniques to minimize contamination from these and other model dependent nuclear effects, including avoiding excessive final state interactions.

community's integration of this new knowledge is continuing, and still more accurate predictions are being actively discussed and developed [143]. Similar computational methods may eventually advance peripheral modeling of secondary processes, such as the annihilation itself and background interactions.

3.2. Phase shift suppression

A key attribute of a traditional free $n \to \bar{n}$ conversion search is a neutron beam focused onto an annihilation target to minimize interactions with, e.g. a guide wall. The difference in neutron and antineutron interactions with wall material have been assumed to act as a large potential difference, suppressing the oscillation. The interaction can be seen as destroying any wave function component, which effectively 'resets the clock' for the oscillation time measurement. With this assumption, only the neutron's free-flight time since last wall interaction contributes to the probability to find an antineutron, necessitating a large-area experimental apparatus in practice.

An *almost* free $n \to \bar{n}$ oscillation search has recently been proposed [144, 145] in which one allows slow, cold neutrons (and antineutrons) (with energies of $< 10^{-2}$ eV) to reflect from effective $n/\bar{n}$ optical mirrors. Although the reflection of $n/\bar{n}$ had been considered in the 1980s for ultra cold neutrons (UCNs) [146–149] and recently in [145] for proposed experiments to constrain $\tau_{n\to\bar{n}}$, the authors now extended this approach to higher energies, namely where nominally cold, initially collimated neutrons can be reflected from neutron guides when their transverse velocities with respect to the wall are similarly very or ultracold. Conditions for suppressing the phase difference for n and $\bar{n}$ were studied, and the required low transverse momenta of the $n/\bar{n}$ system was quantified, leading to new suggestions for the nuclei composing the reflective guide material. It was shown that, over a broad fraction of phase space, the relative phase shift of the n and $\bar{n}$ wave function components upon reflection can be small, while the probability of coherent reflection of the $n/\bar{n}$ system from the guide walls can remain high. The theoretical uncertainties associated with a calculation of the experimental sensitivity, even in the absence of direct measurements of low energy $\bar{n}$ scattering amplitudes, can be small. A new calculation of the low energy antineutron–nucleus scattering amplitudes needed to evaluate these uncertainties has recently appeared [150].

An important consequence would be that the conversion probability depends on the neutron's total flight time, as wall interactions no longer reset the clock. Such an experimental mode relaxes some of the constraints on free n oscillation searches, and in principle allows a much higher sensitivity to be achieved at reduced complexity and costs. The above represents a new idea from within the community which requires a program of simulation and experimental verification. While this does not form part of the current core plan for the HIBEAM/NNBAR experiment, it is considered as a promising future research direction, and experimental verification of this concept is under investigation.

3.3. Neutron–mirror neutron conversions

Though the HIBEAM searches are generic in nature, the mixing of n and its sterile twin n' is considered here within the paradigm of a parallel gauge sector in a mirror matter model [17, 30]. There are a range of possible conversion processes which can be explored experimentally, motivating a suite of searches outlined in section 7.

In addition to external fields and interactions in the standard sector, the possibility of equivalent fields in the sterile sector must be taken into consideration. There can exist also some hypothetical forces between ordinary and sterile sector particles which can be induced e.g.

by the photon kinetic mixing with dark photon [81, 151–153], or by new gauge bosons interacting with particles of both sectors as e.g. common $\mathcal{B}-\mathcal{L}$ gauge bosons [104] or common flavor gauge bosons of family symmetry [154–156]. The respective forces can provide portals for direct detection of dark matter components from a parallel sterile sector and give a possibility for identification of their nature [157–159]. In addition, flavor gauge bosons can induce mixing between neutral ordinary particles and their sterile partners and induce oscillations, e.g. between kaons and sterile kaons, conversion of muonium into hidden muonium, etc [155, 156].

The possibility of neutron–mirror neutron mass mixing $\alpha_{nn'}\bar{n}n' + \text{h.c.}$ was proposed in [17]. It can be induced by six-fermion effective operators $\frac{1}{M^5}(\overline{u}\overline{d}\overline{d})(u'd'd')$ similar to operator (1) but involving three ordinary quarks and three quarks of the sterile (mirror) sector. This mixing violates conservations of both baryon number and mirror baryon number ($\Delta\mathcal{B}=1, \Delta\mathcal{B}'=-1$) but it conserves the combination $\mathcal{B}+\mathcal{B}'$. The mixing mass $\alpha_{nn'}$ can be estimated as:

$$\alpha_{nn'} = \frac{C\Lambda_{\text{QCD}}^6}{M^5} = C^2\left(\frac{10\ \text{TeV}}{M}\right)^5 \times 2.5\times 10^{-15}\ \text{eV}. \tag{9}$$

It was shown that no direct, astrophysical or cosmological effects forbid that $n\to n'$ oscillation time $\tau_{nn'} = 1/\alpha_{nn'}$ can be smaller than the neutron decay time, and in fact it can be as small as a second. So rapid $n\to n'$ oscillations could have interesting implications for the propagation of ultra-high CRs [30, 31] or for neutrons from solar flares [160]. Thus, the effective scale M of underlying new physics can be of a few TeV, with direct implications for the search at the LHC and future accelerators. Effects of $n\to n'$ oscillation can be directly observed in experiments searching for anomalous neutron disappearance ($n\to n'$) and/or regeneration ($n\to n'\to n$) processes [17]. Experimental sensitivities of such searches with ultracold and cold neutrons were discussed in references [161, 162].

The Hamiltonian for $n\to n'$ is given in equation (10). The presence of a static magnetic moment shifts the n and n's total energies. The Hamiltonian is expressed for the general case of neutrons propagating in magnetic fields B (of the standard sector) and B' (of the sterile sector); the former of these is generated by the magnetic poles of the Earth, the latter by hypothetical ionization and flow of gravitationally captured dark material in and around the Earth [18]. Such an accumulation could occur due to ionized gas clouds of sterile atoms captured by the Earth, e.g. due to photon–sterile photon kinetic mixing; present experimental and cosmological limits on such mixing [163, 164] and geophysical limits [165] still allow the presence of a relevant amount of sterile material on the Earth [166]. Then a sterile magnetic field can be induced by the drag of dark electrons due to the Earth's rotation via the mechanism described in [167], which can be enhanced through the dynamo effect [18]. In addition to the static magnetic moments, $\vec{\mu}_n$ and $\vec{\mu}_{n'}$, and unlike for the $n\to\bar{n}$ transition[71], transition magnetic moments (TMMs) [74] may also be present in the off-diagonal TMMs $\vec{\mu}_{nn'} = \kappa\vec{\mu}_n$ between the neutron and sterile neutron term[72].

As analogous contributions to the Hamiltonian, TMMs can be seen as quantities which are as fundamental as the more familiar static magnetic moments. TMMs contribute to the mixing via the interaction of new physics processes with the external magnetic fields, leading to terms $\kappa\vec{\mu}_n\vec{B}$ and $\kappa'\vec{\mu}_n\vec{B}'$, where the dimensionless parameter $\kappa \ll 1$ measures the magnitudes of the

[71] A non-zero TMM between the neutron and antineutron is forbidden by Lorentz invariance then [102, 103]. Moreover, any transition $n\to\bar{n}\gamma^*$ with an external virtual photon connected to a proton would destabilize nuclei even in the absence of $n\to\bar{n}$ mixing.

[72] TMMs play a role both in understanding SM processes, e.g. hadronic decays [168], and the development of BSM physics models, such as those predicting neutrino flavor-changing processes [169].

TMM in units of neutron magnetic moment μ_n.

$$\hat{\mathcal{H}} = \begin{pmatrix} m_n + \vec{\mu}_n\vec{B} & \alpha_{nn'} + \kappa\vec{\mu}_n\vec{B} + \kappa'\vec{\mu}_n\vec{B}' \\ \alpha_{nn'} + \kappa\vec{\mu}_n\vec{B} + \kappa'\vec{\mu}_n\vec{B}' & m_{n'} + \vec{\mu}_{n'}\vec{B}' \end{pmatrix}. \tag{10}$$

Beyond removing exponential decay, a number of simplifications can be made to the picture of $n \to n'$ mixing described above. In the simplest model, it is assumed that n and n' share degeneracies such as $m_n = m_{n'}$, $|\vec{\mu_n}| = |\vec{\mu_n'}|$ and $\kappa = \kappa'$. The magnitude, direction and time dependence of the mirror magnetic field $\vec{B}'$ is *a priori* unknown.

If only $n \to n'$ mass mixing $\alpha_{nn'}$ is present, i.e. assuming for the moment that $\kappa = 0$, then the probability of $n \to n'$ oscillation at time t is given by [18, 45]:

$$P_{nn'}(t) = \frac{\alpha_{nn'}^2 \cos^2\frac{\beta}{2}}{(\omega-\omega')^2}\sin^2\left[(\omega-\omega')t\right] + \frac{\alpha_{nn'}^2 \sin^2\frac{\beta}{2}}{(\omega+\omega')^2}\sin^2\left[(\omega+\omega')t\right], \tag{11}$$

where $2\omega = |\mu_n B|$ and $2\omega' = |\mu_n B'|$, β is the angle between the directions of magnetic fields $\vec{B}$ and $\vec{B}'$, and the contribution of $\alpha_{nn'}$ in the oscillation frequencies is neglected assuming that $\alpha_{nn'} < |\omega - \omega'|$. If $|\omega - \omega'|t \gg 1$, the oscillations can be averaged in time and one obtains:

$$\overline{P}_{nn'} = \frac{\alpha_{nn'}^2 \cos^2\frac{\beta}{2}}{2(\omega-\omega')^2} + \frac{\alpha_{nn'}^2 \sin^2\frac{\beta}{2}}{2(\omega+\omega')^2}. \tag{12}$$

In particular, if $B' = 0$ (i.e. $\omega' = 0$), from (11) the expression $P_{nn'}(t) < (\alpha_{nn'}/\omega)^2$ is obtained if $\omega t > 1$, and $P_{nn'}(t) \approx (\alpha_{nn'}t)^2$ if $\omega t \ll 1$.

As B approaches B', $|\omega - \omega'|$ decreases and the probability $P_{nn'}(t)$ resonantly increases. In a quasi-free regime, when $|\omega - \omega'|t \gg 1$, the probability reaches the value:

$$P_{nn'}(t) \approx \frac{1}{2}(\alpha_{nn'}t)^2\cos^2\frac{\beta}{2} = \cos^2\frac{\beta}{2}\left(\frac{t}{0.1\text{ s}}\right)^2\left(\frac{1\text{ s}}{\tau_{nn'}}\right)^2 \times 5 \times 10^{-3}, \tag{13}$$

where $\tau = 1/\alpha_{nn'}$ is the characteristic $n \to n'$ oscillation time for free neutrons in a field-free vacuum. Therefore, this leads to a situation where the $n \to n'$ oscillation probability non-trivially depends on the value (and direction) of the magnetic field. This effect can be observed in experiments searching for anomalous neutron disappearance ($n \to n'$) and regeneration ($n \to n' \to n$) [17]. Experimental sensitivities of such searches with cold and ultracold neutrons were discussed in reference [161].

Several dedicated experiments searching for $n \to n'$ oscillation with UCNs were performed in the last decade [40–46]. Under the hypothesis that there is no mirror magnetic field on the Earth, i.e. $B' = 0$, the strongest lower limit $\tau_{nn'} > 414$ s (90% CL) was obtained by comparing the UCN losses in zero ($B < 10^{-3}$ G) and non-zero ($B = 0.02$ G) magnetic fields [41]. However, this limit becomes invalid in the presence of B'. Lower limits on $\tau_{nn'}$ and $\tau_{nn'}/\sqrt{\cos\beta}$ in the presence of non-vanishing B' following from experiments [40–46] are summarized in reference [46]. In fact, some experiments show deviations from the null hypothesis, which may point toward $\tau_{nn'} \sim 10$ s and $B' \sim 0.1$ G. For $B' > 0.5$ G or so, an oscillation time as small as 1 s is not excluded [46].

In the case of TMM-induced $n \to n'$ transition, the average oscillation probability becomes [88]:

$$\overline{P}_{nn'} = \frac{2\kappa^2(\omega+\omega')^2\cos^2\frac{\beta}{2}}{(\omega-\omega')^2} + \frac{2\kappa^2(\omega-\omega')^2\cos^2\frac{\beta}{2}}{(\omega+\omega')^2}. \tag{14}$$

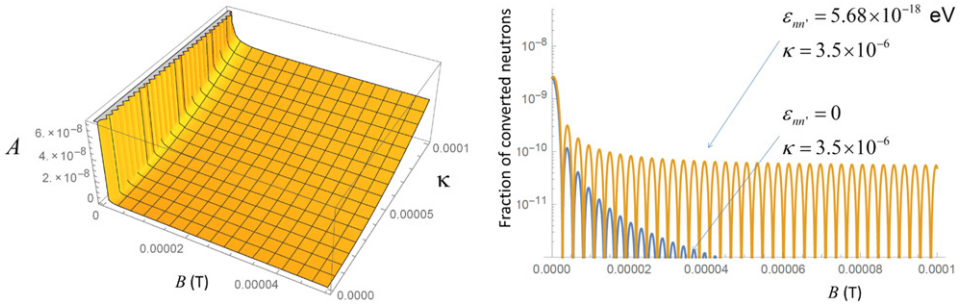

Figure 1. Left: amplitude of the probability function for $n \to n'$ as a function of $|\vec{B}|$ and κ for a value of $\tau = 500$ s. Right: fraction of neutrons which have been converted as a function of $|\vec{B}|$ traveling 25 m in a vacuum at a velocity of 1000 m s^{-1}. Predictions are shown for conversions induced by mass mixing and a TMM ($\tau = 500$ s and $\kappa = 3.5 \times 10^{-6}$) and for mass mixing alone ($\tau = 500$ s) alone.

The limits on parameter κ and the TMM $\kappa\mu_n$ that can be obtained by data analysis of these experiments [40–46] are given in reference [88]. In the case when $\alpha_{nn'}$ and κ are both present, the average probability of $n \to n'$ transition is given just by a sum of terms (12) and (14).

In the following, we choose $\vec{B}'$ to be zero, leaving only three parameters determining the probability of the $n \to n'$ process: $\alpha_{nn'}$, κ and $\vec{B}$. Figure 1 illustrates the interplay between these parameters and their impact on the oscillation, taking $\alpha_{nn'} = 5.68 \times 10^{-18}$ eV ($\tau = 500$ s). For TMM-only transitions (when $\alpha_{nn'} = 0$), one has:

$$P_{nn'} = 2\kappa^2. \tag{15}$$

Figure 1 (right) compares the fraction of converted neutrons after having traveled 25 m in a vacuum for the case of a TMM term and non-zero mass mixing versus zero mass mixing.

The TMM can also lead to an enhanced $n \to n'$ transformation in a gas atmosphere due to the creation of a positive Fermi potential along the neutron path [88]. A constant magnetic field $\vec{B}$ in the flight volume can be chosen such that for one polarization of neutron it will provide a negative magnetic potential compensating the positive Fermi potential of the gas: $V_{\rm F} = \vec{\mu}\vec{B}$. Thus, for example, the Fermi potential of air at normal temperature and pressure corresponds to a constant magnetic field of $\sim$10 G. Continuing to assume that $|B'| = 0$, the oscillation Hamiltonian becomes:

$$\mathcal{H} = \begin{pmatrix} V_{\rm F} - \mu B & \alpha_{nn'} + \kappa\mu B \\ \alpha_{nn'} + \kappa\mu B & 0 \end{pmatrix}. \tag{16}$$

With a zero diagonal term (in the resonance), this corresponds to a pure oscillation with probability:

$$P_{nn'} = (\alpha_{nn'} + \kappa\mu B)^2 t^2. \tag{17}$$

The probability due to the mass mixing term here is enhanced by the term due to the TMM that is proportional to field B.

3.4. Conversions of neutrons to antineutrons via sterile neutrons

Sections 3.1 and 3.3 address the transformations of $n \to \bar{n}$ and $n \to n'$, respectively. However, should a sterile neutron sector exist, processes connecting the visible and sterile sectors need

not be restricted to the above processes, as proposed in references [74, 170]. It is essential to test the full range of conversions between the sectors: $n \to \{n', \bar{n}'\}, \bar{n} \to \{n', \bar{n}'\}$, $n' \to \{n, \bar{n}\}$ and $\bar{n}' \to \{n, \bar{n}\}$.

In principle, a transformation to four states mixed in the n, $(n, \bar{n}, n', \bar{n}')$, in free space without any fields can be described by the symmetric Hamiltonian:

$$\hat{\mathcal{H}} = \begin{pmatrix} m_n + \vec{\mu}_n \vec{B} & \varepsilon_{n\bar{n}} & \alpha_{nn'} & \alpha_{n\bar{n}'} \\ \varepsilon_{n\bar{n}} & m_n - \vec{\mu}_n \vec{B} & \alpha_{n\bar{n}'} & \alpha_{nn'} \\ \alpha_{nn'} & \alpha_{n\bar{n}'} & m_{n'} + \vec{\mu}_{n'} \vec{B}' & \varepsilon_{n\bar{n}} \\ \alpha_{n\bar{n}'} & \alpha_{nn'} & \varepsilon_{n\bar{n}} & m_{n'} - \vec{\mu}_{n'} \vec{B}' \end{pmatrix}. \tag{18}$$

Here, $\varepsilon_{n\bar{n}}$ is the $n\bar{n}$ Majorana mass mixing parameterand $\alpha_{nn'}$ and $\alpha_{n\bar{n}'}$ are mass mixing parameters for nn' and for $n\bar{n}'$ correspondingly. In the following we neglect possible TMM terms between $n, \bar{n}$ and $n', \bar{n}'$ states and assume $m_{n'} = m_n$, $\mu_{n'} = \mu_n$.

Thus, in this case, the final state antineutron can be a result of the classical $n \to \bar{n}$ with mixing mass amplitude ε, and with baryon number change $\Delta\mathcal{B} = -2$ and probability $P_{n\to\bar{n}} = \varepsilon_{n\bar{n}}^2 t^2$. It can also arise due to the second-order oscillation process: $n \to n' \to \bar{n}$ with amplitude $(\alpha_{nn'}\alpha_{n\bar{n}'})$ or $n \to \bar{n}' \to \bar{n}$ with amplitude $(\alpha_{n\bar{n}'}\alpha_{nn'})$ plus interference of all three channels. If $\varepsilon_{n\bar{n}}$ is very small and $\alpha_{nn'}$ and $\alpha_{n\bar{n}'}$ are relatively large, then $n \to \bar{n}$ could be observed for a non-zero sterile magnetic field. However, neither previous limits on free $n \to \bar{n}$ oscillation from experiments in which the magnetic field was suppressed [37], nor nuclear stability limits from $n \to \bar{n}$ conversion in nuclei [53], would be valid for this scenario, since a fixed field $\vec{B}$ compensating for the magnetic field in the sterile sector would be needed to allow the full process $n \to n' \to \bar{n}$ to proceed. In fact, $n \to \bar{n}$ conversion in free neutron experiments can emerge as second-order process induced by $n \to n'$ and $n \to n'$ conversions, with the probability $P_{n\bar{n}}(t) \simeq P_{nn'}(t)P_{n\bar{n}'}(t)$. Existing limits allow the oscillation times $\tau_{nn'}$ and $\tau_{n\bar{n}'}$ to be as small as $1 \div 10$ s (for a summary of present experimental situation see [46]). Therefore, by properly tuning the value of magnetic field B resonantly close to B' (with precision of mG or so) and thus achieving the quasi-free regime, the probability of induced $n \to \bar{n}$ oscillation can be rendered as large as:

$$P_{n\bar{n}}(t) = \frac{1}{4}\alpha_{nn'}^2\alpha_{n\bar{n}'}^2 t^4 \sin^2\beta = \frac{\sin^2\beta}{4}\left(\frac{t}{0.1\ \mathrm{s}}\right)^4 \left(\frac{10^2\ \mathrm{s}^2}{\tau_{nn'}\tau_{n\bar{n}'}}\right)^2 \times 10^{-8}, \tag{19}$$

where β is an (unknown) angle between the directions of $\vec{B}$ and $\vec{B}'$ [170]. Hence, the probability of induced $n \to \bar{n}$ transition can be several orders of magnitude larger than the present sensitivity in direct $n \to \bar{n}$ conversion (7). Once again, for achieving such enhancement, 10 orders of magnitude or perhaps more, the magnetic field should not be suppressed but one must scan over its values and directions for finding the resonance when magnitudes $B \approx B'$ and angle ϕ is non-zero. In addition, different from direct $n\bar{n}$ mixing, $n \to \bar{n}$ transitions induced via $n \to n'$ and $n \to n'$ mixings has a tiny effect on the stability of nuclei [170].

3.5. Antineutron–nucleon annihilation

The distribution of final states following $\bar{n}$ annihilation in target nuclei is of critical importance for understanding the needs of the annihilation detector system for the $n \to \bar{n}$ (and $n \to n' \to \bar{n}$) searches. To date, the target material has been ^{12}C, with four to five pions in the final state, but their intranuclear origin and their cascade dynamics thereafter can be significant. Studies of

Table 1. A list of average multiplicities M from experimental data and simulations taking into account $\bar{p}$ annihilation branching ratios [124, 172] while also considering intranuclear (anti)nucleon potentials with associated nucleon mass defects and nuclear medium response. Based on simulations of 10 000 events. Measurements of proton and neutron multiplicities were not made.

	$M(\pi)$	$M(\pi^+)$	$M(\pi^-)$	$M(\pi^0)$	E_{tot} (MeV)	$M(p)$	$M(n)$
$\bar{p}$C experiment	4.57 ± 0.15	1.25 ± 0.06	1.59 ± 0.09	1.73 ± 0.10	1758 ± 59	—	—
$\bar{p}$C simulation	4.60	1.22	1.65	1.73	1762	0.96	1.03

these effects have been made [124, 171, 172]. In this approach, a model of elementary $\bar{p}N$ annihilation is used, described in detail in [124, 171], taking into account $\sim$100 annihilation channels for $\bar{p}p$ and $\sim$80 channels for $\bar{p}n$, including heavy resonances. The simulations of the elementary annihilation agree well with $\bar{p}$–p interaction data sets (for instance, see table 2 of [124]). For $\bar{n}N$ annihilation, it is assumed that annihilation channels for $\bar{n}n$ are identical to $\bar{p}p$, and annihilation channels for $\bar{n}p$ are charge-conjugated to $\bar{p}n$. Thus, annihilation processes can indeed be considered for $\bar{n}p$ and $\bar{n}n$. Further computations model the particle transport through the nuclear medium (final state interactions). The proposed model for $\bar{n}$ ^{12}C was tested on available experimental data sets from $\bar{p}$ ^{12}C annihilations at rest, showing good agreement.

Table 1 shows the simulated and measured particle multiplicities following $\bar{p}$ ^{12}C interactions based on 10 000 Monte Carlo events. Pionic states dominate after the decay of heavy resonances and are in good agreement with experimental data. The total energy of the final state particles is also shown, for which the measurement is well reproduced by the calculations.

The momentum distribution of positively charged pions is shown in figure 2. The momentum peaks around $\sim$250 MeV, albeit within a broad distribution which extends up to around 1000 MeV. The data are reasonably well described by the simulation. The figure also shows the distribution of kinetic energies of protons. As before, the data are well described. The contribution from evaporative protons is also shown and is seen to correspond to the data quite well even toward lower values of kinetic energy ($\sim$20 MeV). Given the agreement with the data observed in figure 2, there is some measure of confidence in the simulations of extranuclear $\bar{n}$ ^{12}C final states.

We see from figure 3 the expected final state $\pi^{0,\pm}$ counts and momentum spectra arising from a slow $\bar{n}$ annihilating on ^{12}C nucleus. One expects approximately four to five pions of various charges to enter the detector, where it is critically important to identify π^0 species due to their proportionally high population. Because these are so short lived, it is incumbent on the detector to capably reconstruct the π^0, as well as track $\pi^{\pm}$, over a rather large range of momenta.

Figure 4 shows the total momentum of the final state system of emitted mesons and photons versus the system's total invariant mass. Owing to nuclear effects (final state interactions, rescattering, absorption), the final state invariant mass distribution for mesons and photons can fall to less than 1 GeV, lower than would be expected for a naive $\bar{n}N$ annihilation at around 1.9 GeV. The figure also shows the distribution of invariant mass arising only from original annihilation mesons before and after transport. The kinematic distributions shown in figures 2–4 have implications for the detection strategy of annihilation events, particularly affecting the expected signal efficiency.

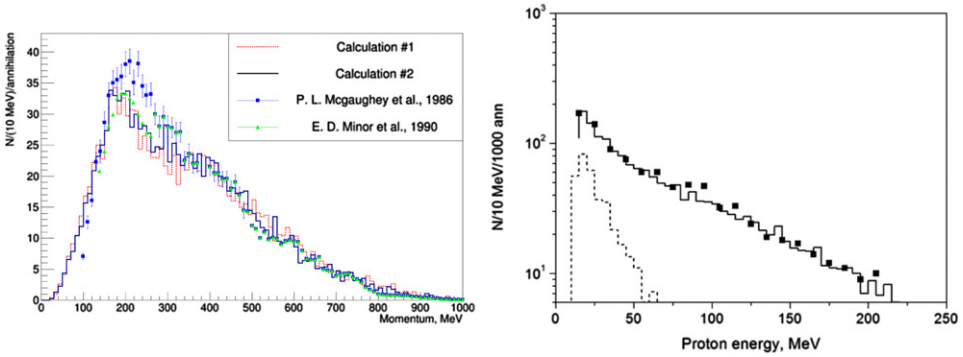

Figure 2. Final state kinematic distributions for 10 000 $\bar{p}$C simulated annihilation events at rest. Left: momentum distribution of positively charged pions [124]. The solid histogram shows the distribution generated from the simulation mentioned in table 1, while the red histogram shows the behavior when (anti)nucleon potentials and mass defects are not considered. Available pertinent data are shown. Right: energy distribution of final state protons [172]. The solid line shows the full spectrum and the dotted line represents the contribution from evaporative processes. All points are taken from experimental data in [173, 174]. See [124, 172] for detailed discussions. Based on simulations of 100 000 events. Reproduced from [125]. CC BY 4.0.

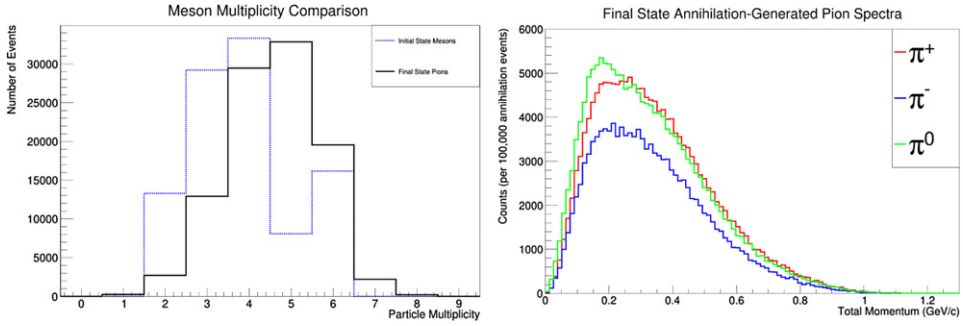

Figure 3. Left: the initial $\bar{n}$ ^{12}C annihilation-generated meson multiplicity is compared to the predicted final state $\pi^{0,\pm}$ multiplicity. The apparent shift occurs due to decays of heavy resonances [172], which can also produce γs and are not considered here, as well as meson absorption during the intranuclear cascade. From truth-level, on the average, one expects $\sim$4.6 final state $\pi^{0,\pm}$s. Right: the final state spectra of all pions originating from $\bar{n}$ ^{12}C annihilation is shown, generally ranging from $\sim$0–1 GeV/c. The tagging and reconstruction of these pions will constitute the heart of any experimental capability to identify $\bar{n}$ appearance. Based on simulations of 100 000 events.

4. Searches for neutron conversions

4.1. Previous searches for $n \to \bar{n}$

As illustrated in figure 5, free (or extranuclear) searches consist of a beam of focused free neutrons propagating in field-free (or quasi-free) regions to an annihilation detector at which any antineutrons would annihilate with a thin target, giving rise to a final state of charged pions and photons. Searches for free $n \to \bar{n}$ oscillation have taken place at the Pavia Triga

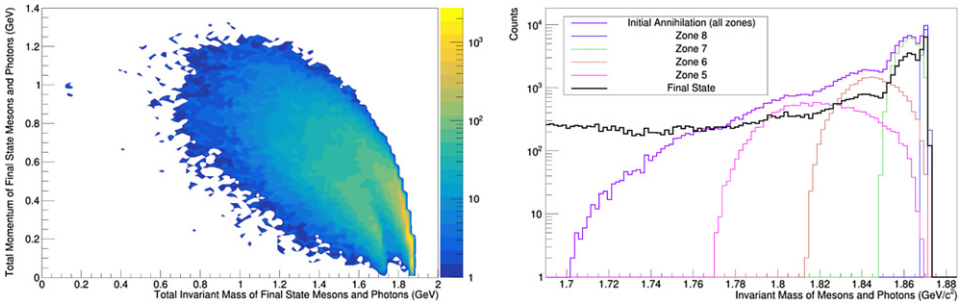

Figure 4. Final state kinematic distributions following an extranuclear $\bar{n}$C annihilation for 100 000 events using an antineutron potential as described in [124] (calculation no. 2 therein). Left: the final states' sum total momentum of emitted *pions and photons* versus the total invariant mass of the pion and photon system. For similar figures and discussions, see [53]. Right: one dimensional distributions of the same invariant mass as at left. The purple histogram characterizes the initial state's invariant mass of all annihilations over the whole of the nucleus. The black histogram shows the final state pions and photons' after undergoing nuclear transport. Other colors show some of the origins of the distribution's structure, with the leftward march of the distributions arising from the annihilation taking place further and further into the interior of the nucleus where final state interactions and isotropically distributed Fermi motion effects can become large within zones of smaller radii (only some zones are shown). For further details, see [124, 172]. Based on simulations of 100 000 events.

Mark II reactor [109, 110] and at the ILL [37, 111]. The latter ILL search [37] provides the most competitive limit for the free neutron oscillation time: $\sim 8.6 \times 10^7$ s.

The figure of merit (FOM) of sensitivity for a free $n \to \bar{n}$ search is best estimated not by the oscillation time sensitivity but by the quantity below:

$$\mathrm{FOM} = \sum_i N_{n_i} \cdot t_{n_i}^2 \sim \langle N_n \cdot t_n^2 \rangle, \tag{20}$$

where, for velocity spectrum bins i, N_{n_i} is the number of neutrons per unit time reaching the annihilation detector after t_{n_i} seconds of flight through a magnetically protected, quasi-free conditioned vacuum region. As equation (7) shows, the probability of a conversion is proportional to the (transit time)^2. Thus FOM $= \langle N_n \cdot t_n^2 \rangle$ is proportional to the approximate number of the conversions per unit time in a neutron beam which impinge on a target[73].

A high-precision search therefore requires a large flux of slow neutrons produced at a low emission temperature which are allowed to propagate over a long time prior to allow conversions to antineutrons. As shown in the subsequent sections, these conditions are satisfied in searches at the ESS.

Searches for $n \to \bar{n}$ in bound neutrons in large volume detectors look for a signature of pions and photons consistent with a $\bar{n}N$ annihilation event inside a nucleus, as illustrated in figure 5. Searches have taken place at Homestake [115], KGF [116], NUSEX [117], IMB [118], Kamiokande [119], Frejus [120], Soudan-2 [121], the Sudbury Neutrino Observatory [122] and Super-Kamiokande [53, 54]. A signature of pions and photons consistent with an

[73] For comparisons, the ILL search [175] achieved FOM $= 1.5 \times 10^9$ n s^2 after 1 year of operation. Thus, if one were to normalize to such an ILL sensitivity unit, and *if* a single unobserved event had occurred, any change in the FOM would imply a directly proportional change in expected potentially observable events, up to overall ratios in signal efficiencies and operating periods.

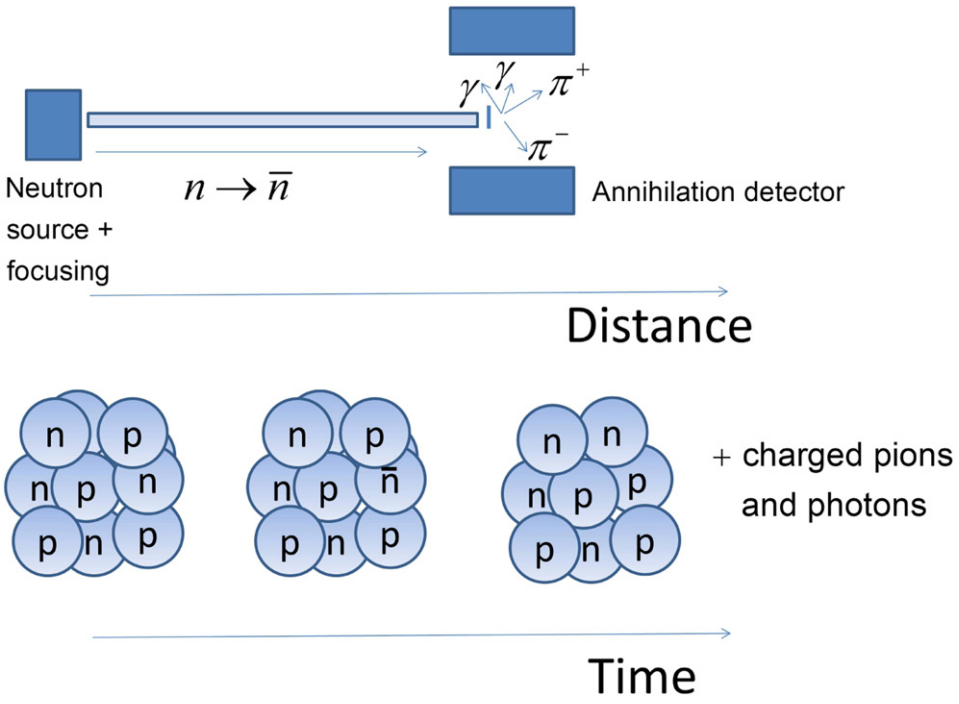

Figure 5. Illustration of the principles of free (top) and bound (bottom) searches for $n \rightarrow \bar{n}$. Each produces observable pions and photons in the final state.

$\bar{n}N$ annihilation event was sought, with Super-Kamiokande providing the most competitive search, for which an inferred free neutron oscillation time lower limit of $\sim 2.7 \times 10^8$ s was obtained. Super-Kamiokande has also searched for dinucleon decays to specific hadronic final states, such as $nn \rightarrow 2\pi^0$ and $np \rightarrow \pi^+\pi^0$, as well as dinucleon decays into purely leptonic and lepton + photon final states [55, 176, 177]. Further limits on BNV decays have been obtained by relating these types of decays [29, 56, 134, 178].

4.2. Previous searches for $n \rightarrow n'$

Two main experimental approaches are used to search for sterile neutrons: measurements of neutrons trapped in a UCN bottle and measurements of beam neutrons[74]. The principles behind these approaches are illustrated in figure 6. There would be anomalous loss of neutrons from the UCN trap via their conversion to sterile neutrons (figure 6(a)). With beam neutrons, experiments can look for the regeneration of neutrons following a beam stop (figure 6(b)), an unexplained disappearance of neutron flux (figure 6(c)) and $n \rightarrow \bar{n}$ via a sterile neutron state. For a comprehensive set of searches with both UCN and beam neutrons, the experiments should scan as wide a range of magnetic fields as possible to induce a neutron–sterile neutron transitions.

[74] In principle, although large volume experiments could have a sensitivity to sterile neutrons, searches for sterile neutron-induced destabilized neutrons are problematic. Any interpretation of results would depend strongly on the composition and properties of the dark sector to which a sterile neutron would belong [17].

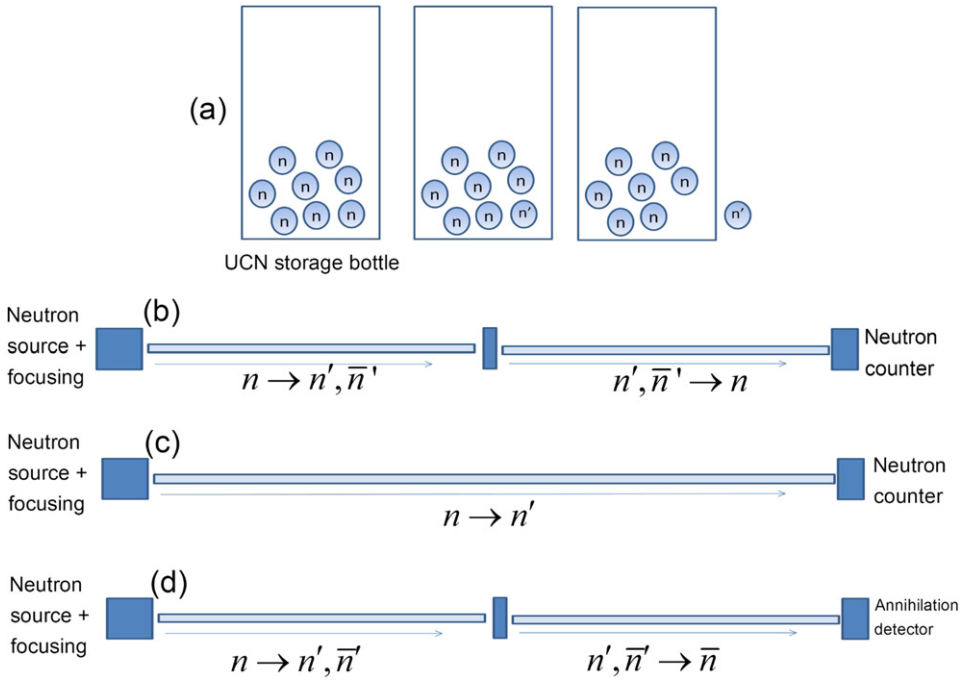

Figure 6. Illustration of the principles of searches for sterile neutron oscillation searches. In the UCN trap (a), it is possible that neutrons effectively disappear, possibly lowering the measured values of the neutron lifetime. For neutron beams, both disappearance (b) ($n \to n'$) and regeneration (c) ($n \to \{\bar{n}, n'\} \to n$) search modes are possible. Another possibility (d) is regenerative in style, though instead leads to further mixing to an antineutron ($n \to \{\bar{n}, n'\} \to \bar{n}$), requiring an annihilation detector just as shown in figure 5. Each regeneration mode requires a neutron absorber to be placed at the halfway point of the beamline, preventing all ordinary neutrons from proceeding downbeam while permitting sterile species to pass unencumbered.

Early searches for sterile neutrons were performed using UCN gravitational storage traps to correlate the possible disappearance of neutrons with the variation of the laboratory magnetic fields [40, 41, 43, 44, 179], assuming that Earth's magnetic field should be compensated to near zero (to satisfy the quasi-free condition) to permit the $n \to n'$ process to occur. With this assumption, the best limit for a free oscillation time $\tau_{n\to n'}$ was obtained by [44], where $\tau_{n\to n'} \geqslant 448$ s (90% CL). More recent measurements and analyses [42, 45, 47] have accounted for the possibility of a modest sterile sector magnetic field by including a wider variation of the laboratory magnetic field $\mathbf{B}$ in the UCN traps. From the analysis of all existing UCN experimental data, the lower limits on $\tau_{n\to n'}$ as a function of $|\mathbf{B}'|$ were obtained [46] in the range of tens of seconds for the sterile sector magnetic fields less than $\sim$0.3 G. However, one UCN experiment [41, 44] reanalyzed in [45] has reported a non-zero asymmetry with a significance of 5σ in the storage time of unpolarized neutrons in a Be-coated trap when a laboratory magnetic field was regularly changed from $+0.2$ G to -0.2 G. This anomalous result was interpreted [45] as an $n \to n'$ oscillation signal with the asymmetry caused by the variation of the angle β between vectors of magnetic fields of sterile and laboratory fields, $\mathbf{B}'$ and $\pm\mathbf{B}$. Thus, $n \to n'$ transitions with, e.g. $\tau_{n\to n'} \sim 30$ s are not excluded for a region of $|\mathbf{B}'| \sim 0.25$ G.

5. Overview of the ESS

The ESS, currently under construction in Lund [180], will be the world's most powerful facility for research using neutrons. It will have a higher useful flux of neutrons than any research reactor, and its neutron beams will have a brightness that is up to two orders of magnitude higher than at any existing neutron source.

The ESS is organized as a European Research Infrastructure Consortium (ERIC) and currently has 13 member states: Czech Republic, Denmark, Estonia, France, Germany, Hungary, Italy, Norway, Poland, Spain, Sweden, Switzerland and the United Kingdom. Sweden and Denmark are the host countries, providing nearly half of the budget for the construction phase. More than half of the budget from the non-host countries is in the form of in-kind contributions, meaning that the countries are delivering components to the facility (accelerator, target, integrated control system and neutron scattering systems) rather than cash.

The project has been driven by the neutron-scattering community, and the construction budget includes 15 instruments covering a wide range of topics in neutron science. The ESS will also offer opportunities for fundamental physics with neutrons, for instance as described in this paper.

Most of the existing spallation neutron sources use a linear accelerator to accelerate particles to high energy. The particles are stored in an accumulator ring and are then extracted in a short pulse to the spallation target. A notable exception is SINQ at the Paul Scherrer Institute (PSI), which uses a cyclotron that produces a DC beam on the spallation target. The ESS will use a linear accelerator but no accumulator ring, and it will thus have longer neutron pulses. This will allow more neutrons to be produced for a given budget, and for most studies in neutron scattering the long pulses will not be at any disadvantage, often rather the opposite. For experiments in fundamental physics where total integrated flux is a main FOM, the ESS concept is clearly of major benefit.

The high neutron flux at the ESS is also due to the fact that it will have the world's most powerful particle accelerator, in terms of MW of beam on target. It will have a proton beam of 62.5 mA accelerated to 2 GeV, with most of the energy gain coming from superconducting RF cavities cooled to 2 K. Together with a 14 Hz pulse structure, each pulse being 2.86 ms long, this gives 5 MW average power and 125 MW of peak power. For proton energies around a few GeV, the neutron production is nearly proportional to beam power, so the ratio between beam current and beam energy is to a large extent the result of a cost optimization, while the pulse structure is set by requirements from neutron science.

The neutrons are produced when the protons hit a rotating tungsten target. The target wheel consists of sectors of tungsten blocks inside a stainless steel disk. It is cooled by helium gas and it rotates at approximately 0.4 Hz, such that successive beam pulses hit adjacent sectors, allowing adequate heat dissipation and limiting radiation damage. Figure 7 shows a cut-out of the target monolith, having the tungsten wheel in the center. High-energy spallation neutrons are slowed down in an adjacent cold neutron moderator surrounded by a beryllium reflector, exiting the moderator–reflector system to be fed to beam extraction points placed within the monolith wall. The monolith extends to a radius of 5.5 m and contains 3.5 m of steel shielding extending from the beamline opening that are located 2 m after the moderator center.

The neutron radiation dose coming out of the monolith is substantial, and further shielding is needed in the structure referred to as 'the bunker'. The bunker, comprised mainly of concrete, ensures that dose levels at the outer bunker surface are less than 3 μSv h^{-1}. Within the bunker, neutron beams are delivered to multiple instruments, which are distributed in two wide angle regions on both sides of the target area. Neutrons from the monolith are fed into neutron guides in the bunker, pass through the bunker wall and, ultimately, on to ESS instruments. In addition

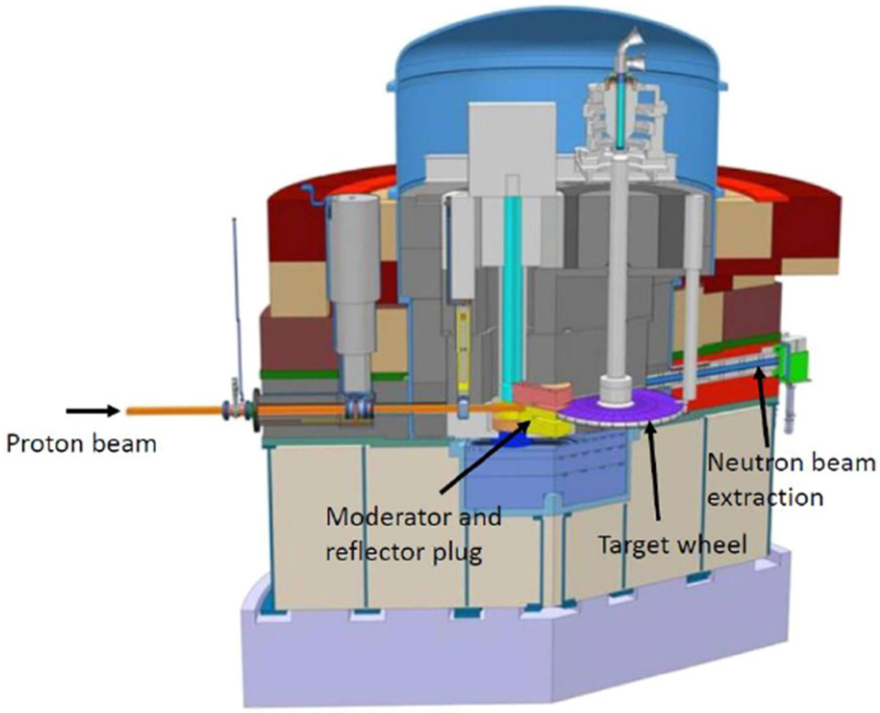

Target monolith

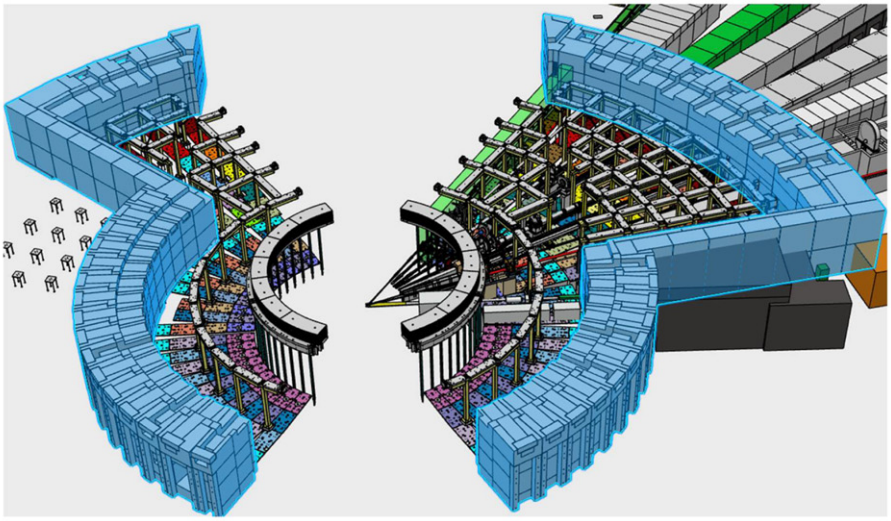

Target monolith and bunker

Figure 7. Top: the ESS target monolith. Bottom: the ESS target monolith and bunker, view from above.

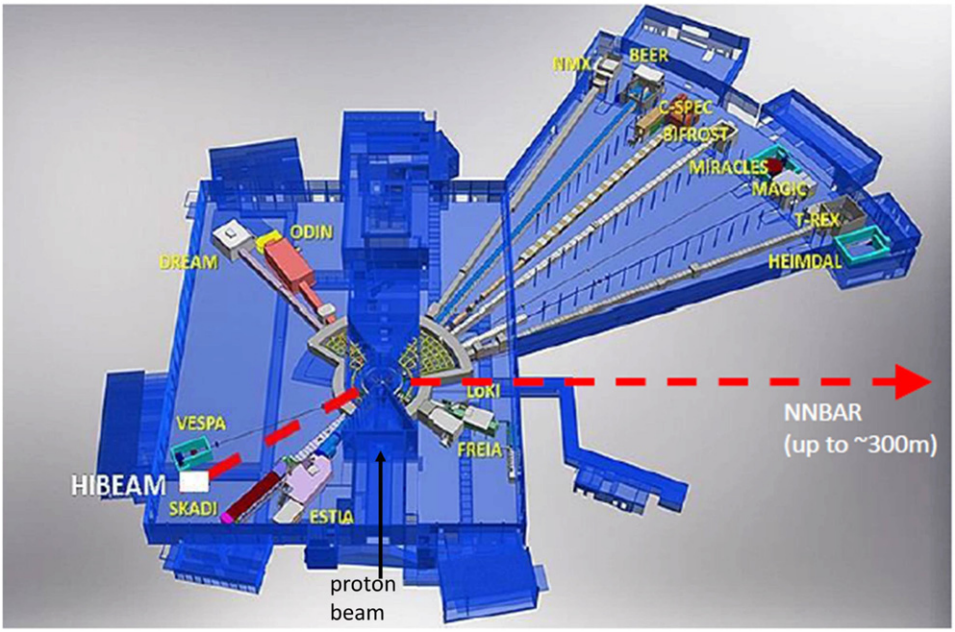

Figure 8. Overview of the ESS, beamlines and instruments. The locations for the proposed HIBEAM and NNBAR experiments are also shown. Reproduced with permission from [183].

to the shielding, the bunker contains components related to the instruments such as guides, choppers, shutters and collimators [181].

In figure 8, an overview of the ESS beamlines and instruments is shown. There are 15 instruments currently under construction at the ESS, representing only a subset of the full 22-instrument suite required for the facility to fully realize its scientific objectives as defined in ESS statutes. In addition to the 15 instruments, a test beamline will be installed among the very first instruments which serves the primary purpose to characterize the target–reflector–moderator system, verifying the performance of the neutron source at the start of operations. It also allows to test and develop relevant neutron technologies. Regarding instruments 16–22, an ESS analysis of the facility's scientific diversity has identified that the addition of a fundamental physics beamline is of the highest priority [182]. The location of the foreseen ESS fundamental physics beamline, HIBEAM/ANNI at beamport E5, is shown. The prospective beamline from the LBP leading to NNBAR is also shown, though would extend far beyond the radii of other instruments.

5.1. ESS timescales and power usage projections

In 2018, a re-optimization of the ESS schedule took place, due mainly to the fact that the original ESS timeline was established before construction began in 2014, and so was impacted by building delays resulting from the ESS's implementation of updated seismic and security standards adopted in recent years within Sweden (and globally). This has primarily impacted the design and construction of the ESS target building, as the strengthened standards were formulated in the aftermath of the Fukushima accident and amid a general increase in concern over global security threats. Following this new baseline, the new plan has the goal to start instrument commissioning in 2022, with early scientific experiments to be carried out on the

Table 2. Target values for the ramp up of the ESS accelerator and instrument availability.

	January 2024	January 2025	January 2026	January 2027
Source operator power (MW)	>0.57	1.25	2	2
Source availability	80%	85%	90%	95%
Source installed capacity (MW)	1	2	2	2
Instruments in operation	3	8	12	15
Days of neutron production	200 minus long shutdown days	200 minus long shutdown days	200	200

first three instruments as soon as possible thereafter. The start of the user program at the ESS is expected to begin in 2023. In the ESS initial stages (July 2022–December 2023), the first neutrons will be produced from the target at very low beam power, where commissioning will include ramp up and testing from accelerator, target and integrated control systems (ICSs). The planned ESS ramp-up time frame is shown in table 2.

5.2. Moderator

The configuration of the ESS neutron source and moderator systems presents excellent opportunities for the fundamental physics research of HIBEAM and NNBAR. This is achieved thanks to the high brightness of the ESS source, the configuration of the beam extraction system and the upgradeability options available for the source, which are attractive for proposed fundamental physics applications. The upper moderator has been designed for the initial suite of 16 instruments (15 neutron scattering instruments, plus the test beamline, located at W11, the same position as NNBAR). The design of the moderator is fully described in [183, 184]. The features of interest for HIBEAM and NNBAR include the following:

(a) The retaining of a monolith configuration for shielding openings and beam extraction ports such that moderators can be placed above and below the tungsten target. Since a design optimization for the initial instrument suite led to the choice of a single (upper) moderator system, this left open an option for future upgrades below the target useful for NNBAR.
(b) The upper cold parahydrogen moderator is 3 cm thick, with a shape optimized for beam extraction in the 42 beamports arranged in two 120° sectors, as seen in figure 9. For HIBEAM/NNBAR, the total available width of the moderator for beam extraction is about 17 cm.
(c) Moderators are placed in plugs that are replaced frequently (the average lifetime of a moderator system at full power is presently assessed to be ∼1 year)
(d) In consideration of possible future upgrades and fundamental physics experiments like NNBAR (which may need a larger moderator system), the inner shielding openings have been designed to be taller at the bottom than at the top of the tungsten target. A cross-sectional view of the region of the target showing the moderators, inner shielding and beam extraction openings is shown in figure 10.

The HIBEAM experiment will use the upper moderator. By the time the experiment starts, it is expected that the Mark II moderator ('butterfly-1'), optimized for maximum cold brightness to all the instruments, will be in place. This moderator's main characteristic is its reduced height (3 cm) compared to its lateral dimensions (∼24 cm), which was found to deliver maximum brightness to the sample areas across the instrument suite [183, 184].

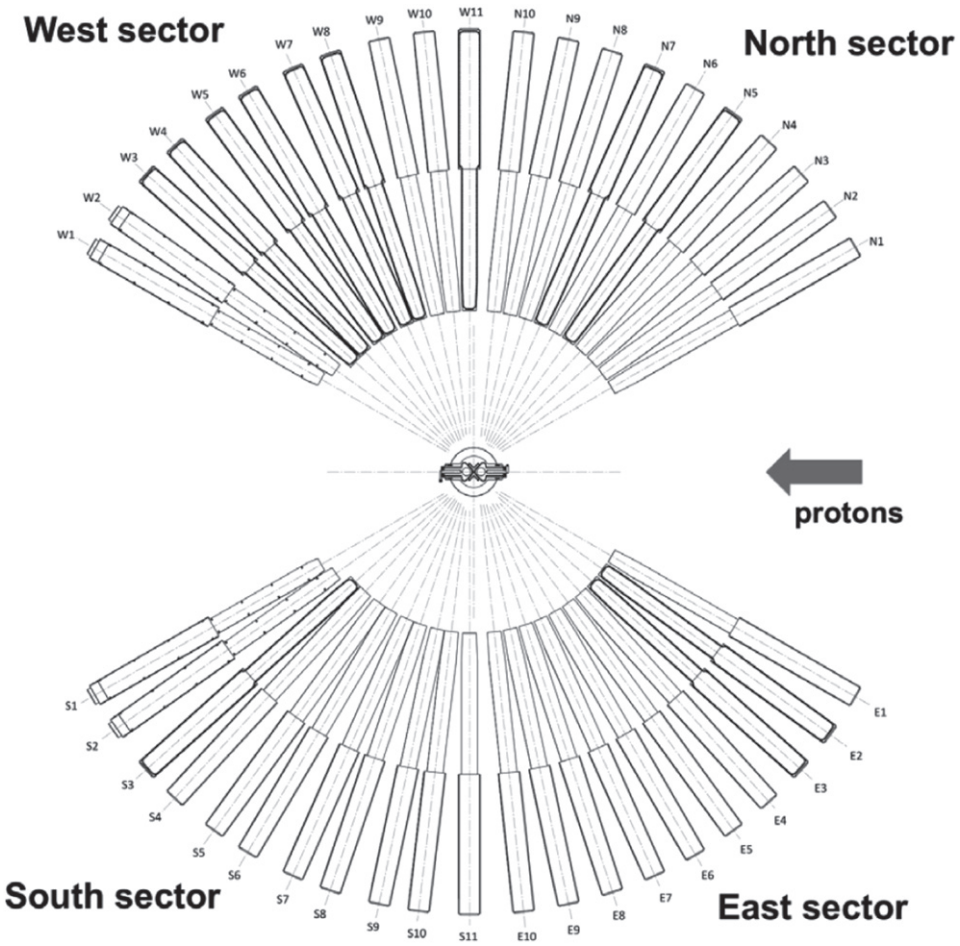

Figure 9. The beamport systems of the ESS arranged around the moderators. Note that neutron beam extraction is possible above and below the target. The location for the proposed HIBEAM experiment is at beamport E5. The location for the proposed NNBAR experiment is at beamports N10, W11 and W10.

A design study, termed HighNESS, has just began for a new cold neutron source and associated instruments at the ESS, including NNBAR. This is funded as a Research and Innovation Action within the EU Horizon 2020 program under Grant Agreement 951782 [185, 186]. A liquid deuterium moderator is envisaged, which provides the high-flux, slow-neutron source required by NNBAR. Such a high-intensity source, with a large emission surface and a wavelength spectrum shifted toward the longer wavelengths, compared to the upper moderator, would be highly beneficial not only to NNBAR, but also to several neutron scattering applications, such as SANS, imaging and spin-echo [183]. The lower moderator to be used by the NNBAR experiment should be tailored specifically for high-intensity neutron extraction, unlike the ESS upper moderator which is generally developed for brightness. This high intensity can be achieved by increasing the dimensions of the moderator. However, it has been shown [183] that a 3 cm parahydrogen moderator already delivers about 80% of the maximum intensity achievable by increasing the moderator height. The only way to have a worthwhile

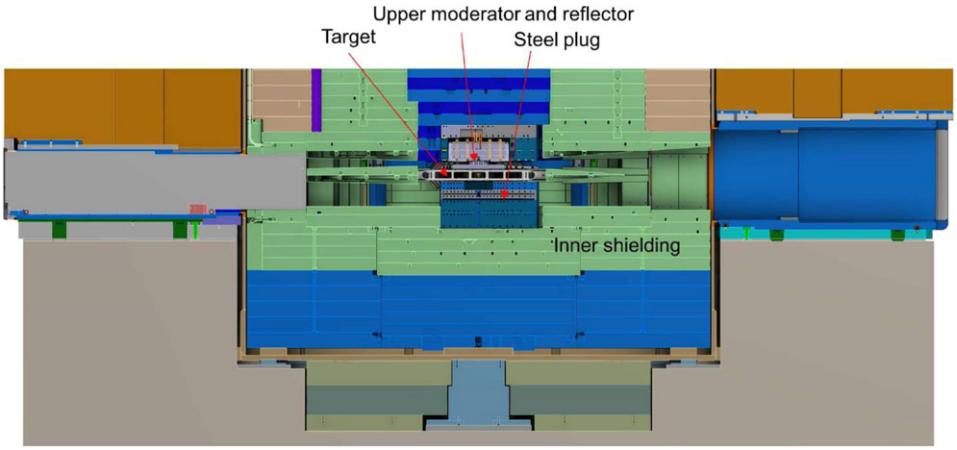

Figure 10. A cross-sectional view of the target/moderator area, including the inner shielding. Reproduced with permission from Mats Segerup and Rickard Holmberg. Reproduced with permission from Mats Segerup and Rickard Holmberg.

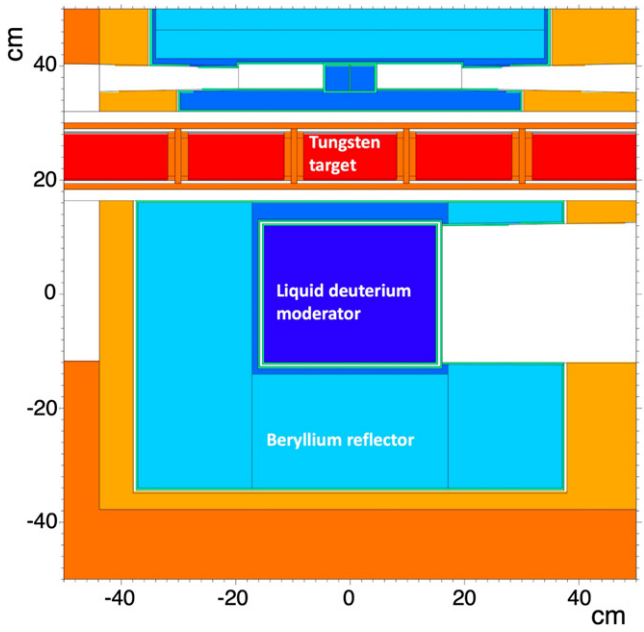

Figure 11. Overview of the liquid deuterium moderator geometry.

increase in intensity is by using a different type of moderator. The choice under study is a liquid ^{2}H moderator, similar to what is used at reactor sources like the ILL (also in dimensions) or at the SINQ facility. Preliminary studies of these options were performed in [187], indicating an increase in intensity of a factor of $\sim$3 compared to a 3 cm flat moderator. This increase in intensity is related to the overall larger dimensions, as well as the negligible neutron absorption

Table 3. Parameters of the upper moderator and possible parameters for the lower moderator of relevance for HIBEAM/NNBAR. Note that the lower moderator's ^{2}H brightness and intensity values are approximate estimates at this stage of research and design, while expected values for the upper moderator are more precise [183].

	Upper	Lower
Moderator temperature	20 K	20 K
Total beam extraction window at moderator face	17×3 cm^2	25×20 cm^2
Moderator time average brightness (E <20 meV)	5×10^{13} n cm^{-2} s^{-1} sr^{-1}	1.5×10^{13} n cm^{-2} s^{-1} sr^{-1}
Moderator time average intensity (E <20 meV)	2.5×10^{15} n s^{-1} sr^{-1}	7.5×10^{15} n s^{-1} sr^{-1}

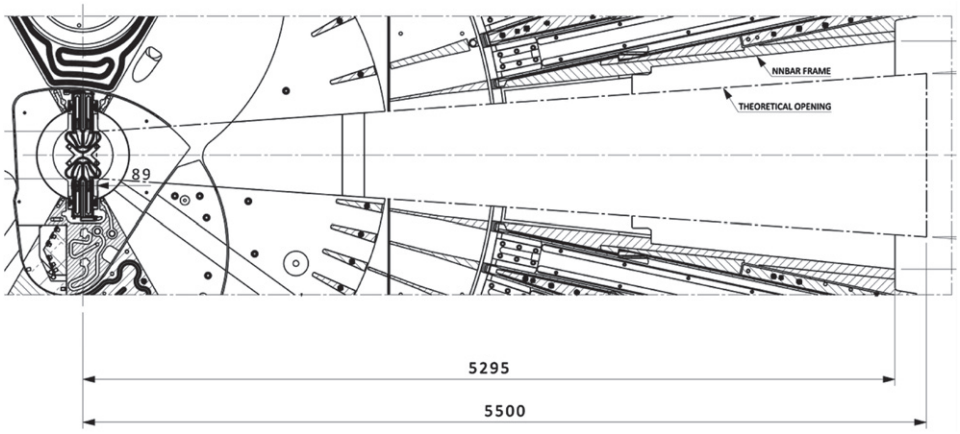

Figure 12. Top view of the NNBAR beamport. Reproduced with permission from Mats Segerup and Rickard Holmberg. Reproduced with permission from Mats Segerup and Rickard Holmberg.

in deuterium. The possible geometry of the lower large ^{2}H moderator is shown in figure 11, which is updated from the originally proposed geometry of reference [184].

Some expected parameters of the neutron source for HIBEAM and NNBAR are listed in table 3.

5.2.1. The large beam port for NNBAR. In the current baseline design of the ESS monolith, a critical provision has been made for the NNBAR experiment. A normal ESS beamport would be too small for NNBAR to reach its ambitious sensitivity goals. Therefore, part of the beam extraction system in the ESS monolith has been engineered so that a large frame covering the size of three beamports will be constructed. Initially, the frame will be filled by three regular-size beamports plus additional shielding for other experiments, including the ESS test beamline. The three beamports can be removed to provide a LBP to NNBAR for the duration of the experiment and eventually replaced at the end of the experiment. Two views of the beam extraction region at the NNBAR beamport are shown in figures 10 and 12, both from the moderator to the monolith exit. At the time of this writing, no other existing or planned neutron facility will have an LBP of similar dimensions, making the ESS the ideal site for a full-scale NNBAR experiment.

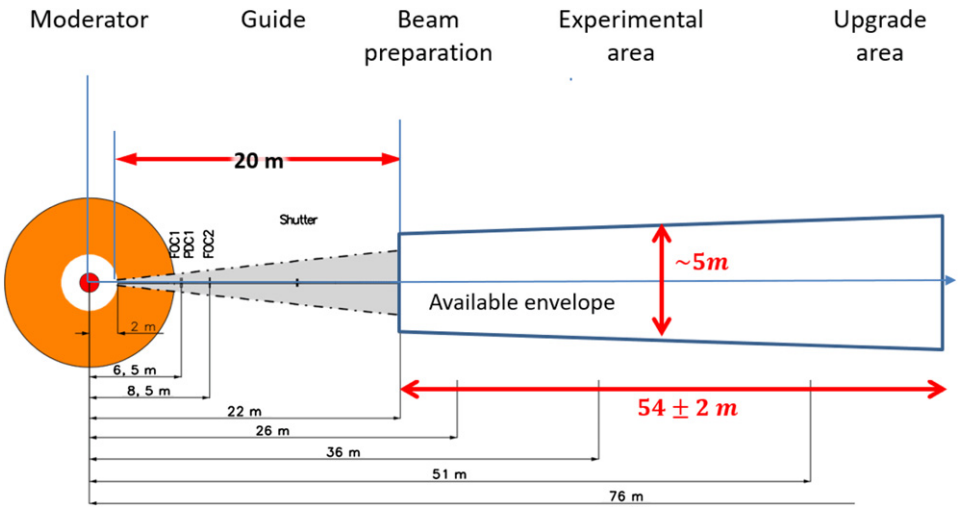

Figure 13. A schematic overview of the ANNI fundamental physics beamline floor plan which would be used in HIBEAM. Reproduced from [39]. CC BY 4.0.

6. ANNI beamline

The search for $n \to \bar{n}$ with a sensitivity $\sim$1000 times higher than in the previous ILL-based experiments [37] remains an ultimate goal of the NNBAR collaboration. Due to the commissioning schedule of the ESS, the floor for the start of construction of $n \to \bar{n}$ experiment might be available no earlier than year 2026 and the designed power of 5 MW could be obtainable after year 2030. The NNBAR collaboration would exploit the opportunity of low-power operation and the commissioning time of the ESS during the intervening years to exploit opportunities at the ESS to search for sterile neutrons at the HIBEAM stage of the experiment using the ESS beamline developed by the ANNI collaboration [39]. As shown in section 2, the physics of $n \to n'$ is close to and possibly generically related to the $n \to \bar{n}$ process. Several smaller scale and relatively inexpensive experiments can be performed in this area. A further goal of HIBEAM is the development of a search for $n \to \bar{n}$, albeit at a likely lower sensitivity than that achieved by the ILL experiment. The pilot experiment will enable detector research and development together with background mitigation techniques, necessary for the full NNBAR experiment.

This section is organized as follows. First, the ANNI beamline is described, followed by the searches for neutron conversion processes involving sterile neutrons.

6.1. ANNI beamline and beam properties

Ample discussion on the properties and usage of the ANNI beamline for fundamental physics searches has been considered in [39]. Figure 13 gives a schematic outline of the ESS/ANNI fundamental physics beamport. Neutrons emerging from the moderator pass through a guide system (figure 14) and then into an experimental area (figure 13) with a length of around 54 m and a width of around 5 m (visualized here without all other experimental apparatuses in the hall). Due to the beam hall size constraints, there would be very limited room to use focusing reflectors to increase sensitivity for n oscillation searches. HIBEAM considerations are thus minimally based on the full-length beamline with possible aperture collimation.

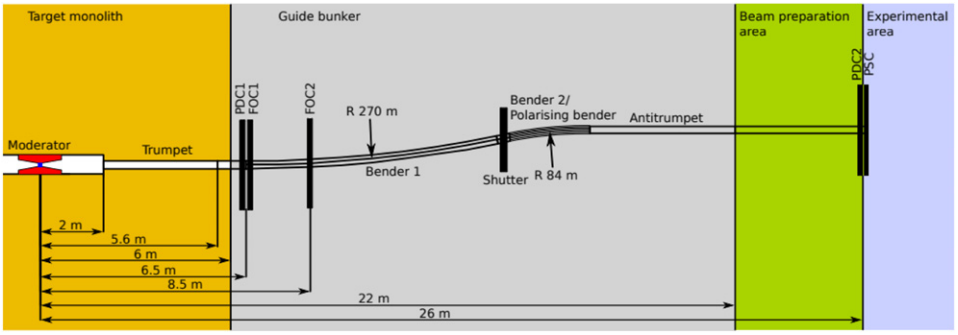

Figure 14. A basic schematic overview of the optimized vertically curved *n* guide system used in the ANNI design preventing direct sight of the cold moderator, thus reducing backgrounds, as discussed in [39]. Reproduced from [39]. CC BY 4.0.

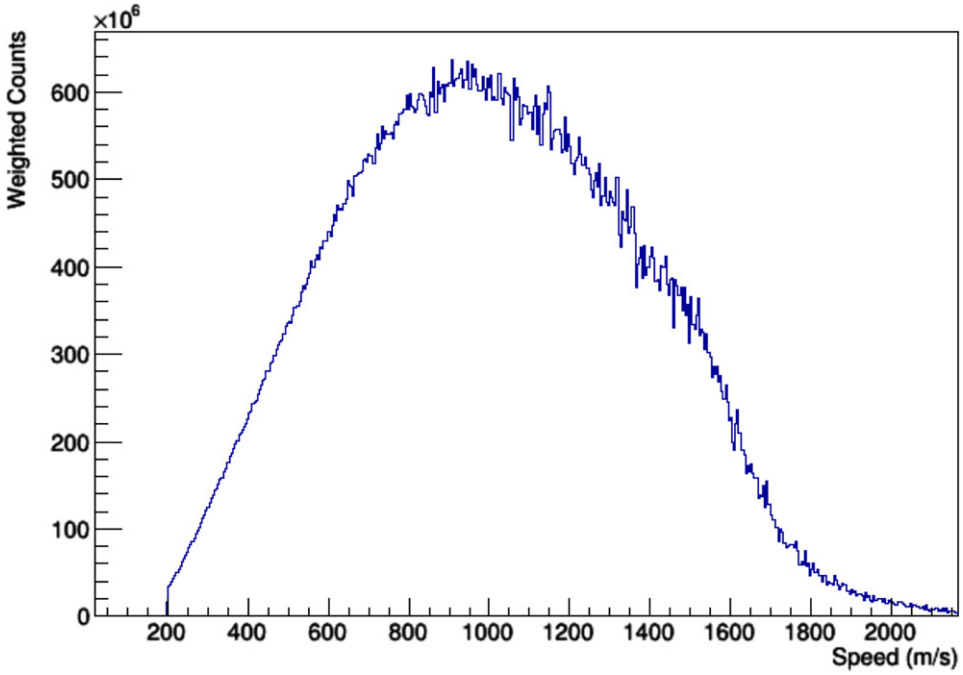

Figure 15. The incident beam velocity spectrum coming from the ANNI/HIBEAM beamport. The results use a simulation event file provided by the authors of [39].

Simulations using the ESS butterfly moderator design in McStas 2.4 [188] have been performed by the ANNI collaboration, fully modeling the *S*-curved *n* guide in a background-reduced, cold-spectrum selected, beam-shape-optimized way [39]. A McStas output of an *n* source file with coordinates, momenta and weights of the neutrons normalized to one initial proton with energy 2 GeV on the ESS tungsten target transported through the ANNI beam optics to the collimator exit at $z = 22$ m was produced. Figure 15 shows the spectrum of velocities of neutrons from this simulation flying through the ANNI beamline.

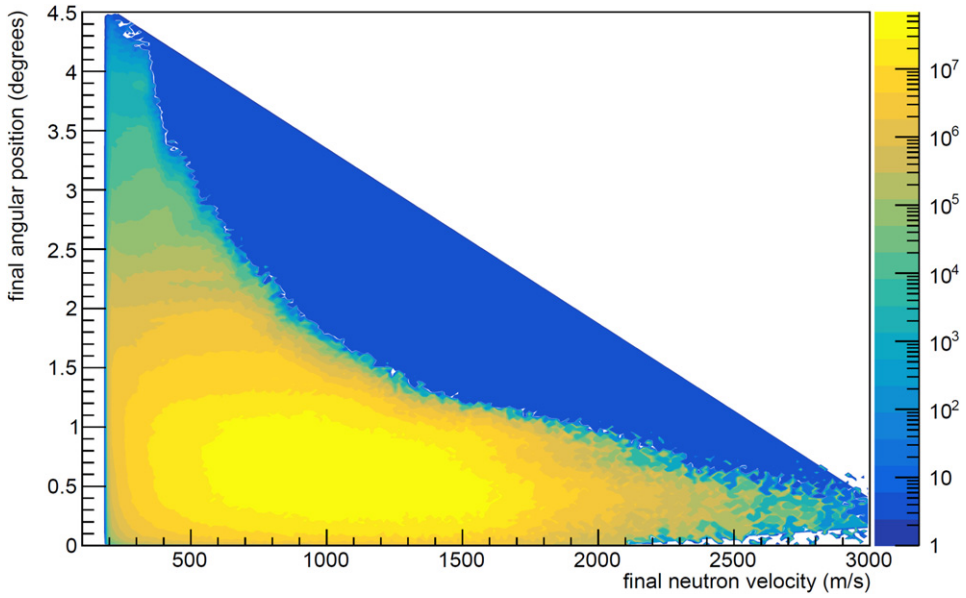

Figure 16. The ANNI beam divergence as a function of velocity at a distance of 50 m from the beamport; gravity is taken into account and the entire flux (irrespective of any virtual detector's $\sim\infty$ size) is considered. The results use a simulation event file provided by the authors of [39], and includes the effects of gravity.

As seen in figure 16, the initial beam characterization shows a large swathe of slow neutrons over the beam length of 50 m having larger divergence at smaller velocities. Most neutrons do not fall outside a 1.5 m radius (angle $\leqslant 1.72$ degree), though even that would constitute an enormous and financially untenable detector. Thus there is a sacrifice of a fraction of the valuable slowest neutrons by choosing a detector with a practical radius of 0.25 m–0.50 m. Assuming 1 MW of operating power, simulations show an absolute beam normalization of 1.5×10^{11} n s^{-1} (at the beamport exit). For a conservatively designed 1 m diameter detector downstream of the 50 m propagation length, this flux becomes 6.4×10^{10} n s^{-1}. This is without the installation of any further beam optimization or neutron reflectors, no lowering of the detector due to gravitational drop or optimization of beampipe shape, and assuming an inherently perfect detector efficiency.

Figure 17 shows a top view of the neutron tracks estimated by Phits due to the interaction of the ANNI neutron beam with the ^{12}C target. Most of the neutrons pass directly through the target—a small fraction are scattered off of it given low n^{12}C cross section and some are absorbed, inducing the emission of $\sim$MeV photons. We take the origin of the coordinate system to be the experimental area, after ANNI's curved guide extraction, i.e. the origin is located in the so-called 'available envelope' as shown in figure 13.

Figure 18 shows a cross-sectional view of the ANNI neutrons at the annihilation target. The observed neutron interference pattern is caused by the different bounce distances the ANNI neutrons take when being transported through the *S*-curved guide.

The capabilities of the HIBEAM beamline can be further contextualized when the full final flux is considered as a function of a detector radius, as seen in figure 19. This hints at the need for greater beam control via *n* reflectors. However, space constraints will limit this prospect.

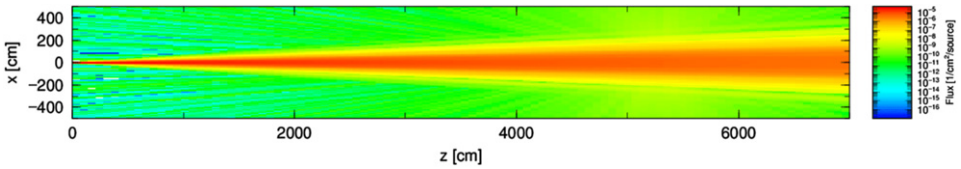

Figure 17. A top view of the ANNI neutron beam tracks obtained by Phits. The origin of the coordinate system is in the experimental area, after ANNI's curved guide extraction. Gravitational effects are not taken into account, but do little to affect this view.

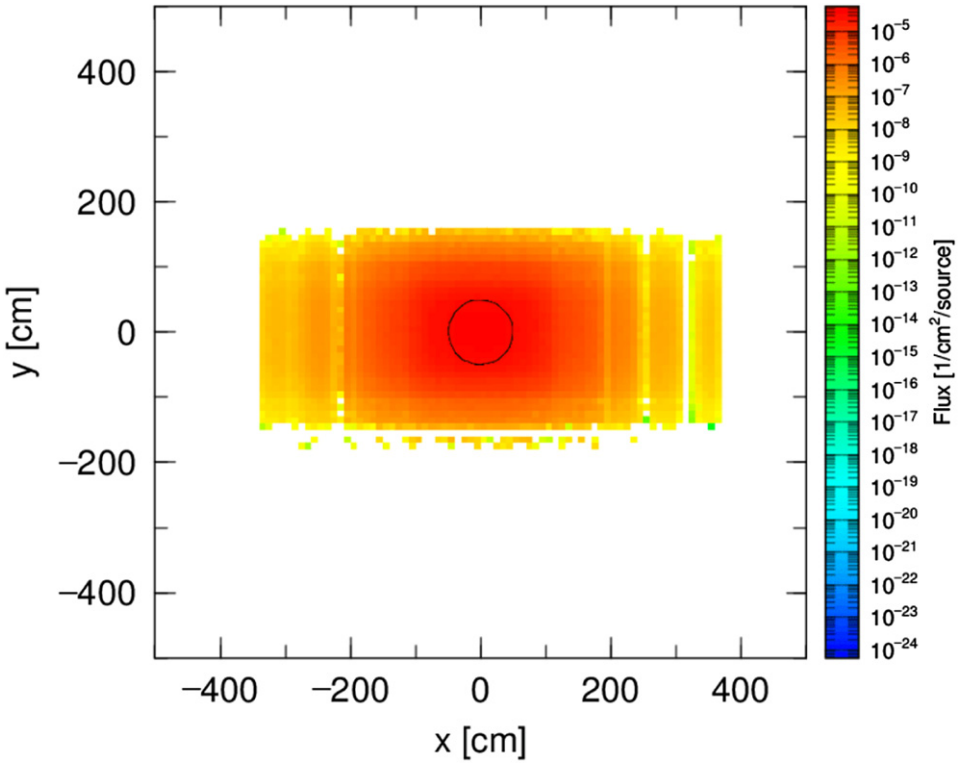

Figure 18. A cross-section view of the target region showing the ANNI neutron beam tracks obtained by Phits. The observed interference-like pattern is due to bounce-to-detector distances along ANNI's *S*-shaped curved guide. The black circle at the origin represents the prospective 1 m diameter ^{12}C target. Gravitational changes to this distribution are not included for simplicity in Phits, but are marginal within the detector region.

7. Searches for sterile neutrons at HIBEAM

The initial steps of the envisaged HIBEAM/ANNI to the NNBAR experimental program is partially based on the theoretical possibilities for $n \to n'$ described in section 3.3. The program will include, but will not be limited to, the following experiments, each able to be performed for relatively short times using the ANNI beamline without full power. Sections 7.1–7.4 (sections

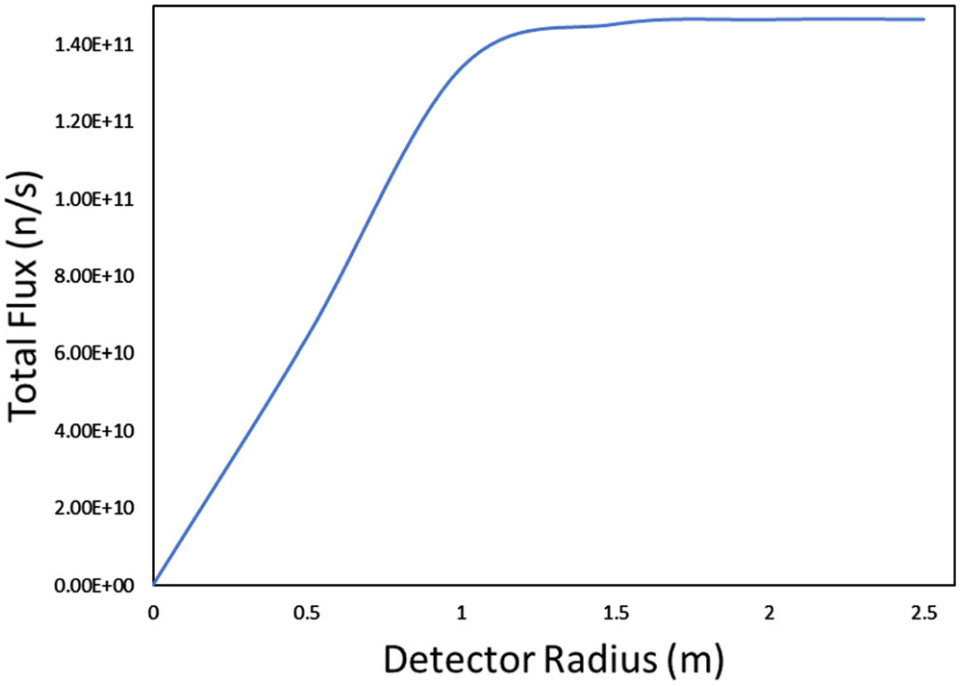

Figure 19. The smoothed total unreflected flux per 1 MW of spallation power for the ANNI beamline as a function of final detector radius assuming 50 m of flight.

7.6 and 7.7) cover searches for evidence of sterile neutrons generated by mass mixing (a non-zero TMM). As shown in this section, by employing complementary configurations for sterile neutron searches, a characterization of the sterile neutron mixing sector can be made in the event of a discovery. Section 7.4 describes a search for neutrons transforming to antineutrons via a sterile neutron state in a regeneration style experiment. This provides a well-motivated opportunity to refine the technical approach to the high-efficiency detection of antineutron annihilation events with small backgrounds. Taken together, the range of envisioned experiments enables potentially multiple discoveries made with one set-up to be supported by an observation of several different signals with a different experimental configuration.

7.1. Search for $n \to n'$ via disappearance

The disappearance of $n \to \{n', \bar{n}'\}$ is sensitive to a scenario in which at least one of the mass mixing parameters $\alpha_{nn'}$ or $\beta_{n\bar{n}'}$ (see equation (18)) is non-zero. The search assumes the presence of an unknown sterile magnetic field $\mathbf{B}'$, which would be matched by a magnetic field in the visible sector.

A schematic overview of the experiment is shown in figure 20. A more detailed diagram showing all relevant apparatus is shown, together with a simpler schematic picture illustrating the basic principles of the search. Neutrons propagate along an aluminum vacuum tube of around 50 m in length, with a varying diameter separated by a window; neutron rates at the start and the end of the propagation zone are precisely measured. The symbol M (left side) represents a current-integrating beam monitor with efficiency 20%–30%. The symbol C (right side) represents a current-integrating beam absorption counter with an efficiency $\sim$100%. The assumed beam intensity used here and for subsequent HIBEAM projections is 6.4×10^{10} ns^{-1}

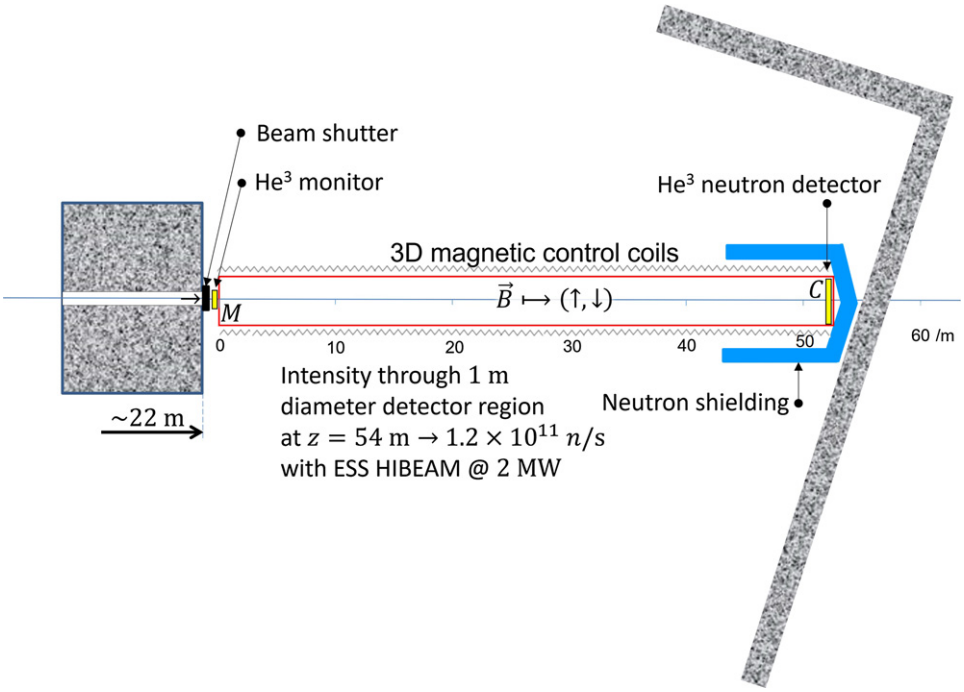

Figure 20. Schematic overviews of the $n \rightarrow n'$ search by disappearance at HIBEAM. The diagram shows the apparatus components and flux values, as well as giving a simplified schematic illustrating the basic principles of the search. The symbol M represents a current-integrating beam monitor with an efficiency of ∼20%–30%. The symbol C represents a current-integrating beam absorption counter with an efficiency ∼100%. The 3D-adjusted magnetic field can be applied in neutron flight volume with sufficient uniformity and with the possibility to vary the field to an exactly opposite direction (shown by the up and down arrows within the parentheses).

per 1 MW of operating power [39], scaling linearly thereafter. The sterile magnetic field is assumed to be constant, uniform and not exceeding the magnitude of Earth's magnetic field [18]. The measurements of the change of neutron flux will be made for a range of axial laboratory magnetic field values in different directions in a tetrahedral configuration for a range of -0.5 G to $+0.5$ G with a step of only a few mG, a few times less than the resonance width to achieve adequate resolution of the resonance trough. Thus, the counting rate (determined by charge integration) of the counter C in figure 20 will be controlled by the magnitude of magnetic field. The charge integrating counter M will monitor variations of the beam intensity independent of variations of magnetic field.

The detection of a resonance would appear as the reduction of the total counting rate in the C/M ratio vs $|\mathbf{B} - \mathbf{B}'|$. This experimental signal is sensitive to multiple parameters of the sterile sector. From this measurement, a limit on the mass mixing parameter ϵ, or the $n \rightarrow n'$ oscillation time $\tau^{\rm dis}_{n \rightarrow n'}$, can be extracted. A positive signal would indicate not only the existence of the sterile state n', but also the existence of sterile photons γ', required for the transformation to occur at non-zero $\mathbf{B}'$. With more detailed scans, the three-dimensional direction of the sterile magnetic field $\mathbf{B}'$ can be established. As also shown in references [162, 189], due to its first-order nature, the disappearance method is the most statistically sensitive approach for setting a limit on ϵ or $\tau^{\rm dis}_{n \rightarrow n'}$.

Measurements of $n \to n'$ disappearance with a cold n beam will require full magnetic control in the flight volume of the vacuum tube shown in figure 20. The 3D magnetic field should be uniform and be preset to the desired 3D value in any direction with accuracy better than 2 mG in the range from 0 mG to ∼500 mG, presenting a technical challenge for this experiment. Another challenge will be the construction of the charge-integrating counters which can achieve a measured charge proportional to the n flux with high accuracy, typically 10^{-7}. It has been recently shown [190] that such stability and accuracy can be achieved with a ^{3}He detector in charge-integration mode. Measurements for positive and negative **B**-field magnitudes would allow the determination of the oscillation time $\tau^{\rm dis}_{n\to n'}$ independently of the value of the unknown angle β between the vectors **B** and **B**′, as well as an estimate of the angle β itself.

The dependence of the sensitivity of $n \to n'$ searches on the properties of the beam and apparatus can be rather complex given the regenerative nature of the oscillation under certain magnetic field conditions, n monitor efficiencies and environmental background rates. The sensitivity for low magnetic field disappearance in the absence of visible resonance signal was best (if briefly) discussed in [162], but is reiterated here. For disappearance, the main dependencies concern the bare and square-normalized integrals of the neutron velocity spectrum, $S(v)$:

$$J_0 = \int S(v)\mathrm{d}v, \qquad J_2 = \int \frac{S(v)}{v^2}\,\mathrm{d}v, \tag{21}$$

which are then used to calculate the lower limit for the $n \to n'$ oscillation time, $\tau^{\rm dis}_{n\to n'}$

$$\tau^{\rm dis}_{n\to n'} > \left(\frac{J_2\sqrt{J_0 T\epsilon}}{J_0}\cdot\frac{L^2}{2}\cdot\frac{1-1.7\epsilon+0.76\epsilon^2}{g\sqrt{1-\epsilon}}\cdot\frac{\sqrt{2K}}{\sqrt{2+K}}\right)^{\frac{1}{2}}, \tag{22}$$

where T (s) is the accumulated time for each individual magnetic field measurement point, ϵ is the n-monitor efficiency (taken to be, e.g. 30%), L (m) the length of magnetically controlled flight, the g-factor parameterizes the confidence level (for instance, $g_{95\%} = 3.283$) obtained from statistical Monte Carlo simulations and K is the number of 'zero-effect' measurements (e.g. at magnetic field $B = 0$) exceeding the time T for the effect measurement by factor K. This calculation is based on the single maximum deviation of one of the $+B$ and $-B$ folded together measured points from the mean value of 200 individual measurements of the ratio C/M. With appropriate calculation of J_0 and J_2 (see equation (21)), equation (22) can be used for scaling different measurements and configurations at the same beamline. However, better limits can be obtained with more detailed analysis based on the line shape fit to experimental magnetic field scan data, as well as beam pulse timing.

The structure of equation (22) is mainly analytical in origin, though their dependence upon factors of g was ascertained by thousands of independent Monte Carlo experiments. To obtain signal sensitivity to a 95% CL with 200 separate magnetic field point measurements and an additional 25 background runs with equidistributed run folding over a finite magnetic field range (e.g. $[-200, 200]$ mG), a (conservative) background of 1 n s^{-1}, a 30% n monitor efficiency and two 25 m magnetically controlled sections of beamline, the sensitivity in oscillation time $\tau_{n\to n'}$ can be calculated for various detector radii over different periods of running without any exploitation of the pulsed beam time structure. One ESS operating year is considered to be approximately 200 days (see table 2) when discounting for routine maintenance and seasonal shutdowns. The sensitivity of the disappearance method as a function of detector radius for $\tau^{\rm dis}_{n\to n'}$ is shown in figure 21 together with sensitivities for regeneration modes (discussed in sections 7.2 and 7.3).

Figure 22 shows the current limits from trapped UCN experiments together with the expected sensitivity of the HIBEAM experiment (in the disappearance mode) after 1 year's

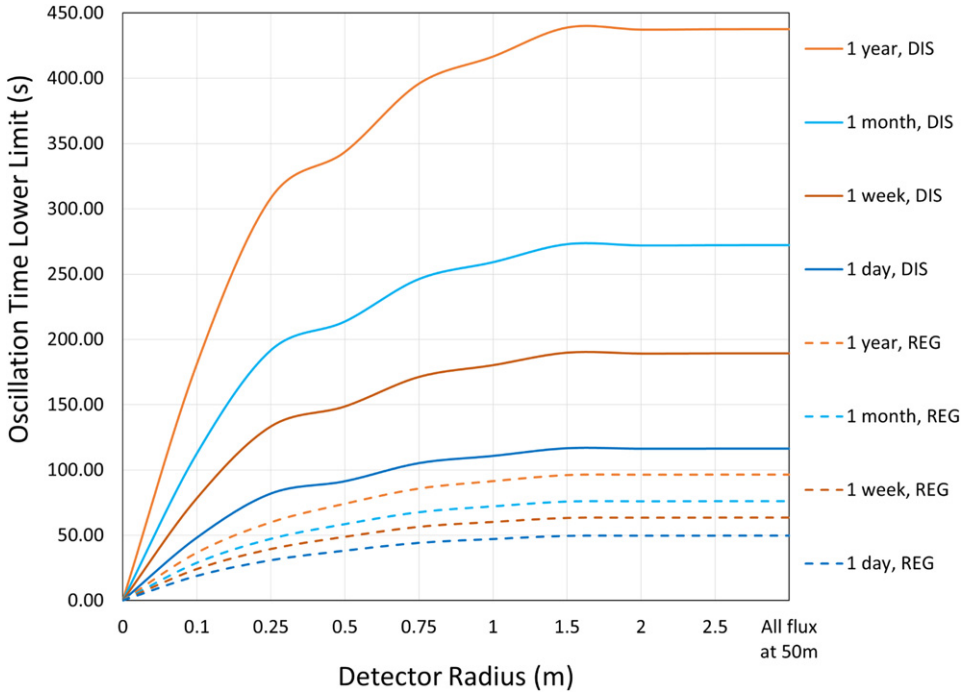

Figure 21. Sensitivity at 95% CL for the discovery of $\tau^{\text{dis}}_{n\to n'}$ (disappearance, 'dis') and $\tau^{\text{reg}}_{n\to n'}$ (regeneration, 'reg') for various detector radii for the nominal 1 MW HIBEAM/ANNI flux at 50 m. A background rate of 1 n s^{-1} is assumed for the regeneration search. Plots have been smoothed.

ESS running for a power usage of 1 MW. Increases in disappearance sensitivity of greater than an order of magnitude are possible depending on the value of the magnetic field used. It can be seen that HIBEAM covers a wide range of oscillation times for a given magnetic field value (up to and beyond an order of magnitude), many of which are unexplored by UCN-based experiments, and remain free of the model assumptions of those searches. In the limit of a vanishing TMM, the sensitivity increases quadratically with the observation time. However, the possible contribution of a TMM complicates this picture (section 3.3). For simplicity, the FOM of sensitivity when comparing experiments is therefore taken here to be the oscillation time.

It should be noted that the interpretations and limits rely on the experimental assumptions, which may be poorly understood for neutron collisions on UCN material trap walls [161]. This source of systematic uncertainty can be removed by performing dedicated searches with propagating cold neutrons in a magnetic field, as planned for the HIBEAM experiment.

High-precision searches for $n \to n'$ are also being pursued using UCN at the PSI by the nEDM collaboration [191], albeit for the magnetic field range $|\mathbf{B}| < 0.2$ G so far considered. A series of searches for $n \to n'$ conversions, due to various processes along a beamline (e.g. figure 6), are planned at the High Flux Isotope Reactor (HFIR) at Oak Ridge National Laboratory [189, 192]. The higher beam intensity of the ESS and the longer available flight paths will allow exploring these mechanisms with higher sensitivity at the ESS than at the HFIR reactor.

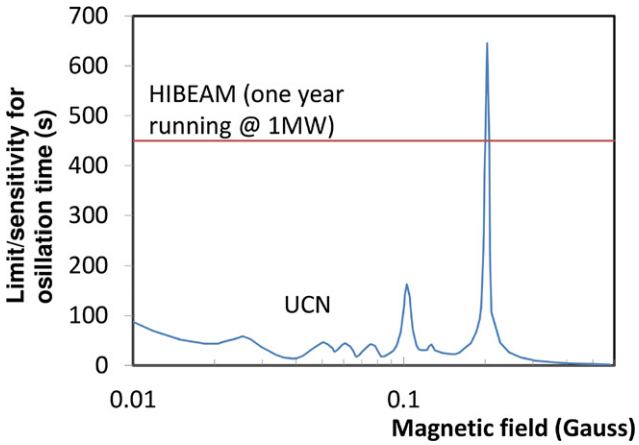

Figure 22. Excluded neutron oscillation times in blue for $n \to n'$ disappearance from UCN experiments [40, 42, 44–47] as a function of the magnetic field $\mathbf{B}'$. The projected sensitivity for HIBEAM (disappearance mode) is also shown in magenta for 1 year's running at the ESS assuming a power of 1 MW.

7.2. Search for the regenerative $n \to n' \to n$ process

The regeneration search derives from a similar theoretical basis as the disappearance search [162, 189], though corresponding to a two-stage (second-order) process with a consequently quadratically smaller probability. In the first stage, the $n \to n'$ transformation takes place in an intense cold n beam at the quasi-free environment limit corresponding to $|\mathbf{B} - \mathbf{B}'| \sim 0$. The largely untransitioned n beam will be blocked by a high suppression beam trap, while the remaining sterile n' will continue unabated through the absorber; in a second volume behind the absorber (stage two), maintaining the same conditions of $|\mathbf{B} - \mathbf{B}'| \sim 0$ as the section before it, the $n' \to n$ transformation produces detectable ns with momentum conserved, as though the totally absorbing wall were not present at all. The resonance behaviour depends primarily on the magnitude of the laboratory $\mathbf{B}$; if the vectors of $\mathbf{B}$ and $\mathbf{B}'$ are not well aligned, i.e. the angle βZ0, the oscillation can still occur with somewhat reduced amplitude [18]. This feature provides a robust systematic check for the experiment: oscillations can be turned off simply by changing the magnitude of $\mathbf{B}$ out-of-resonance in the volume before and/or after absorber. Taking measurements at the positive and negative magnitudes of the field $\mathbf{B}$ in both volumes (four combinations) allows for a determination of the oscillation time independent of the angle β.

A schematic overview of the principle of the regeneration experiment is shown in figure 24. The lowest possible n-background rate in the counter R will be important for a high sensitivity of regeneration search in $\mathbf{B}$-scan, and sufficiently shielding R represents an important challenge for this measurement.

The observation of the resonance in the $\mathbf{B}$-scan would be defined by a sudden appearance of regenerated ns when the $\mathbf{B} - \mathbf{B}' \approx 0$ condition in both volumes is met. Like with disappearance, a positive signal would be a demonstration of the $n' \to n$ transformation as well as the existence of the sterile n' and γ'. The requirement of matching conditions in both volumes ensures this type of measurement is significantly more robust to systematic uncertainties that could cause a false signal to be observed and provides an unambiguous test of that hypothesis.

For the regeneration experiments, in the absence of an observed signal above background level, an upper limit on the oscillation time $\tau^{\text{reg}}_{n\to n'}$ can be established from a statistical analysis. This limit was parameterized in [162] through the quartic-normalized integral of the velocity spectrum

$$J_4 = \int \frac{S(v)}{v^4}\,\mathrm{d}v \tag{23}$$

providing the following estimate for the oscillation $n \to n'$ time

$$\tau^{\text{reg}}_{n\to n'} > \left(\sqrt{4T}\cdot\frac{L^4}{4g\sqrt{\bar{n}_b}}\cdot J_4\right)^{\frac{1}{4}}, \tag{24}$$

where $\bar{n}_b$ is the average background rate in the detector R (see figure 24) in n s^{-1}. This calculation is again based on the single maximum deviation of one of the folded magnetic scans of 200 measurements and T is time for one individual measurement. Running over possible values of this background rate, the behavior of the upper oscillation limit can be constructed and is shown in figure 23. It should be noted that the regeneration mode searches are susceptible to environmental background rates only due to full beam absorption at the halfway point of the beamline. From equation (24), it can be seen that the length L of each of two vacuum tubes in the regeneration scheme is the only parameter that can essentially increase the limit for $\tau^{\text{reg}}_{n\to n'}$. The regeneration oscillation time sensitivity is lower for the same running time than for the disappearance mode as the former (latter) is a two-transition (single-transition) process. However, both processes are complementary with different experimental configurations and neither sharing the same sets of experimental uncertainties. Furthermore, any observation in the disappearance mode could be verified by a regeneration experiment running for a longer time.

7.3. Search for $n \to \bar{n}' \to n$

As discussed in section 3.3, the symmetry between ordinary matter and mirror matter in general allows a range of transformations between the visible and sterile neutron sectors, beyond the simple $n \to n'$ process tackled in sections 7.1 and 7.2. A neutron can be transformed into a mirror (sterile) antineutron which then regenerates back to a detectable n state: $n \to \bar{n}' \to n$. Since the angular momentum of the neutron is conserved, the magnetic moment of the mirror antineutron will be oppositely aligned to the magnetic moment of the sterile neutron due to the mirror CPT theorem. Therefore, a resonance should be observed when magnetic fields in the first and second flight tubes are opposite in direction. This field configuration is included in the anticipated set of measurements shown in figure 24. This search will therefore be made as a complement to $n \to n' \to n$ discussed in section 7.2 and with a similar sensitivity.

7.4. Search for $n \to \bar{n}$ by regeneration through mirror states

Searches for $n \to \bar{n}$ assume that the transformation occurs via mixing with a non-zero mass amplitude $\varepsilon_{n\bar{n}}$ term; this necessitates magnetic shielding in a search. However, $n \to \bar{n}$ can also arise due to the second-order oscillation processes: $n \to n' \to \bar{n}$ and $n \to \bar{n}' \to \bar{n}$, with an amplitude comprising $\beta_{n\bar{n}'}\alpha_{nn'}$ and associated interference terms. The earlier body of searches [37, 109–111] for free $n \to \bar{n}$ would be insensitive to this scenario.

A schematic layout of the search for $n \to \bar{n}$ through regeneration is shown in figure 25. Construction of the $\bar{n}$ annihilation detector at the end of second vacuum volume will be required

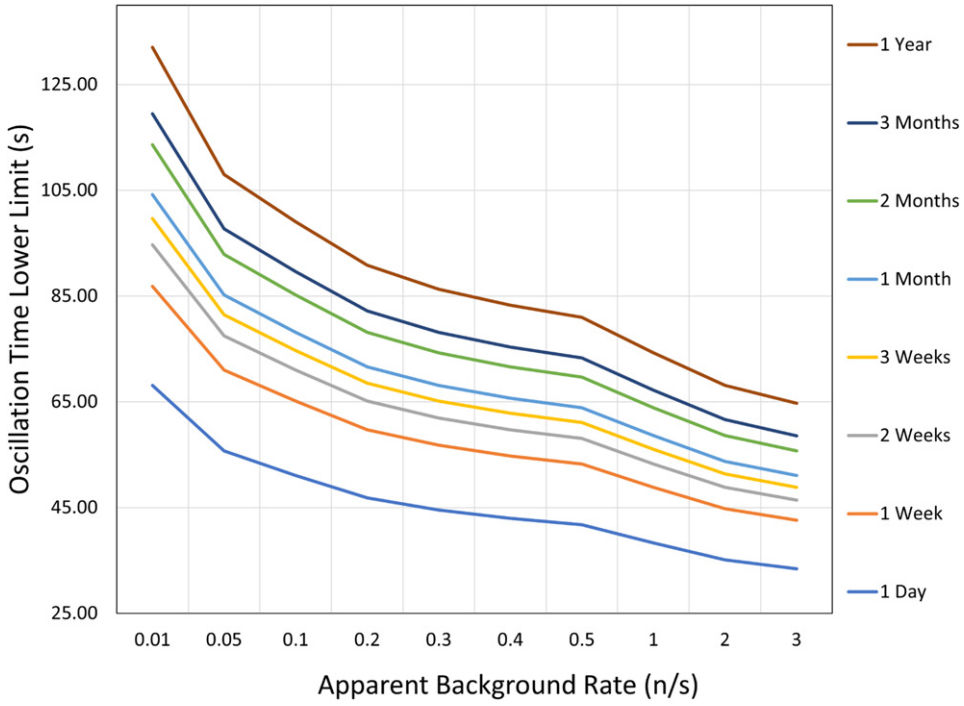

Figure 23. Sensitivity at 95% CL on the oscillation time as a function of the apparent background count for regeneration searches, $\tau_{n\to n'\to n}$ and $\tau_{n\to \bar{n}'\to n}$, in a low magnetic field configuration after 50 m of flight shown for a 0.5 m radius detector for the nominal 1 MW HIBEAM/ANNI flux.

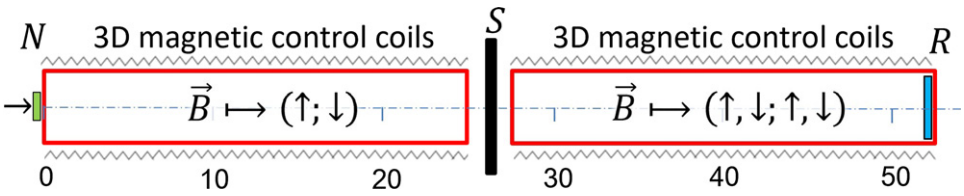

Figure 24. A simplified schematic of the $n \to n' \to n$ and $n \to \bar{n}' \to n$ regeneration searches. Two aluminum vacuum tubes with lengths 25 m are shown. The symbol N represents a low efficiency beam monitor, R shows a ^{3}He high-efficiency low-background counter and S is a beam absorber. An axial magnetic field is applied in different directions (shown by up and down arrows within parentheses) in the two vacuum tubes, and the configurations can be alternated to choose between hypothetically identical (opposite) magnetic moments of n and n' ($\bar{n}'$).

for this experiment. A search for $n \to \bar{n}$ through regeneration is complementary to the classic $n \to \bar{n}$ search assuming no sterile neutron mixing. Discussion of the details of the annihilation detector is therefore deferred to section 8.2, where it is described in the context of the classic $n \to \bar{n}$ search.

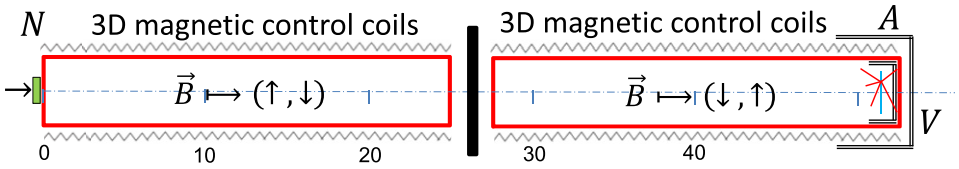

Figure 25. An $n \to \{n', \bar{n}'\} \to \bar{n}$ regeneration search schematic using two aluminum vacuum tubes with diameter 1 m. The symbol N represents a low efficiency beam monitor, A shows an annihilation tracking detector enclosing a carbon foil target to capture the annihilation $\bar{n}$C event, all of which is surrounded by V, a cosmic veto system. An axial magnetic field is applied in different directions in the two tubes.

7.5. Complementarity of searches for sterile neutrons generated via mass mixing

The program of searches has the potential to both make a fundamental discovery of a dark sector and to quantify the processes underpinning the observations. For example, if the search discussed in section 7.1 could detect a signal in the disappearance mode, this would imply a disappearance for all possible final states of oscillating neutrons. Since the magnetic moment of a neutron is oppositely aligned to that of an antineutron due to the CPT theorem (and as for sterile neutron and antineutrons), it will be advantageous to use non-polarized beams. Here, the compensation $\mathbf{B} \approx \mathbf{B}'$ would imply transformations to $\bar{n}, n', \bar{n}'$ for different initial polarization states of neutrons. In regeneration searches, all four magnetic field combinations in two flight volumes would be possible, with $\pm\mathbf{B_1}$ versus $\pm\mathbf{B_2}$ used to detect all possible channels of $n \to$ regeneration and $n \to \bar{n}$ due to mass mixing amplitudes $\alpha_{nn'}$ and $\beta_{n\bar{n}'}$.

7.6. Search for regeneration through a neutron transition magnetic moment (gradients method)

As discussed in section 3.3 and shown in equation (15), the probability of the process $n \leftrightarrow n'$ due to a TMM with magnitude κ for sufficiently large magnetic fields is approximately constant, $P_{n'} = \kappa^2$. Due to the independence of $P_{n'}$ of the magnitude of magnetic fields, the oscillating (n, n') system can travel through strong magnetic fields while retaining the same probability of transformation. In a classical sense, the gradients of the magnetic field potential $\mu \cdot \mathbf{B}(\boldsymbol{r})$ cause a force acting only upon the neutron part of the (n, n') system, and not on the sterile neutron part. Thus, the components of the (n, n') system are separated in space as with two spin components in a Stern–Gerlach experiment. When passing through a difference of magnetic potential, the difference in kinetic energies of the (n, n') components can become larger than the energy width of the wave packet of the system: this 'measures' the system by collapsing it into either a pure n or pure n' state. The required magnetic field gradient corresponding to the 'measurement' event can be found according to [88] from the following equation:

$$\frac{\Delta B}{\Delta x} > \frac{1}{\mu v (\Delta t)^2} = \frac{v}{\mu (\Delta x)^2}, \tag{25}$$

where Δx is the distance traveled in the magnetic field for time Δt, μ is neutron magnetic moment and v is the neutron velocity.

The presence of strong magnetic field gradients destroys the 'entanglement' of the oscillating (n, n') system. A surprising consequence is that as the system continues through the gradient and has its initial state repeatedly reset, this creates additional opportunities for the transformations $n \to n'$ or $n' \to n$, effectively increasing the transformation rate. In reference [88] this

mechanism was suggested as an explanation for the neutron lifetime anomaly [89]. The disappearance of neutrons due to the magnetic gradients present in UCN trap experiments could explain the $\sim 1\%$ lower value of the measured n lifetime in bottle experiments than is seen in measurements using the beam method. This explanation of the n lifetime anomaly together with existing limits from the direct experimental $n \to n'$ searches implies [88] that κ is in the range of $\sim 10^{-4}$–10^{-5}.

To test this hypothesis, solenoidal coils with alternating currents in each coil can be implemented around the two vacuum tubes to create a magnetic field along the beam axis with a 'zig-zag' shape, providing an almost constant gradient along the tube length. These coils can be applied in a regeneration experiment scheme as shown in figure 24 to search for the nTMM-induced $n \to n' \to n$ regeneration effect with $\kappa < 10^{-5}$. Another opportunity still under development is the use of a cylindrical Halbach array.

7.7. Search for regeneration through a neutron TMM (compensation method)

As described in [88] and section 3.3, an enhanced $n \to n'$ transformation rate can be produced in a gas atmosphere due to the nTMM. A constant magnetic field $\mathbf{B}$ will be applied in the flight volume to give rise to a negative magnetic potential which will compensate the positive Fermi potential of the gas. The gas density should be sufficiently low to avoid incoherent scattering or absorption of the neutrons, resulting in a pure oscillation with probability $P_{nn'} = (\epsilon_{nn'} + \kappa\mu B)^2 t^2$. The magnetic field is then scanned in order to search for a resonance condition resulting in a regeneration signal. The magnitude of the laboratory magnetic field at which the resonance might occur depends on the magnitude of the neglected hypothetical sterile magnetic field. The magnitude of $\mathbf{B}'$ can be determined by setting the laboratory magnetic field to zero and instead scanning the pressure in the flight tube. In this scenario, the probability is described by the corresponding equation:

$$P_{nn'} = (\epsilon_{nn'} \pm \kappa\mu B'')^2 t^2, \tag{26}$$

where $\pm$ is due to the different possible parities of the sterile magnetic field. Thus, the magnitude of $\mathbf{B}'$ can be also independently determined.

7.8. Neutron detection for sterile neutron searches

All forms of the sterile neutron searches rely on measurement of the visible state of the neutrons. Detection of cold and thermal neutrons requires major technical competence for the scattering experiments of the ESS, though a standard solution for neutron detection may utilize gas detectors based on ^{3}He in a single-wire proportional chamber. The detectors can be operated at low gain since the $n + {}^3\mathrm{He} \to t + p$ reaction produces a very large ionization signal. While this is the baseline technology assumed for HIBEAM, it is also possible that modern readout solutions from high energy physics can augment the performance of such a neutron detection scheme further. As an example, the most challenging readout scenario is considered here, in which each neutron in the flux would be individually detected. Assuming a neutron flux of 10^{11} n s^{-1} evenly spread out over a circular surface of diameter 2 m, and assuming each detector element to be about 1 square cm in transverse area, one would have 30 000 readout channels with a singles counting rate in each channel of about 3 MHz. This rate is indeed not trivial to deal with but it can be accommodated by the ATLAS TRT detector, where each detector element is a single-wire proportional chamber (operated at high avalanche gain) read out on the wire. Typical singles counting rates in the ATLAS TRT are in the range of 6–20 MHz, so 3 MHz seems quite feasible in comparison. The ATLAS TRT electronics will be taken out

from the ATLAS setup in 2024, presenting a timely opportunity for HIBEAM, and are therefore an interesting possibility to investigate for use in HIBEAM. The energy of the reaction products do not provide any useful information about the originating neutron, therefore only the number of neutrons detected would be recorded in the data stream. The use of coincidence criteria with neighboring detector cells will also be investigated, to avoid double counting when nuclear fragments leak into neighboring cells.

If the individual counting of neutrons is not necessary, an integration of the released charge in the detector material gives a measurement proportional to the number of incoming neutrons. After proper calibration, such current integration is less sensitive to the actual rate of neutrons. It should also be mentioned that, in view of the shortage of ^{3}He, much R & D is done for scattering experiments on other methods for cold neutron detection. Synergies with readout systems developed for high energy experiments are expected, and neutron detection in HIBEAM is a good example of an application with a specific scientific use as motivation for exploring such synergies.

8. Search for $n \to \bar{n}$ at HIBEAM

In addition to the suite of sterile neutron searches described in section 7, a major aim of HIBEAM is to act as a pilot experimental program during the early, developmental stages of the ESS, with the aim of performing a new search for $n \to \bar{n}$ transitions, at first without exploiting the planned full beam power of the facility. While this search will likely not surpass the sensitivity in reference [37], HIBEAM will be used to develop the design and prototyping of technologies necessary for the second-stage NNBAR program, which is dedicated to world-leading, complementary, high-precision searches for $n \to \bar{n}$ at the LBP. As described in section 7.4, the HIBEAM experiment will also perform searches for $n \to \bar{n}$ via regeneration from a mirror sector for which the target and annihilation detector described in this section would also be used.

This section describes the apparatus needed to perform an experimental search: magnetic shielding, the vacuum vessel, the target and the annihilation detector. Here, the detector requirements and possible technology choices are outlined. The sensitivity of the HIBEAM experiment for an HIBEAM search for $n \to \bar{n}$ is then estimated. Since HIBEAM is a pilot experiment ahead of the NNBAR stage, it would be expected that the experience of designing and operating HIBEAM would inform the final design of the NNBAR annihilation detector.

8.1. Magnetic shielding

As explained in section 3.1, the *n*s must be transported in a magnetically shielded vacuum. For quasi-free *n*s, this corresponds to a vacuum of 10^{-5} mbar and a magnetic field of less than around 10 nT along the *n* flight path [108].

The target vacuum can be achieved with a vacuum chamber comprising highly non-magnetic materials, e.g. Al, with turbo molecular pumps mounted outside of the magnetically shielded area. Magnetic fields of less than 10 nT have been achieved over large volumes (see, for example, reference [193]). For the planned experiment, a shielding concept will be used based on an aluminum vacuum chamber, a two-layer passive shield made from magnetizable alloy for transverse shielding, and end sections made from passive and active components for longitudinal shielding, as shown in figure 26.

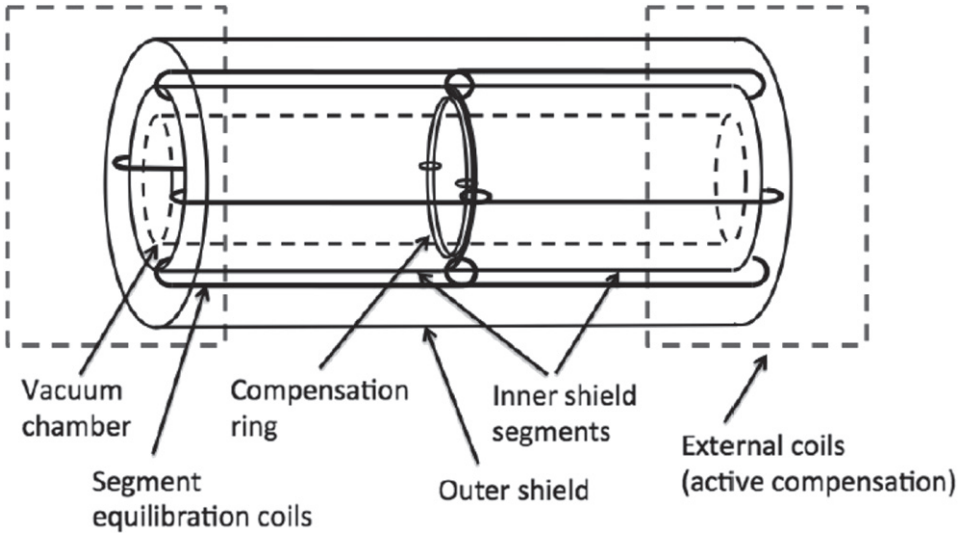

Figure 26. Schematic overview of the planned magnetic shielding. Reproduced with permission from [38].

8.2. Detector components for $n \to \bar{n}$ searches

A key experimental task of any $n \to \bar{n}$ search is to isolate and detect the annihilation of $\bar{n}$s from a beam of free ns. The transformation has an extremely low probability, and although an ESS experiment could have by far the longest experimental observation time of a free n beam, it may be probable that any experiment would measure only $\mathcal{O}(1)$ candidates.

The overarching goal for the detector system is to provide the highest possible sensitivity for detecting an $\bar{n}$ annihilation. These ambitions go beyond a statistical significance analysis, allowing for a claim of discovery from even only a few observed annihilation events; in the case of non-observation, a robust upper limit can be imposed, and multiple compelling theories of baryogenesis eliminated or severely constrained.

As much as possible, the detector system must provide a reliable and complete reconstruction of each annihilation event. Statistical correction of experimental shortcomings cannot be performed on the individual event level; thus, the design goal must be to record as many observable parameters as possible, taking in all available information about the subsequent annihilation products and, if possible, compensate directly for detector effects that are statistical in nature via over-sampling. From this, one understands immediately that special attention must also be paid to $\sim 4\pi$ detector coverage and similarly must avoid permanently and temporarily dead detection areas, due either to support structures or failing detector components, respectively. Serviceability, too, must then be a key design feature.

An important detector constraint is that a magnetic field cannot be used. Thus, momentum cannot be directly measured, only the kinetic energy deposited in the detector and the direction of the particles. A sensitive $n \to \bar{n}$ experiment should therefore:

(a) identify all charged and neutral pions, properly reconstructing their energy and direction; and
(b) reconstruct the energy and direction of most higher energy, charged nuclear fragments (mostly protons; fast ns will likely escape undetected).

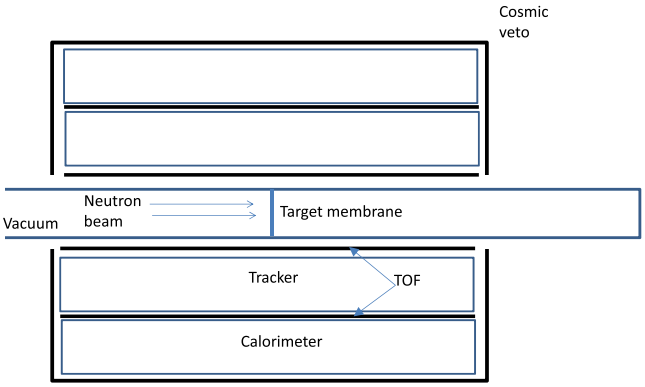

Figure 27. Schematic overview of the NNBAR detector.

The positive identification of an annihilation event would ideally comprise the identity of all pions, a total invariant mass which amounts to two nucleons ($\sim$1.9 GeV) and a reconstructed common point of origin in space and time of all emitted particles including nuclear fragments from the plane of the annihilation foil. The directionality of an event should be verified by checking that particles move outwards, acting as an important discriminant against backgrounds from CRs and atmospheric neutrinos. A generic detector must thus include tracking, energy loss, calorimetry, timing and CR veto systems, as illustrated in figure 27.

8.3. Overall geometry

The optimization of the diameter of the annihilation foil is a balance between a large diameter that maximizes the visible n flux and overall manufacturing cost, which grows dramatically with diameter. The baseline design assumes a 200 cm diameter for NNBAR and substantially lower for HIBEAM. The discussion below is guided by NNBAR while HIBEAM features are presented in section 6. During the long time of flight, the n beam will be affected by gravitation such that the flux incident upon the annihilation foil will not be regular and uniform but rather elongated vertically and containing a vertical gradient in observation time such that the slowest ns in the velocity spectrum will pass through the bottom of the foil. Since the oscillation probability (and so too the annihilation probability) grows as t^2, the largest number of annihilations will hypothetically take place at the bottom of the foil.

The geometry of the detection system will also be optimized balancing practical considerations for event reconstruction. A consequence of the broad spread of annihilations in the foil disk is that there is no strong argument for having a cylindrical detector layout. A rectangular layout is likely to be cheaper and will serve the purpose equally well, if not even better than a circular cross-section setup. On the one hand, a large area for annihilation presents a difficulty since particle detection normally assumes some average angle of incidence and a central point of emission. On the other hand, a common vertex for a number of secondaries in a large area becomes a strong constraint for an annihilation event: they contain at least two tracks in the majority of cases.

The momentum for each particle can be reconstructed if particles are identified and their direction and kinetic energies measured. If the missing momentum (higher than the Fermi momentum) points into any uninstrumented areas of the detector, one can still have a good understanding of the event, though the topology would not be as well characterized as in the case of all secondaries being observed. While full efficiency and 4π coverage for tracking and

reconstruction of annihilation products is impossible due to the n beam path, very high coverage should be achievable. A $\sim$10 m long detector with a 1 m inner radius with full coverage in azimuth would result in a geometrical acceptance of 90%, such that about half of all annihilation events will be fully reconstructed. Even with excellent geometric efficiency, loss of information about the total energy is unavoidable. The energy carried away by nuclear fragments may in most cases go unrecorded, though this should be a small fraction of the kinetic energy imparted to other heavy charged fragments like protons. On the other hand, up to 10% of the annihilation energy is lost to fast neutrons emitted from the nucleus. For momentum balance, the loss of nuclear fragments can be more significant due to their higher mass.

8.4. The annihilation foil and the vacuum vessel

8.4.1. The ^{12}C *annihilation foil.* The annihilation cross-section is very large (kilobarns compared to millibarns) for cold n capture in, e.g. carbon. A very thin carbon foil is thus sufficient to provide high probability for the $\bar{n}$ to annihilate. However, the very large cold n flux will produce gamma-emitting nuclear reactions which will be a source of background that contributes to the singles counting rate in detector channels, though it will not be a severe background to the annihilation signal itself. Although the gamma energies are low at the MeV scale, gamma production occurs at a large rate. The pileup of many gammas is therefore a potential problem to consider in the detector design, in particular the granularity.

A claim of discovery of $n \to \bar{n}$ should be supported by non-observation under conditions where no $\bar{n}$ should occur. One strategy is to switch off the magnetic shielding in the beamline, effectively prohibiting oscillation. However, this approach requires excessive additional running time to verify that the signal vanishes. An attractive alternative is to install two identical foils, separated by a distance of less than roughly a meter [110]. True $\bar{n}$ annihilation would then occur only in the first foil while false annihilation signals should occur with nearly equal abundance in the second foil, as the neutron beam is not significantly attenuated in the foil. A downside of this approach is that the background is also doubled from nuclear physics processes in the foils, requiring an increase in the background rejection capability of the setup, as well as tracking of particles in three dimensions, which is generally advantageous.

8.4.2. The vacuum vessel. The cylindrical vacuum chamber is envisioned as 2 m in diameter with 2 cm thick aluminum walls, and must achieve a vacuum pressure less than 10^{-5} mbar. The final engineering design and material choice will be informed by simulations of particle transport and background calculations. Some material effects have advantages to the experimental approach, but other effects may motivate locating the tracking detectors inside the vacuum vessel.

Advantages of thick vacuum vessel walls:

- stops electrons from n beta decay in flight;
- shields to some extent nuclear physics gamma background; and
- pair production of γs from pi^0 decay well measured by tracking and calorimetry.

Drawbacks of thick vacuum vessel walls:

- energy loss in the material makes higher threshold for detection outside the wall; and
- multiple scattering leads to worse resolution when pointing back to the annihilation vertex

With good tracking in the vacuum one could even consider to benefit better from the material in the vessel walls by using a high-Z material instead of aluminum.

8.4.3. Background considerations for higher sensitivity searches. From the ILL experiment one knows that the annihilation signal was background-free at the sensitivity of this experiment. The NNBAR experiment aims at a factor of around 1000× higher sensitivity. In the ILL experiment, CRs produced the dominant contributions to background, with the total number of these events naively scaling with the exposure time and the detector volume. These backgrounds will be present at the ESS as well, and will ultimately place more stringent demands on the efficiency for background rejection than the experiment at the ILL. Because the planned sensitivity increase at the ESS relies on an increase of several orders of magnitude in the cold neutron beam, the probability for false annihilation signals due to cold neutron beam-induced background will increase accordingly as well.

A major new difficulty compared to the ILL is the presence of high-energy background induced by the proton beam at the ESS. The contribution from this high-energy background to the annihilation signal is very hard to estimate. However, the fact that it should occur only in beam-related, rather than narrow-time windows, makes it possible to inhibit events when this background reaches the detector. The large spread of n velocities around 800 m s^{-1} means that the arrival of cold ns to the detector area at 200 m distance from the moderator will be quite uncorrelated with the cycles of the ESS linac. Based on the experience at the ILL, background to the annihilation signal is expected to be very low, but since the aim is for substantially higher sensitivity, the background discrimination should be improved as much as one can to allow discovery with the minimum number of events. Thus having the best possible resolution in total energy and vertex definition shall be the design goal. A very strong constraint is to reconstruct the vertex in three dimensions, not only two dimensions as in previous experiments. For charged particles, 3D tracking is fairly straightforward to introduce. For neutral pions, pointing back to a vertex is an interesting development task for the calorimetry.

8.5. Tracking and energy loss measurements

8.5.1. Tracking outside the vacuum. Around 99% of the annihilation events will have two or more charged pions, many of which will be visible above any detector thresholds (consider figure 4). The full reconstruction is based on these tracks, which must be reliably extrapolated through space, inwards to the annihilation vertex and outwards to the calorimetry. The tracking of these charged particles shall thus be of very high reliability. A time projection chamber (TPC) is ideal for the purpose due to the following:

- 3D tracking.
- Similar position response in all dimensions.
- Independent of track direction.
- Each ionization event recorded in all space points.
- One space point per cm gas thickness—continuous track image.
- Tracks reconstructed with very few combinatorial mistakes.
- Excellent for $\frac{dE}{dx}$ reconstruction with an eliminated Landau tail.
- Excellent granularity by the time dimension.

A TPC tracking detector can record the most information of each track in the most reliable way. By using both the space and time dimension it has a very high granularity. The TPC effectively divides up the sensitive volume in independent cells of about 1 cm^3 volume each. The drawbacks are that it has poor time resolution and requires a trigger, and is thus limited to a few kHz trigger rate.

Particle identification is important since a large fraction (typically 30%) of the annihilation energy is bound in the rest masses of the pions. Identifying the pions would constrain the

requirement on the energy balance considerably. Neutral pion identification is discussed in the calorimeter section. Measurement of $\frac{dE}{dx}$ together with a kinetic energy of charged particles can provide particle identification. At the high end of the proton spectrum, 400 MeV, a proton has velocity $0.7c$. A pion with that velocity (i.e. same energy loss) has 60 MeV kinetic energy due to the large mass difference. Setting this as a limit will cut away all protons and only lead to a loss of pions below 60 MeV, a small fraction of the pions. If energy loss is measured outside the vacuum chamber wall the difference between pions and protons will be even larger.

Since many $\frac{dE}{dx}$ measurements are performed on each track, one can eliminate the exceptional $\frac{dE}{dx}$ samples due to delta electrons. Since track direction and $\frac{dE}{dx}$ is obtained from the same information, combinatorial mistakes when combining track and energy loss information become negligible. For a robust $\frac{dE}{dx}$ measurement, the track length should be reasonably long (>50 cm). Since the track in the TPC reliably points in 3D, inwards and outwards, information about the track from different detectors are assembled with minimum risk of combinatorial mistakes. This is essential since statistical correction for combinatorial mistakes cannot be performed on individual events.

8.5.2. Tracking inside the vacuum chamber. The thick wall of the vacuum vessel will cause multiple scattering such that the track direction measured outside may lose some pointing resolution. Since the charged pions have fairly low mass, and since low kinetic energies are of interest, this is a considerable effect and the vertex resolution is an important discriminating parameter for claiming discovery. Including track coordinates on the vacuum side of the wall resolves this situation. Two space points on each track should be sufficient since the pointing from outside is good enough for the track definition.

The detector inside the vacuum will face heavy background from both n beta decaying in flight and gammas from n capture reactions. High granularity is thus necessary. Two Si strip stations with stereo angle between strips to allow for a space point from each station would serve this purpose. Arranged as a cylinder with 1 m radius and 10 m length, this would be a very costly detector and one may have to consider cheaper options with gas detectors or scintillating fibers. Possibly, one could compromise on the z-coordinate for the inner detectors if multiple scattering does not prohibit safe determination of the foil responsible for the vertex. In that case, more options for inner detectors may be considered, as long as the issue of high singles rate due to background can be avoided, which calls for a high granularity. An energy loss measurement in the vacuum also presents an advantage. With Si detectors this could be realized but is a matter of cost, while this appears to be more difficult to accomplish with other detector types. The benefit of energy loss measurement on the inside of the vacuum envelope has to be carefully evaluated.

Cases where no charged pion goes through the wall cannot be handled. At least one charged particle must give a track in the tracking outside to enable a search for stopping charged particles from potential annihilation, hypothesizing an emission point at the intercept of the extrapolated track and the annihilation foil. Rather than pions it will be more likely that charged nuclear fragments will stop in the chamber wall. For stopping particles, a maximum energy corresponding to the range in the wall material can be set.

8.6. Calorimetry

The energy measurement by the calorimeters will be a crucial part of the evidence that an annihilation event has been observed in two ways. It will identify the neutral pions that occur in 90% of the annihilations and ensure that the sum of absorbed energy (kinetic and tied up in pion rest masses) shall sum to two nucleon masses. In addition, the calorimetry shall provide

the kinetic energy of the charged pions and charged nuclear fragments. Energy measurements at these energies are notoriously difficult. Several processes are involved.

8.6.1. Charged hadronic particles. As long as the incoming particle is stopped by ionization energy loss only, its kinetic energy can be measured with good resolution. However, already at pion energies around 100 MeV this means traversing a great deal of material and the probability for nuclear reactions becomes sizable. The energy can still be correctly measured as long as secondaries are charged and all energy is absorbed in a sensitive detector material. Energy carried by fast neutrons will not be absorbed and remain unmeasured. For this reason low-Z materials are preferred. For the actual annihilation products, protons will be mostly stopped by ionization energy loss while the bulk part of the charged pions cause nuclear interactions resulting in an energy deficit. If the calorimeter only samples a fraction of the energy of the charged particles as in a sampling calorimeter, the actual energy signal in the case of a nuclear reaction can instead become larger due to the larger energy loss by slow nuclear fragments. On the other hand, some nuclear fragments will stop in insensitive absorber materials. Other effects that obscure the energy measurement of charged pions is an additional 4 MeV energy from weak decay of positive pions where an undetected neutrino carries away most of the energy of the pion mass. This mass could always be inferred from the charged pion identification so it is a small effect. A larger effect is that negative pions stopping in the material will be captured by nuclei. Energy corresponding to the pion mass shall be carried away but some will be by fast neutrons and be undetected. This gives an uncertainty in the energy by one pion mass.

All these unavoidable effects can normally be corrected for by averages based on simulations. Here, where we want the energy to be measured as accurately as possible for each individual particle, one cannot correct and the calorimeter design must be optimized differently. In some sense these fundamental unavoidable problems are arguments against expensive materials with very good energy resolution. Possibly, measuring $\frac{\mathrm{d}E}{\mathrm{d}x}$ and the range of particles can give can the most reliable information.

8.6.2. Photons from neutral pion decay. The two photons from neutral pion decay have at least 67.5 MeV energy. This is far above the energy of any natural sources of particles except cosmic origin. Ninety percent of all annihilations have at least one neutral pion. A single photon energy threshold should thus be a simple and reliable trigger of annihilation events. For electromagnetic calorimetry the energies are quite low leading to poor shower statistics. As long as the detector medium is sensitive over the whole volume and large enough to absorb all energy, the shower fluctuations do not influence the energy resolution. In a sampling calorimeter (mixed absorber and sensitive materials) shower fluctuations lead to lower energy resolution. For both calorimeter types, the position resolution of the incoming photon is worsened by the shower fluctuations.

The calorimetry of photons serves three purposes: triggering on annihilation events, identifying neutral pions and determination of the pion kinetic energy. A pointing ability toward the annihilation vertex would verify the neutral pion as having the same origin as the charged particles and add to the constraints on the annihilation event. Since 98% of annihilation events have at least two charged pions, a vertex based on these should be identified for all events one would analyze. With this vertex known (which is also the decay point of the neutral pion) and the impact positions on the calorimeter measured, one can reconstruct the invariant mass of any pair of photons from the opening angle between photons and the measured photon energies. The invariant mass resolution is key to a firm, particle-by-particle statement about the potential neutral pion since:

- a narrow cut on invariant mass minimizes combinatorial background, which is key to a statement that these photons come from a neutral pion; and
- the more accurately the invariant mass is measured, the better the assumption of the photon origin at the vertex of the charged particles is confirmed.

Crystals of high Z, sensitive over the whole volume, are superior in terms of energy resolution since the limited shower statistics is irrelevant for the resolution. The position resolution will be rather poor both for crystals and sampling calorimetry since it is deteriorated by shower fluctuations. The way to improve position resolution is to choose materials with a small Moliere radius. Moving the calorimeter to a larger radial distance from the cold neutron beam axis improves the opening angle resolution as well.

Uniformly sensitive crystals can be either based on scintillation light (several high-Z materials exist) or Cherenkov light (lead glass being mostly used). Both types share the ability to measure the total energy as deposited by electrons and positrons, and from a fundamental point of view they could have equally good resolution for photons. In the readout stage, one can expect to have more light from a scintillator and thus somewhat better energy resolution. However, scintillators give a signal corresponding to all deposited energy while lead glass is basically blind to nuclear fragments due to the Cherenkov threshold. Charged pions of at least 30 MeV produce Cherenkov light. The energy calibration of lead glass for charged pions in the actual energy range desired for NNBAR is not trivial. On the other hand, the different nuclear effects for stopping pions will not give arbitrary additions to the measured energy.

While fully sensitive crystals are highly desirable, they are also the most expensive solution. One will not benefit fully from the expensive materials because of the large spread in angle of incidence of the photons. Placing the calorimeter at larger radial distance gives a more perpendicular angle of incidence but at a dramatically increased cost. Crystals will also have substantial sensitivity to high intensity energy gamma background with nuclear origin.

A sampling calorimeter may be a more cost-effective option. It can be made so that the response does not depend on angle of incidence and it is less sensitive to gamma backgrounds since the conversions happen mostly in the high-Z absorber material. If photoelectrons escape into a readout scintillator they will give a signal only in one of the readout planes, i.e. much lower signal than if created by showers of many electrons propagating through many layers of scintillator. A useful feature of the measurement situation is that the rate of ionizing particles going through more than one sensitive layer of the sampling calorimeter is very low while the rate of ionizing events in single layers is large, calling for high granularity in the readout. High granularity can however just as well be achieved by segmentation in depth instead of laterally as one would be normally, which can be useful for the charged particle energy/range measurement. The readout of individual range segments can then be performed over a large transverse area as long as the readout is position-sensitive. Then the tower structure of calorimeter cells can be avoided while still obtaining the same calorimetric response, irrespective of angle of incidence. By a 2D coordinate for each range segment one has a pointing vector for the photon. Longer air gaps in the calorimeter stack can even be included to improve the pointing resolution. The requirements on the calorimetry are quite different from the state-of-the-art calorimetry in high-energy physics. This calls for an interesting R & D program to find the best solution for NNBAR.

Motivated by the arguments discussed in this section, a Geant study of the response of a calorimeter module to charged hadrons and photons has been performed ahead of a detailed study of a physical prototype at an *in situ* ESS neutron test beam in 2023 and test beams at other facilities. The module is based on lead glass and scintillators and exploits the Cherenkov signature for electromagnetic energy, caused by the interaction of photons, charged hadrons

(mainly via $\frac{dE}{dx}$) and hadronic energy. A charged particle range telescope comprising ten layers of plastic scintillator lies in front of the lead glass. More details are given in appendix A.1.

8.7. Cosmic veto, timing and triggering

8.7.1. Cosmic veto. The sum of two n masses represents a high energy which cannot be produced by any background source in nature other than CRs. Therefore an active veto detector against charged CR particles must surround the detector. It should consist of two layers of active material such as plastic scintillators. Two close-by detector layers in coincidence reject induced background in order to avoid false vetoes, which, if too frequent, reduce efficiency by vetoing good events. The detector material should be several cm thick to allow discrimination by a simple threshold of several n induced backgrounds such as Compton scattered gammas, with signal independent of detector thickness, from charged minimum ionizing particles, with signal increasing linearly with detector thickness. The cosmic veto is expected to be a part of the hardware trigger logic and vetoed events will not be stored. However, it may prove possible to postpone the rejection from the cosmic veto to the offline analysis. Thus the cosmic veto should be designed with sufficient timing resolution to determine the direction, inwards or outwards, of the particles associated with the signal.

Charged CRs producing high-energy deposits and tracks in the NNBAR detector are rather straightforward to discriminate. Much more problematic is if the deposit is induced by energetic neutral particles (γs or ns). A geometrically long sampling calorimeter divided in depth opens up the possibility to measure the direction of the showers by timing measurements within the calorimeter. In addition, a Cherenkov-based calorimeter is sensitive to the direction of the shower and could be made essentially blind to showers directed inwards. Finally, dE/dx measurements may be helpful for an additional layer of veto for fast neutrons.

8.7.2. Timing. For charged particles in the tracking system it is desirable to verify that particles of interest travel outwards. Over a 1 m distance there will be a 6 ns timing difference between relativistic particles for the two cases. Such timing resolution is not very demanding and detectors for this purpose shall be placed at the entrance and exit of the tracking system. More demanding than time resolution is the singles counting rate, which is large in these regions of the setup. Plastic scintillators are adequate for the timing resolution and background signals from n-induced nuclear physics processes can be discriminated similarly as was described for the cosmic veto, with a double detector layer for each station and several cm of scintillator thickness.

Other detector solutions with good timing resolution and two-dimensional readout (to give the space point together with the chamber plane) would be resistive plate chambers (RPCs). One could achieve a high granularity by the two-dimensional readout and, since the signal is formed by the particle passing multiple gaps of avalanche gain, one could discriminate Compton gammas since they will only give signal in at most one avalanche gap. Making this a specific design goal one could probably arrive at a good solution with respect to preventing background to destroy the time measurement. RPCs could therefore also be a viable option for the cosmic veto.

8.7.3. Triggering. A trigger to catch energy deposits of more than 67.5 MeV for one of the gammas from a neutral pion decay is straightforward to implement in hardware as a signal threshold that will catch 90% of the annihilations. If taken in anticoincidence with the CR shield, the trigger should be easy to handle by modern data acquisition systems. With modern computational approaches and powerful signal processing on the detector, online data reduction can be powerful enough to take data without hardware triggering, as with the upgrade of

the ATLAS experiment at the LHC. In addition to a trigger on electromagnetic energy in the calorimeter, a track trigger can be implemented with the timing detectors (plastic scintillators or RPC) as described above. The lack of a point defined by a known collision vertex makes it necessary to allow large directional freedom in the track matching of the track trigger. Of course, straight-line tracking (no magnetic field) helps motivate three tracking trigger stations. Powerful background rejection on the signal level is mandatory.

8.8. Search for $n \to \bar{n}$

For $n \to \bar{n}$ via mass mixing, the quasi-free condition is needed, implying magnetic field-free transmission of neutrons. Any antineutrons which are produced would then annihilate with a target surrounded by a detector. The detector would reconstruct the characteristic multi-pion signal to infer the existence of $n \to \bar{n}$.

As shown in section 4.1, the FOM for a free $n \to \bar{n}$ search is given by $\langle N_n\, t_n^2 \rangle$. The FOM is proportional to the rate of converted neutrons impinging on a target to achieve a high FOM, the following criteria must be met:

(a) The n source must deliver a beam of slow, cold ns (energy <5 meV) at high intensity, maximising both t_n and N_n, respectively, for a given beamline length.
(b) The beamport must correspond to a large opening angle for n emission.
(c) A long beamline is needed to maximize t_n.
(d) A long overall running time is needed due to the rareness of the process.

Note that neutron beams with lower average energies have higher transport efficiencies when supermirror reflectors are utilized, as in the second-stage NNBAR experiment described in section 9.

8.9. Sensitivity of HIBEAM for $n \to \bar{n}$

Considering figure 25, if the central n absorber were to be removed and two vacuum tubes were be combined to one with the common magnetic compensating/shielding system, one would recover the essential elements of a $n \to \bar{n}$ experiment at the HIBEAM/ANNI beamline, although with a shorter neutron flight path. Figure 28 shows the sensitivity in ILL units per year normalized to the ESS running year, i.e.

$$\begin{aligned} \text{ILL units per year} &= \frac{\langle N_n\, t_n^2 \rangle_{\text{ESS}}}{\langle N_n\, t_n^2 \rangle_{\text{ILL}} \cdot \ (\text{Operational Factor})} \\ &= \frac{\langle N_n\, t_n^2 \rangle_{\text{ESS}}}{(1.5 \times 10^9) \cdot (1.2)} \end{aligned} \tag{27}$$

of a $n \to \bar{n}$ search as a function of the radius of the detector, assuming a 1 MW operating power. One ILL unit is defined using the FOM and the flux and running time used in reference [37] as an observable for the number of converting neutrons for a given mass mixing term. The operational factor is a correction factor for the different annual running times expected at the ESS compared to the ILL for the latter's total running period. The sensitivity estimate given by this approach conservatively assumes that the detection efficiency at HIBEAM would be the same as at the ILL experiment ($\sim$50%).

The sensitivity reaches a plateau for a detector radius of $\sim$2 m. It can be seen that an ILL-level sensitivity can be achieved after running for several ($\sim$3) years with an appropriately sized detector, but this should be considered a generous possibility, as cost considerations may lead to a smaller detector. These can be only linearly offset by a longer running period and

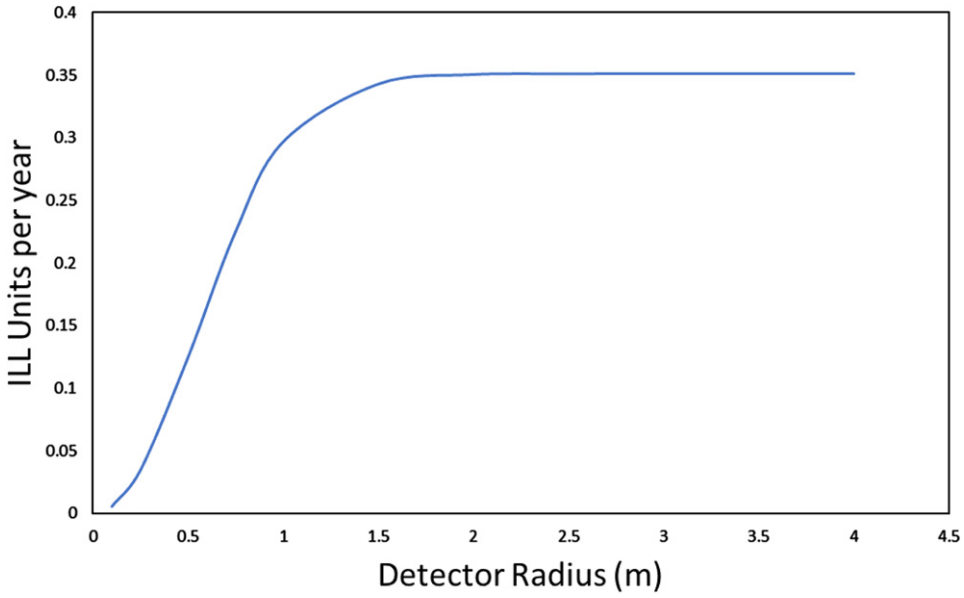

Figure 28. Sensitivity (in ILL units) of the $n \to \bar{n}$ search at HIBEAM/ANNI as a function of the radius of the annihilation target, assuming 1 MW of operating power, perfect reconstruction, and zero background.

higher operating power. $\bar{n}$ ^{12}C annihilation and outgoing product tracking efficiencies, along with their associated cosmic, atmospheric and fast-n backgrounds, have not yet been considered entirely, though state-of-the-art simulations of the underlying microscopic processes have been completed [124, 172].

Nonlinear, though fractional, increases in sensitivity can be achieved with the design and construction of focusing (pseudo-)ellipsoidal superupmirrors starting near the beamport to increase (anti)neutron flux on the ^{12}C annihilation target. Highly preliminary computations using 0.25 m minor-axes and major-axis lengths of 27–50 m for half-ellipsoidal reflector geometries assuming perfect n reflectivity have shown some $\sim$40% increase in overall sensitivity. More realistic configurations and reflectivity modeling must be completed and geometrically optimized.

9. Neutronics and the NNBAR experiment

In order to realize a modern NNBAR experiment that would provide a substantial improvement in sensitivity ($\sim$1000$\times$) than that achieved at the ILL experiment [37], a higher overall cold neutron intensity must be utilized. As stated in the 2013 ESS Technical Design Report [180], there is a requirement that the ESS provide a level of time averaged cold brilliance comparable to the current cold source at ILL. This, along with novel neutron optical design concepts, can facilitate an experiment with orders of magnitude improvement over previous experiments. Furthermore, as discussed in section 5, a lower liquid deuterium moderator can be installed. Figure 29 illustrates how parts of the shield and reflector system removed to allow a greater conical penetration and to minimize losses due to the presence of the Fe shield and Be reflector system.

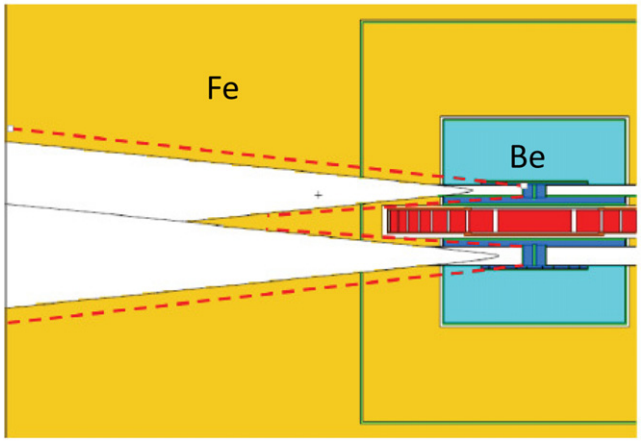

Figure 29. Nominal (white region to the left of the neutron source) and enlarged (region enclosed by dashed lines) conical penetration through the Be reflector and Fe shield.

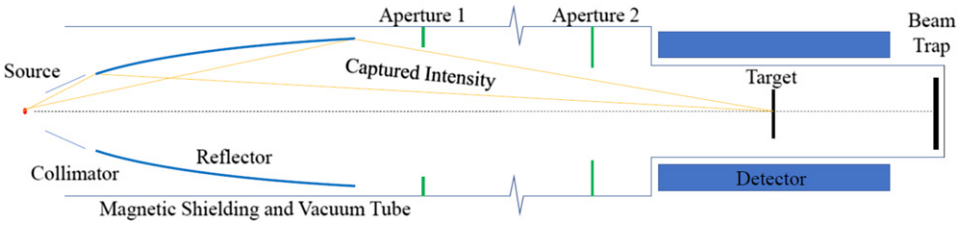

Figure 30. Baseline NNBAR experiment. Neutrons from the moderator are focused on a distant target foil surrounded by an annihilation detector.

In this section, the sensitivity of the NNBAR experiment is quantified. A baseline outline of the NNBAR experiment is given followed by a description of a Monte Carlo-based estimation [194] of the performance of a neutron reflector coupled to a large volume, lower liquid deuterium moderator [187] using simulation geometry implemented within MCNP [195]. The aim is for a zero background search, as achieved at the ILL. The background reduction strategy is described in section 10.

9.1. Baseline NNBAR experiment

A simple baseline NNBAR experiment is shown in figure 30. A longitudinal distance of 200 m separates the source and the target foil. Neutrons passing through the foil are absorbed in a beam trap.

In order for NNBAR to make the most of the impressive neutron intensity at the ESS, there must a be a 'gathering' reflector to ensure that a large neutron flux is directed and focused via a magnetically shielded region on the annihilation target. To first order, the most obvious reflector geometry is that of an ellipsoid [196], which would facilitate efficient transport of neutrons that otherwise would miss the annihilation target completely. The start and end points of the reflector on the longitudinal axis are 10 m and 50 m, respectively. The semi-minor axis of the ellipsoid is 2 m. The radius of the annihilation foil is 1 m.

An effective reflector must be fully illuminated by the source. This means that a substantial amount of the overall intensity will have trajectories that deviate significantly from the nominal beam trajectory axis. To achieve this, reflecting angles for even fairly cold neutrons ($\sim$1000 m s^{-1}) will exceed that of the limit of the best traditional reflectors. NNBAR will thus use neutron supermirror technology [197] which has been used with success for many years as a means to guide thermal and cold neutrons to many scattering instruments at both pulsed and continuous neutron sources. NNBAR will utilize the same multi-layered surface treatment on its reflector to gather and focus the wide range of neutron trajectories at the source. To do so, surfaces with surface reflectivity up to $m = 6$, i.e. a reflection capability as high as six times better than the reflectivity limit for polished nickel. Neutrons from a liquid deuterium source are collimated in the structure housing the moderator. Neutrons emerging are reflected via an ellipsoid supermirror along a magnetically shielded region toward a target foil, surrounded by an annihilation detector. A beam trap absorbs the beam. The detection efficiency of an annihilation event in the foil is 50%.

9.2. Differential reflectors

At the LBP, the liquid deuterium source would be offset from symmetry axis of the LBP which is aligned with the target. To deal with this, a segmented differential reflector was designed. This has a distorted ellpsoid-like shape, albeit one which can be optimized via the solution of coupled differential equations for neutron reflections to allow specific reflection angles at certain distances from the foci, providing maximum intensity to the target foil [194]. Segmentation also allows optimization of the m value for different panels in the supermirror complex, reducing costs and allowing for easier large scale manufacturing.

Figure 31 (top) shows a simulation of a neutron reflection and focusing toward a target at 200 m distance along the longitudinal axis (referred to as beam trajectory position) from the position of the reflector in a differential reflector. It is shown how the neutron emerges from a source which is offset from the central-axis of the ellipsoid-like reflector. Figure 31 (bottom) shows a sampling of traced rays representing neutron trajectories, also including gravity. The neutrons can be restricted to a range in the vertical direction transverse to the longitudinal axis of around 2 m.

9.3. Sensitivity of the NNBAR experiment

Figure 32 shows a sketch of a differential reflector configuration with parameters that can be optimized to maximize the sensitivity of the NNBAR experiment. Shown are the source focal point position, $\vec{x_s}$, the target focal point position, $\vec{x_f}$, the reflector start position, z_i, and the reflector end position, z_f.

An optimization of the shape parameters (keeping the others constant) was made. Figure 33 show how the sensitivity for NNBAR varies as a function of the source focal point vertical position, the source focal point horizontal position, the target foil focal point horizontal position, the reflector start position, the reflector end position and the surface reflectivity m. The sensitivity is expressed as ILL units per year, as defined in section 8.9.

As can be seen, a sensitivity of around 350 ILL units per year is obtained. The sensitivity is strongly dependent on the surface reflectivity m. Indeed, developments in the supermirror technology are one of the driving factors in allowing NNBAR a large sensitivity increase since the ILL experiment. The peak sensitivity of $\sim$350 ILL units per year is achieved for $m \sim 6, 7$ and falls to $\sim$10 ILL units per year for $m \sim 1$. A doubling of start position from 10 m to 20 m leads to an approximate halving of the sensitivity. Extending the end position from 40 m to 60 m increases the sensitivity by around 20%. The foil focal point horizontal position is less

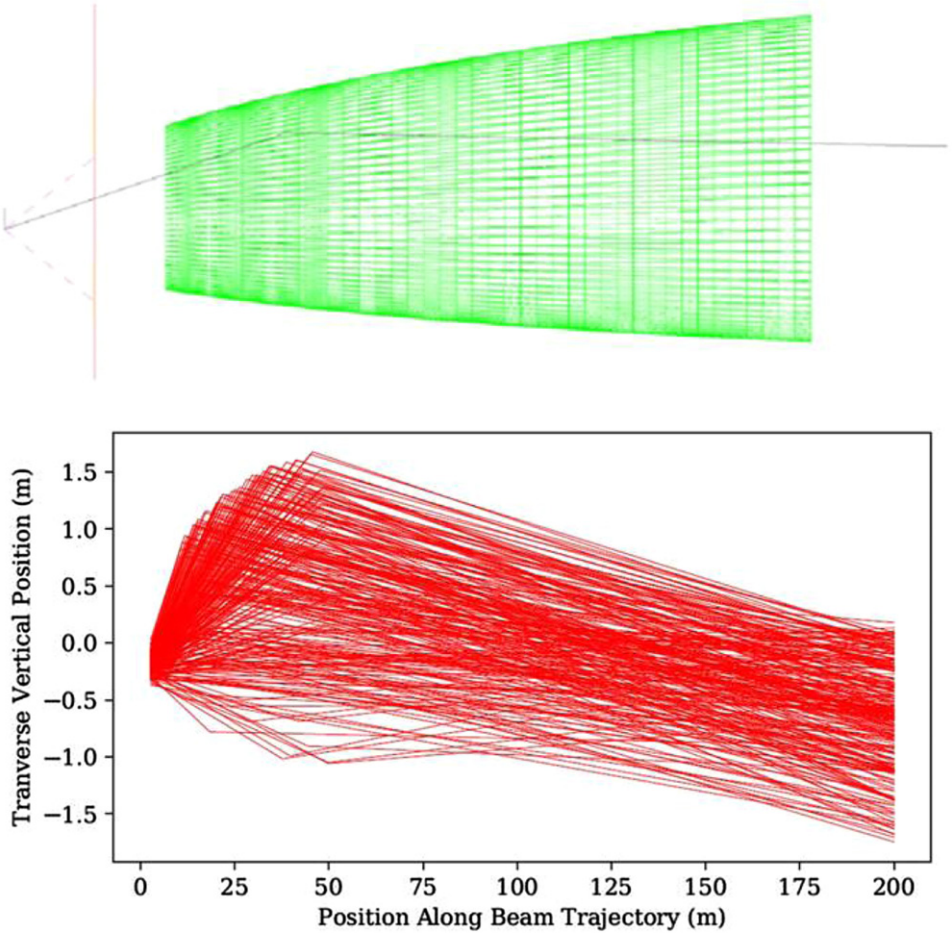

Figure 31. Top: neutron reflection and focusing from a segmented differential reflector. Bottom: sampling of traced rays showing the transverse vertical displacement of the neutrons as a function of longitudinal distance.

sensitive, changing by about 10% for shifts of up to 4 m. Optimising the source focal points (horizontal and vertical) changes the sensitivity by up to around 30% in the considered range.

9.4. Gain with respect to the ILL experiment

As was shown in section 9.3, simulations predict a sensitivity of around 350 ILL unit per year. For an experiment running for three years this provides an improvement of three orders of magnitude. The increase in sensitivity can be broadly decomposed into the gain factors given in table 4. Sensitivity increases are due to the greater source intensity, propagation length and run time. The largest gain is from the now widely available high m reflectors.

To further investigate differences between the ILL and the ESS for a search for $n \to \bar{n}$, the performance of only the moderators was studied. In this case, the calculated performance of a liquid deuterium lower moderator of ESS was compared to the ILL horizontal cold source (HCS), used for the original ILL search. For this comparison, updated brightness data was considered, indicating that the cold brightness of the ILL moderators is about three times larger

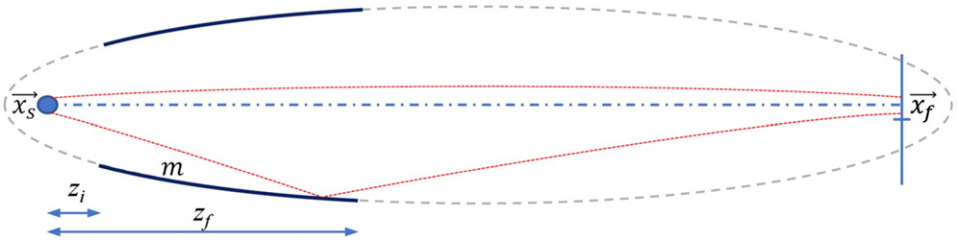

Figure 32. Parameters for a differential reflector relevant to the design and sensitivity of the NNBAR experiment.

than the official data [198]. Even with this correction, it was found that an optimized ESS lower moderator together with the upper 'butterfly' moderator would deliver a higher intensity, larger than the HCS used for the ILL search. The expected gain is due to several factors, including an optimal beam extraction (aiming at viewing the full surface of the moderator) and an optimization of the moderator specifically for the NNBAR experiment.

9.5. Discussion of sensitivity

The results shown above exploit a simulation of a liquid deuterium lower moderator. One of the goals of the HighNESS project [185, 186] will be to deliver an engineering design of such a moderator. The performance will be different to that previously simulated and a new NNBAR sensitivity will be quantitatively determined. Based on experience and results from previous moderator designs, it is possible to list and give quantitative estimates of factors influencing the performance of such a moderator. This includes several contributions, which either increase or decrease the performance of the moderator for NNBAR's ultimate capability.

The first group of contributions enhance NNBAR's sensitivity and include optimizations of the design, including moderator size, positioning with respect of the target and the use of reentrant holes, a proven technology to increase neutron intensity by a factor of 1.5× for a specific direction [199]. Furthermore, if pure orthodeuterium is assumed instead of the mixture of ortho- and paradeuterium used in reference [187], the expected spectrum should be colder than previously calculated in the simulation [187] used for the NNBAR sensitivity estimates above. Another option might be to employ a single-crystal reflector filter in front of the moderator to enhance the thermal and cold flux while reducing the epithermal and fast flux [200].

The second group comprises contributions which can potentially degrade the sensitivity of NNBAR. This can occur with the refinement of engineering details: the fact that other beamlines, other than NNBAR, might view the moderator and may consequently require the removal of some reflector material surrounding the moderator, resulting in decreased performance [183]. Also, a possible shadowing effect of the inner shielding in the monolith could reduce the effective (viewed) surface area of the moderator. Naive estimations suggest a cancellation of these competing effects.

A full quantification of the NNBAR sensitivity is part of the HighNESS program. However, it should be noted that, in principle, running times can be extended to mitigate against any loss of sensitivity. Furthermore, estimates provided in this paper are rather conservative with an assumed selection efficiency for an annihilation event of around 50%, as obtained at the ILL; indeed, detector technology and data analysis methods in experimental particle physics are substantially more advanced compared to the early 1990s and so a far higher efficiency would be expected for a modern-day experiment. Finally, only a lower liquid deuterium moderator

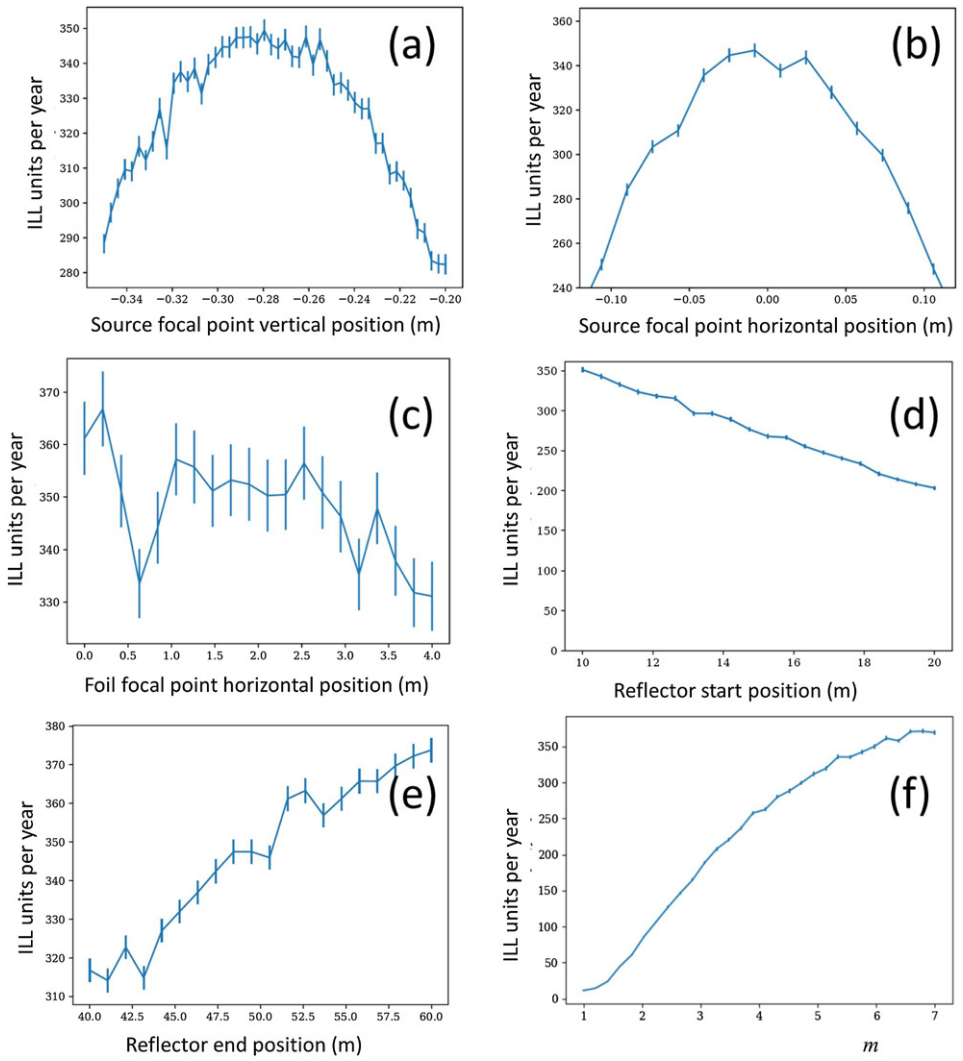

Figure 33. Sensitivity of the NNBAR experiment for one year of running in ILL units as a function of (a) the source focal point vertical position, (b) the source focal point horizontal position, (c) the target foil focal point horizontal position (d) the reflector start position (e) the reflector end position and (f) the surface reflectivity m.

was considered for the sensitivity calculations given in this section. The upper butterfly moderator would also provide an additional flux of cold neutrons. Mitigation by longer running and the conservative nature of the current estimates could thus also protect against an unexpected lowering of the planned full power of the ESS from 5 MW to 2–3 MW.

9.6. Sensitivity of NNBAR and other experiments

Limits on the free $n \to \bar{n}$ oscillation time, together with the potential sensitivities of HIBEAM (section 8) (assuming 3 years running at 1 MW) and NNBAR (assuming 3 years running at 5 MW, and a three orders of magnitude improvement in ILL units) are shown in figure 34.

Table 4. Breakdown of gain factors for NNBAR with respect to the last search for free neutron–antineutron conversions at the ILL.

Factor	Gain w.r.t. ILL
Source intensity	$\geqslant 2$
Neutron reflector	40
Length	5
Run time	3
Total gain	$\geqslant 1000$

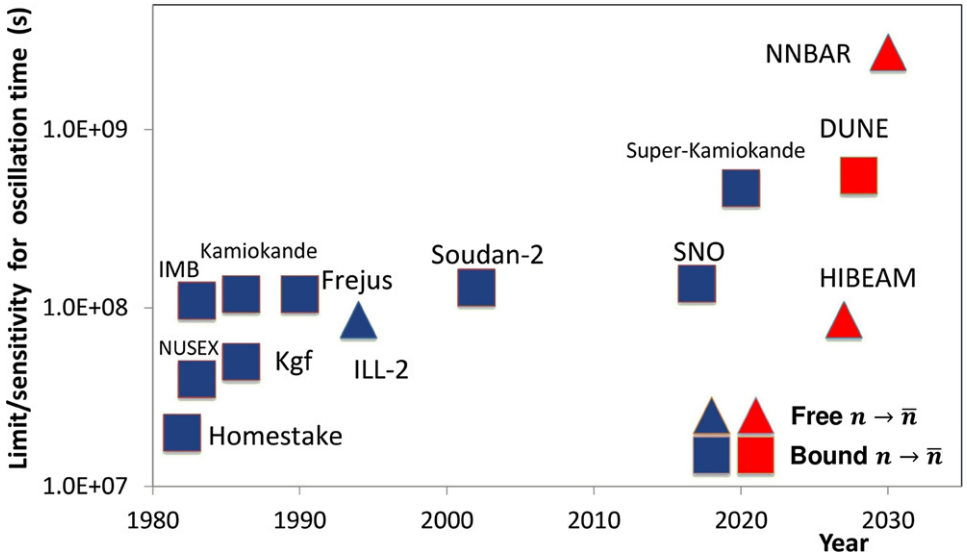

Figure 34. Lower limits on the free neutron oscillation time from past (blue) experiments on free and bound neutrons. Projected future (red) sensitivities from HIBEAM and NNBAR are shown together with the expected sensitivity for DUNE. Searches with free neutrons with made with the Pavia Triga Mark II reactor [109, 110] and from the searches made at the ILL [37, 111]. The most recent and competitive result from the ILL is shown and is denoted ILL-2 [37]. Limits from bound neutron searches are given from Homestake [115], KGF [116], NUSEX [117], IMB [118], Kamiokande [119], Frejus [120], Soudan-2 [121], SNO [122] and Super-Kamiokande [57]. For the bound neutron experiments, various model-dependent intranuclear suppression factors are used to estimate a free neutron oscillation time lower limit.

Also shown in figure 34 is a projected converted free oscillation time lower limit for bound neutron conversions within ^{40}Ar nuclei within the future DUNE experiment, where $\tau_{n\to\bar{n}} \geqslant 5.53 \times 10^8$ s [123] for an assumed exposure of 400 kt years. Note that this limit does not take account of new ^{40}Ar intranuclear suppression factor calculations completed in [124]; systematic simulation studies continue within the DUNE collaboration and further automated analysis improvements are underway [123] in hopes of eliminating atmospheric neutrino backgrounds. There is as yet no estimate for the expected $n \to \bar{n}$ sensitivity for Hyper-Kamiokande.

As discussed in section 3.1, consideration of limits or sensitivities on the free neutron oscillation time for free and bound neutron searches is, to a certain extent, an *apples and pears* comparison. There is overlap in physics potential, but neither renders the other redundant.

Indeed, both would play essential and complementary roles in both the definitive establishment of and cross reference for any future discovery.

10. Backgrounds

In this section, the background sources for HIBEAM and NNBAR are described. Common backgrounds for HIBEAM and NNBAR in the context of $n \to \bar{n}$ transformations are discussed first, followed by a description of backgrounds which are exclusive to NNBAR. Backgrounds for HIBEAM in the context of $n - n'$ oscillations, for both disappearance and regeneration modes, are discussed separately.

10.1. HIBEAM–NNBAR backgrounds

As discussed in section 3.5 the experimental signature for $n \to \bar{n}$ is striking: the annihilation of the antineutron, releasing roughly 1.9 GeV of total energy, typically in the form of pions (four to five on average).

It is instructive to consider the background mitigation strategy of the most sensitive cold neutron experiment performed to date at the ILL [175]. Using a steady reactor neutron source, this experiment confirmed an absolutely zero background while expecting a signal efficiency of $\sim$50% by using multiple track and kinematic cuts. Such a unique, state-of-the-art feature is impressive, especially given the large integrated flux of slow neutrons which passed through the annihilation target every second (10^{11} n s^{-1}). Developing a detector scheme with zero background is extremely important for the potential detection of an antineutron appearance where even a single event can represent a fundamental discovery.

Both HIBEAM and NNBAR must contend with cold neutron beam-generated and CR backgrounds. Beam-generated backgrounds comprise fast neutrons and high-energy particles from the spallation source, as well as charged and neutral CRs generated in the upper atmosphere. NNBAR will be especially likely to be affected by high-energy products from the spallation process given the large opening angle of the beamport. These all are now discussed.

10.1.1. Cold neutron beam backgrounds. Cold neutron beam backgrounds include an irreducible component in the form of MeV gammas from neutron capture in the annihilation target and beamtube, as well as fast neutrons from the source. To achieve backgroundless operation (below one stray event per year of operation), the HIBEAM and NNBAR detectors should use a similar configuration to the ILL experiment, where only 5.2% of the cold neutron beam was lost to the beam optics and in the journey to the target. At the ILL, the beam halo was absorbed by boron-loaded glass collimators and the beam dump was constructed of ^{6}Li-loaded tiles. Similar technology is being considered.

Compared to the ILL, the (NNBAR) detectors will see a significant increase of $\geqslant$100 times) cold neutron current through the annihilation target. With a neutron absorption probability $\sim 5 \times 10^{-6}$, this rate will produce $\sim 10^8$ reactions in the target film per second or 5×10^5 GeV per second of isotropically emitted low energy ($\sim$MeV) photons inside the detector. This energy deposition rate will not be too challenging for a modern trigger system, but it can provide high counting rates in the sub-detector elements and can be a potential source of background in random combination with cosmic events or (for NNBAR) with fast neutrons. Given that the ESS will have such an enormous increase in incident flux compared to the ILL and an even larger increase in the portion of the beam which does not reach the target, more stringent requirements on the beam line shielding, detector granularity, tracking resolution and trigger cuts will be required. In the ILL experiment, spurious events above threshold produced

by multiple gamma-ray hits during the 150 ns trigger timing window account for about 32% (1 Hz) of the total trigger rate of ∼4 Hz.

10.1.2. Cosmic rays. CRs were the dominant backgrounds for all previous free neutron transformation experiments. For the ILL experiment, these alone accounted for a remaining 3 Hz of trigger rate, with 2.7 Hz coming from CR muons which evaded the veto (an efficiency of ∼99.5%) and 0.3 Hz due to neutral CRs. The neutral CRs were of particular concern, as they evade the CR veto and can appear to produce events which originate from the target; these were assessed to be the leading contributors to possible backgrounds in the signal window. Given the larger annihilation target area and detector volume for HIBEAM, and especially for NNBAR, these events are expected to potentially contribute to backgrounds and a corresponding improvement in vertex reconstruction and event identification will be required.

10.1.3. High energy products from the spallation source — NNBAR only. Previously at the ILL, moderated neutrons from the reactor source were directed into a curved neutron reflecting guide, such that slow neutrons with low transverse momenta were transported along while fast neutrons and photons were filtered out. This will occur for HIBEAM by virtue of using an *S*-curved ANNI guide system (see figure 14).

For the NNBAR experiment there are also other sources of backgrounds specific to the spallation source that were not present for the ILL experiment due to the usage of the large beamport. When protons with an energy of 1–2 GeV interact with a heavy nuclear target, spallation can produce high-energy particles (such as protons, pions, muons, gammas), most essentially among them neutrons with an energy range of MeV to GeV; once moderated, these become the slower neutrons of interest (reaching the detector after ∼0.1 s). In the NNBAR layout, in order to achieve higher cold neutron currents, the detector will directly view the source through the large beamport, where all fast charged and neutral particle components will contribute to additional backgrounds. Fortunately, due to the pulsed operation of the ESS, these fast particles can be vetoed by time of flight (during a period of ∼10 μs after the beginning of the pulse) by excluding the beginning of a proton beam spill on the spallation target. It is estimated that this would lead to a <5% loss of the total cold beam intensity for a neutron–antineutron transformation search.

10.2. HIBEAM backgrounds: neutron–sterile neutron oscillations

Both disappearance and regeneration of sterile neutrons would rely on the observation of a magnetic field dependent resonant oscillation signal. These two methods have different systematic difficulties: (i) for disappearance, one must detect a small reduction in the counting rate of total incident neutrons to the order of $\sim 10^{-6}$–10^{-8} of the total flux, a challenge due to the need for precisely characterized, ultrahigh efficiency neutron monitors able to handle the large beam intensity; (ii) for regeneration, one must have a very low background count rate in the final neutron detector following total incident beam absorption, requiring an essential detector shielding effort.

From knowledge of other currently operating cold neutron sources such as the HFIR and the Spallation Neutron Source at Oak Ridge National Laboratory, it is known that the ambient background rates in ^{3}He tube-style cold neutron detectors are rather low (few n s^{-1}), even when large in overall area and closer to their respective sources than HIBEAM plans to be; this is also the case despite higher duty cycles compared to the ESS. This generalized rate usually includes no vetoes or purpose-built particle-tracking equipment around the detectors and only modest shielding and so can be still improved. Assuming an effective background rate of ~ 1 n s^{-1} should thus be achievable for a regeneration experiment at HIBEAM.

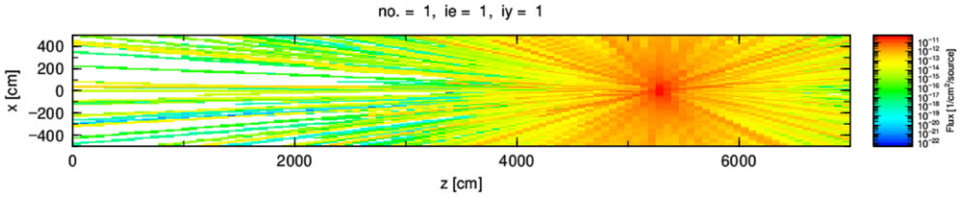

Figure 35. Photon tracks produced from the interaction of the ANNI neutrons with the carbon-12 target. The origin of the coordinate system is in the experimental area, after ANNI's curved guide extraction.

10.3. Background mitigation strategies

The main methods to suppress the expected backgrounds for HIBEAM and NNBAR in neutron–antineutron searches are:

- Prepare a control background sample by 'switching off' all active magnetic shielding elements of the experiment, allowing the Earth's field to suppress the neutron transformation effect, but leaving the entire experiment unperturbed in the process. This could be done during beam-off and beam-on periods, as well as partially characterized with a similar target-detector configuration during an HIBEAM $n \to n' \to \bar{n}$ experiment
- Add one or more targets downstream of the annihilation target but within the sensitive volume of the detector to produce additional 'sources' for background events without an annihilation signal. Any antineutron produced in the original cold neutron beam would be removed by the primary annihilation target [110].
- Suppress the generation of gamma backgrounds produced by neutron capture on target via demanding multiple 'track-like' cuts on the detector, since these events do not create tracks.
    - Tracking these particles back to a common vertex ($\pm$ several mm^3) to resolution smaller than the total beam spot on target will be important.
- Design a CR veto or, with a modern fast-timing calorimeter, use the entire calorimeter as a CR veto, coupled with vertex reconstruction capability, in order to reduce muon events.
    - Rejection of neutral CR events is to be accomplished by background subtraction via directly measured rates within the detector setup, along with energy deposition and multiple track cuts.

10.3.1. Gamma backgrounds from target. A preliminary estimation of gamma emission from the annihilation target due to neutron capture was done for HIBEAM. McStas simulated events [39] for the ANNI beam were used for the neutron source assuming ESS operating at 1 MW and the ANNI neutron current 6.4 $\times 10^{10}$ neutrons s^{-1}. The simulation was implemented in Phits [201] using a carbon-12 target of 1 m diameter. The distance from the neutron source to the target was assumed to be of 53 m, with a target thickness of 100 μm. Gravitational effects acting on the neutrons were not taken into account in the simulation.

Figure 35 shows a top view of the photon tracks obtained by Phits due to the interaction of the ANNI neutron beam with the carbon-12 target. As the HIBEAM detector will completely surround the target, these photon tracks represent an important background source that will be further studied in dedicated detector simulations in the near future.

The photon current from the target is obtained by Phits. The current is calculated such that any photon crossing the target surface adds 1 to the current. By multiplying the photon current with the incident neutron current and target area, the photon rate emission from the target over the full energy spectrum can be estimated. The photon rate calculated by Phits is 3.15×10^5 photons s^{-1}. Furthermore, since the collaboration is also exploring the use of beryllium-9 as the material for the target, the photon rate from neutron capture for it was also estimated for it in Phits and found to be 6.68×10^5 photons s^{-1}.

11. Future directions

In addition to the work outlined in the previous sections, the collaboration is pursuing possibilities to further enhance the sensitivity to neutron conversions and quantify and suppress backgrounds. A fundamental aim is to design a background-free $n \to n$ search, as achieved at the ILL. Similarly, backgrounds to mirror neutron searches need also to be minimized.

To achieve the above, a full Monte Carlo-based model of different designs of the annihilation detector is being constructed. Simulated background and signal processes will be used to optimize the experiment's sensitivity. These simulations will be informed and optimized with the experience of early running and tests at the ESS.

The work will dovetail with the Horizon2020 HighNESS project to design a liquid deuterium moderator and associated instruments including NNBAR.

Hardware R & D is also planned to support the simulation effort. Work has started on a prototype calorimeter module which would take part in a neutron test beam at the ESS in 2023 for *in situ* background measurements. The calorimeter module is described in the appendix.

Cost estimation and reduction will also be done. A potentially important way to reduce the cost is to exploit the possibility of allowing neutrons to bounce without 'resetting the clock' (section 3.2). There are laboratory experiments which can shed light on the validity of these ideas. The formula used for the antineutron–nucleus reflectivity deviates strongly from the usual Fresnel shape familiar from light optics due to the very large effect of the imaginary part of the antineutron optical potential. The accuracy of the neutron reflectivity formula in this extreme limit has been verified by neutron reflectometry measurements on gadolinium, which is an element with two isotopes that possess a very high neutron absorption cross section comparable in size to that possessed by antineutrons [202, 203]. It would also be very interesting to test theoretical calculations of nbar-A scattering amplitudes with data from slow antiprotons (there is essentially no hope to get slow antineutrons for scattering experiments) as long as theory can handle the Coulomb corrections to extract the nuclear component of the scattering from the data. Experiments with very cold antiprotons available at CERN could also be envisaged.

Other strategies which may impact cost are optimization of the distance from the entrance aperture of the neutron reflector system to the moderator, potentially reducing the size of the optical system dramatically, and relaxing magnetic shielding requirements while still sufficiently satisfying the quasi-free condition [108].

12. Summary

Strong theoretical motivations addressing open questions in modern physics such as the matter–antimatter asymmetry, the nature of dark matter and the possible Majorana nature of the neutrino imply the existence of neutron conversions into anti-neutrons and/or sterile neutrons. A remarkable opportunity has arisen to conduct a two-stage experiment (HIBEAM leading to

NNBAR) to be hosted by the ESS, which will perform a series of high precision, world-leading neutron conversion searches. The final goal is to achieve a sensitivity in searching for $n \to \bar{n}$ with free neutrons which is three orders of magnitude higher than the last such experiment. A collaboration to carry out this program has been formed with the aim of performing the experiment.

Acknowledgments

D Milstead gratefully acknowledges support from the Swedish Research Council. The work of Z Berezhiani is supported in part by CETEMPs at the University di L'Aquila. The work of Y Kamyshkov was supported in part by US DOE Grant DE-SC0014558. The work of S Girmohanta and R Shrock is supported in part by US NSF Grant NSF-PHY-1915093. The work of L Varriano is supported by a US National Science Foundation (NSF) Graduate Research Fellowship under Grant No. DGE-1746045. B Kerbikov is supported by RSF Grant 16-12-10414. Rabrindra Mohapatra gratefully acknowledges support from the NSF via the Grant: PHY-1914631. B Kopeliovich and I Potashnikova acknowledge Grants ANID—Chile FONDECYT 1170319, and ANID PIA/APOYO AFB180002. A Young is supported by the NSF Grant PHY-1914133 and the DOE Grant DE-FG02-ER41042. W M Snow acknowledges support from US National Science Foundation Grant PHY-1914405 and the Indiana University Center for Spacetime Symmetries. J L Barrow's work was supported by the US Department of Energy, Office of Science, Office of Workforce Development for Teachers and Scientists, Office of Science Graduate Student Research (SCGSR) program. The SCGSR program is administered by the Oak Ridge Institute for Science and Education for the DOE under Contract No. DESC0014664. J L Barrow was also partially supported in part by the Visiting Scholars Award Program of the Universities Research Association. The work of P S B Dev is supported in part by the US Department of Energy under Grant No. DE-SC0017987, by the Neutrino Theory Network Program Grant No. DE-AC02-07CHI11359, and by a Fermilab Intensity Frontier Fellowship. L J Broussard is supported by the US DOE under Contract DE-AC05-00OR2272. This work is also funded by the European Union Framework Program for Research and Innovation Horizon 2020 in the HighNESS project, under Grant Agreement 951782.

Data availability statement

The data that support the findings of this study are available upon reasonable request from the authors.

Appendix A. Prototype development and the ESS test beam line (TBL)

In this appendix, a description is given of the prototype detector development which would be deployed at an ESS test beam. The test beam is also described.

A.1. Prototype calorimeter module

As described in section 8 an annihilation detector must provide as reliable and selective information as possible in each individual event. The crucial information is event topology and conservation of energy and momentum. For free $\bar{n}n$ annihilation events, identifying and measuring total energy and momentum of all outgoing particles gives unique annihilation signatures and one should measure these parameters with the best possible resolution since the discriminating

cuts will be limited by the resolution by which the kinetic energy has been measured. However, $\bar{n}n$ annihilation in nuclei (carbon in this case) introduces additional means to dissipate energy and momentum by nuclear fragments. Some of the energy cannot be captured as it is carried by neutrons. Energy carried with protons (and to some minor extent composite fragments) can be measured, but particle identification is important since the proton rest mass shall not be included in the total invariant mass. Taken together, the total invariant mass of pions and photons will only be equal to two neutron masses in about 30% of the cases when the annihilation takes place in a carbon nucleus (see figure 4).

If the kinetic energy of charged nuclear fragments is also measured, this will narrow the distribution, but it is clear that a selection on invariant mass has to be quite generous in order to avoid cutting away good annihilation events. As a consequence, it makes no sense to strive at the highest possible energy resolution. This is actually quite satisfying, since, in particular the charged hadrons are in a very difficult energy regime where energies are often too high to be absorbed by electromagnetic processes only, and the statistical significance on energy deposit by strong interactions is extremely poor. Thus, optimization of the calorimetry is important. Figure 2 illustrates the simulated kinetic energy/momentum distributions of the charged hadrons expected in an annihilation event. Given the distributions shown, an energy resolution for charged hadrons of ± 5 MeV appears to be more than sufficient.

The principles

The topological aspects of annihilation events to be handled by the tracking must be considered together with the need that the tracking will provide a $\frac{dE}{dx}$ measurement. Since tracks are resolved in three-dimensional space, the track direction for charged particles into the calorimeter is accurately determined. Thus, safe particle identification by combining $\frac{dE}{dx}$ and energy is achieved. Background of gamma radiation in the MeV range will be very high. To cope with this background, a high granularity, in space and time, using a large number of detector elements and electronic readout channels is needed. This will be one guideline for a calorimeter design. As pointed out, the kinetic energy resolution can be rather relaxed. For charged hadrons this may pay off in a simple calorimeter design. For photons, however, one should still strive at good energy resolution in order to obtain a narrow invariant mass peak for the identification of the neutral pions.

A.1.1. The tentative calorimeter design. A hybrid approach is adopted for the calorimeter with ten, 3 cm thick layers of plastic scintillators reaching a total thickness of 30 cm followed by a 25 cm (ca 20 radiation lengths) of lead glass for the electromagnetic calorimetry. A Geant-4 [204] visualization of the response of the set-up to a charged pion with 240 MeV kinetic energy is shown in figure A1. The pion punches through the scintillators leaving a cone a Cherenkov light in the lead glass.

The hadron calorimeter with 30 cm thickness is sufficient to stop protons with more than 200 MeV kinetic energy. About 80% of protons in the high energy end of the spectrum will come to rest without a nuclear interaction. This will cover effectively all protons that happen to be emitted from the annihilation point (figure 2, bottom). However, 30 cm of plastic will only stop pions up to about 80 MeV kinetic energy (260 MeV in momentum, figure 2, top) which is only about 30% of the expected pion spectrum. Charged pions passing through additional 25 cm of lead glass will have about 250 MeV kinetic energy i.e. momentum about 400 MeV which would account for another 30% of the pion spectrum. Even if one can calibrate the energy response by Cherenkov radiation, one cannot expect to make a proper energy measurement since most charged hadrons passing this amount of matter will suffer one or a few hadron nucleus collisions with a rather unpredictable energy signal as result. The very low number of collisions is the reason that hadron calorimetry by showering is not a viable technique at

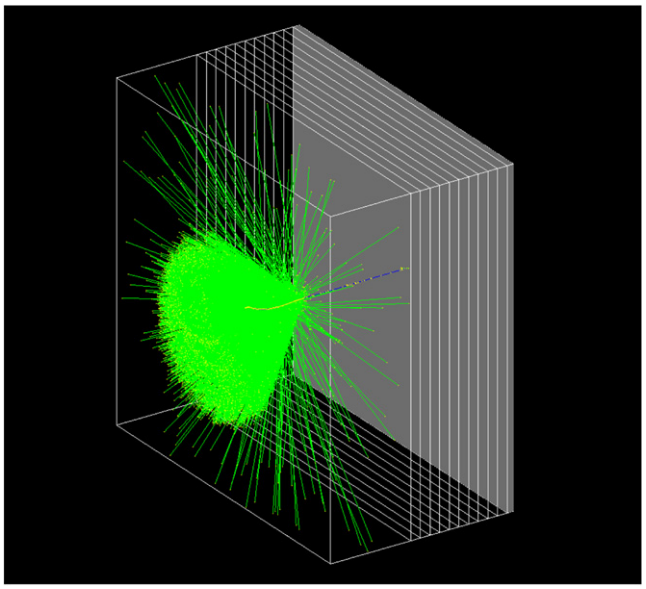

Figure A1. A Geant-4 visualization of a calorimeter module with ten layers of plastic scintillator and a lead-glass block. The Cerenkov photons (green) are shown as is the pion track.

these energies. Actually, the nuclear fragments from these hadronic collisions will not produce Cherenkov light. Thus, calibrated Cherenkov light for charged pions will mostly reflect the range of the pion until it makes a collision. Figure A2 shows the clear, almost linear relation between range and the amount of Cherenkov light, as predicted using Geant-4. Note that only pions with 240 MeV have been injected. Ideally one should have only a sharp peak at about 7000 photons, but anything lower than that is due to collisions on the way.

Considering all of the above, the strategy is to use the plastic scintillator stack for a range measurement, where each scintillator defines a kinetic energy bin in the proton and pion spectra and the Cherenkov light in the lead glass as a measure of the charged pion range in the lead glass. For cases where a particle comes to rest by electromagnetic energy loss only, the range will give the kinetic energy (since the particle mass is known by the particle identification) with an adequate resolution. In case of a hadronic interaction in the detector materials, one must differ between protons and pions. For protons one should be able to know if a nuclear reaction has taken place since there will be a clear correlation between $\frac{\mathrm{d}E}{\mathrm{d}x}$ and range which is violated if a reaction takes place. The $\frac{\mathrm{d}E}{\mathrm{d}x}$ value itself can, if good enough energy loss resolution is achieved, provide complementary energy information, unaffected by the hadronic collision. For pions however, which almost all will be near minimum ionizing, there is no such correlation between $\frac{\mathrm{d}E}{\mathrm{d}x}$ and range, and one will only be able to state the range of the pion for as long as it was a pion. The charged pions produce Cherenkov light down to quite low kinetic energies in lead glass.

By limiting the information from the plastic layers to hit/no hit information, the light read-out and the readout electronics can be made simple (a discriminator threshold only) and cheap, thus allowing a very high segmentation to the benefit of handling the gamma background. The

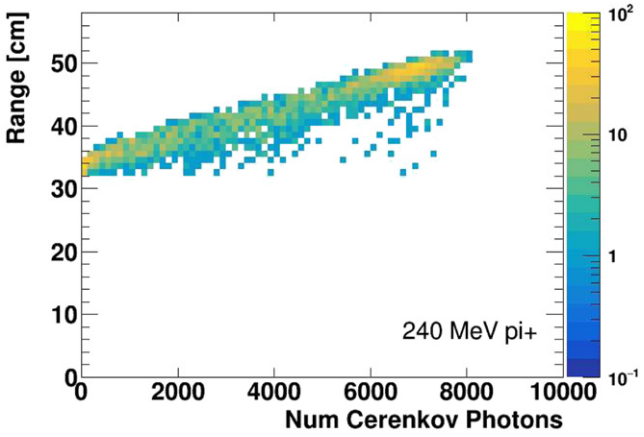

Figure A2. The relationship between range and amount of Cherenkov light for charged pions with 240 MeV kinetic energy, as predicted by Geant-4. Pions with this energy reach into around 20 cm into the lead glass.

scintillator thicknesses will be chosen such that minimum ionizing particles will give substantially larger signals than Compton electrons from gammas. With 3 cm thickness of scintillating plastic, an MIP will deposit about 6 MeV, much above gammas with nuclear physics origin.

The plastic scintillator layers will be segmented in a way such that coarse tracking in 3D can be done on the hit/no-hit information that is available on a nanosecond time scale. Thus a powerful and fast track trigger can be constructed. Different ways of extracting and sensing the light from the scintillator segments will be investigated in order to optimize the solution for cost, performance and segmentation, taking advantage of the moderate resolution required. The lead glass will have a good energy resolution, being sensitive over the whole volume. Cherenkov light has the advantage of being direction-sensitive. This gives the possibility to measure the direction of particles or even make it blind to particles in the wrong direction. This would be important to discriminate against fake events of CR origin. This is an important R & D topic. The resolution by which the point of impact of gammas from π^0 decay shall be good in order to obtain good resolution in the reconstruction of π^0.

This will drive the lateral segmentation of the lead glass either as lead glass blocks or a segmentation of the light readout. Whether or not the readout is direct by photomultipliers or via wavelength shifting fibers is also an R & D item. One could think of segmenting the 25 cm of lead glass in the depth dimension to better measure the range of charged pions. It is questionable if it is worth the increased cost of light sensors and electronics. Possibly, the cost of the lead glass itself is balancing the cost of more readout.

To conclude, it is considered that this unusual detector application aimed for too high energy for nuclear physics and too low energy for particle physics methods offers many interesting detector R & D challenges. It is anticipated that it would be deployed in the ESS test beam described below. The prototype would be supplemented with a scintillator cosmic shield and an inner TPC.

A.2. The ESS test beam

A dedicated test beam line (TBL) will be build at the ESS to be used initially to verify that the accelerator has successfully delivered beam on target, and to characterize the pulsed neutron

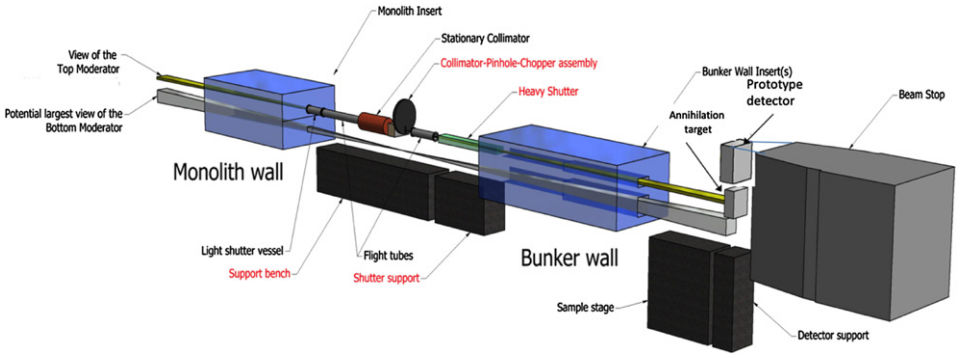

Figure A3. Overview of the planned ESS test beam set-up. A collimated beam would be passed to the carbon target and then to the detector prototype.

beam emitted from the upper moderator (e.g. time structure, spatial distribution, energy dependence etc), while it can be adjusted to also view a future lower moderator. In the longer term, it will provide supporting measurements for the user program and also serve for the development of key neutron technologies, such as optical components, choppers, and detector systems. For the last mentioned purpose, the ESS TBL is an ideal place to perform tests of the prototypes of HIBEAM/NNBAR detectors. Figure A3 shows a schematic overview of the TBL. In its basic configuration, it is a pin-hole (camera obscura) imaging station for viewing the entire width and height of the moderator assembly, with a double-disc chopper at the pin-hole position to provide tuneable wavelength resolution and wavelength band selection. For the moderator characterization, a position sensitive detector will be placed at 17 m from the moderator with an adjustable pin-hole at the half-way position, enabling the spatial imaging of neutrons of different wavelengths emerging from the moderator. The instrument will be in direct line-of-sight and not be equipped with optics, but in addition to the double disk chopper will have a series of collimators (one stationary and one adjustable in size), a range of optional beam attenuators and filters, and a heavy shutter. The test for the HIBEAM/NNBAR detectors will be done in combination with the annihilation target. After hitting the annihilation target, the beam will be absorbed in a beam stop that is already part of the TBL. With a direct view of the source, the TBL represents also an optimal place to make background measurements since it will not only provide cold but also fast and high energy neutrons as can be seen in figure A4.

Planned measurements include:

- Test of the full prototype detector
- Benchmark against experimental data of Monte Carlo background simulations
- Gamma background measurements from neutron interaction and activation with the annihilation target and surrounding materials
- Fast neutron background measurements
- CRs and skyshine background characterization

All these measurements will allow a deep understanding of the background and provide a better mitigation strategy both for HIBEAM and the NNBAR experiment. Finally, it is worth mentioning that most of the backgrounds, along with the signal Monte Carlo events provided by the authors reference [172], have already been preliminarily simulated and interfaced with

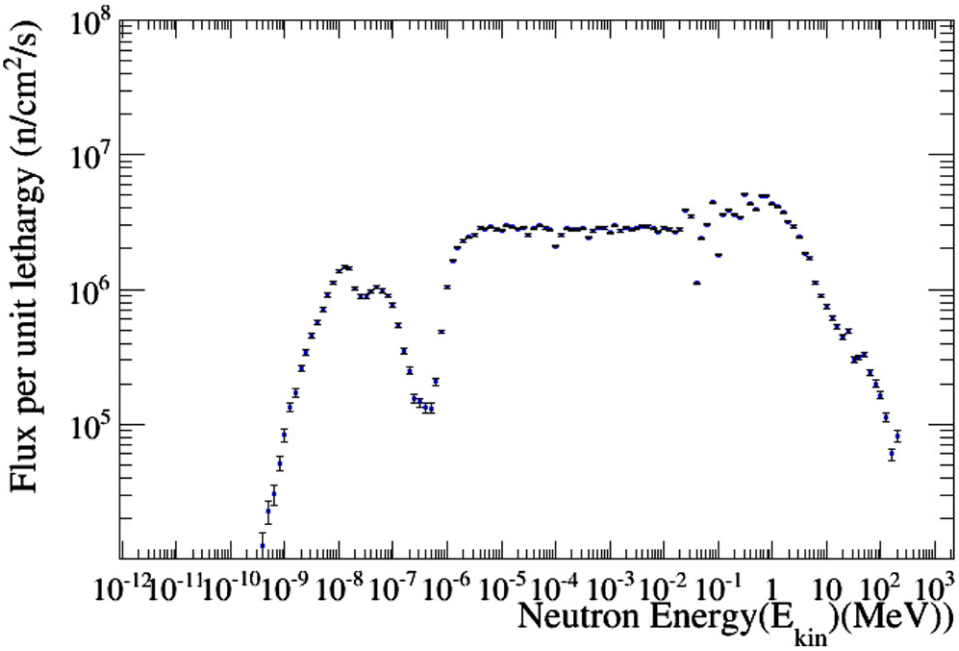

Figure A4. Neutron energy spectrum at the location of the annihilation target location of the TBL.

a simulation of the NNBAR–HIBEAM detector in Geant4 via a coherent software framework. The results will be described in a forthcoming publication.

ORCID iDs

L J Broussard https://orcid.org/0000-0001-9182-2808
D Milstead https://orcid.org/0000-0002-7788-4129

References

[1] 't Hooft G 1976 Computation of the quantum effects due to a four-dimensional pseudoparticle *Phys. Rev.* D **14** 3432–50
't Hooft G 1978 *Phys. Rev.* D **18** 2199 (erratum)
[2] Kuzmin V A, Rubakov V A and Shaposhnikov M E 1987 Anomalous electronweak baryon number non-conservation and GUT mechanism for baryogenesis *Phys. Lett.* B **191** 171–3
[3] Dolgov A 1992 Non-GUT baryogenesis *Phys. Rep.* **222** 309–86
[4] Smith G L, Hoyle C D, Gundlach J H, Adelberger E G, Heckel B R and Swanson H E 2000 Short range tests of the equivalence principle *Phys. Rev.* D **61** 022001
[5] Schlamminger S, Choi K Y, Wagner T A, Gundlach J H and Adelberger E G 2008 Test of the equivalence principle using a rotating torsion balance *Phys. Rev. Lett.* **100** 041101
[6] Cowsik R *et al* 2019 Test of Einstein's equivalence principle with a long-period torsion balance (arXiv:1808.09925 [gr-qc])
[7] Sakharov A D 1967 Violation of *CP* invariance, *C* asymmetry, and baryon asymmetry of the universe *Pisma Zh. Eksp. Teor. Fiz.* **5** 32–5
Sakharov A D 1991 *Usp. Fiz. Nauk* **161** 61

[8] Kuzmin V A 1970 Cp violation and baryon asymmetry of the universe *Pisma Zh. Eksp. Teor. Fiz.* **12** 335–7
[9] Mohapatra R N and Marshak R E 1980 Phenomenology of neutron oscillations *Phys. Lett.* B **94** 183
Mohapatra R N and Marshak R E 1980 *Phys. Lett.* B **96** 444 (erratum)
[10] Phillips D G II *et al* 2016 Neutron–antineutron oscillations: theoretical status and experimental prospects *Phys. Rep.* **612** 1–45
[11] Chang L-N and Chang N-P 1980 $B - L$ nonconservation and neutron oscillation *Phys. Lett.* B **92** 103–6
[12] Kuo T K and Love S T 1980 Neutron oscillations and the existence of massive neutral leptons *Phys. Rev. Lett.* **45** 93
[13] Cowsik R and Nussinov S 1981 Some constraints on $\Delta B = 2$ neutron–antineutron oscillations *Phys. Lett.* B **101** 237–40
[14] Rao S and Shrock R 1982 $n \leftrightarrow \bar{n}$ transition operators and their matrix elements in the MIT bag model *Phys. Lett.* B **116** 238–42
[15] Rao S and Shrock R E 1984 Six fermion ($B - L$) violating operators of arbitrary generational structure *Nucl. Phys.* B **232** 143–79
[16] Caswell W E, Milutinović J and Senjanović G 1983 Matter–antimatter transition operators: a manual for modeling *Phys. Lett.* B **122** 373–7
[17] Berezhiani Z and Bento L 2006 Neutron–mirror neutron oscillations: how fast might they be? *Phys. Rev. Lett.* **96** 081801
[18] Berezhiani Z 2009 More about neutron–mirror neutron oscillation *Eur. Phys. J.* C **64** 421–31
[19] Grojean C, Shakya B, Wells J D and Zhang Z 2018 Implications of an improved neutron–antineutron oscillation search for baryogenesis: a minimal effective theory analysis *Phys. Rev. Lett.* **121** 171801
[20] Bringmann T, Cline J M and Cornell J M 2019 Baryogenesis from neutron-dark matter oscillations *Phys. Rev.* D **99** 035024
[21] Mohapatra R N and Marshak R E 1980 Local $B - L$ symmetry of electroweak interactions, Majorana neutrinos and neutron oscillations *Phys. Rev. Lett.* **44** 1316–9
Mohapatra R N and Marshak R 1980 *Phys. Rev. Lett.* **44** 1643 (erratum)
[22] Babu K S, Mohapatra R N and Nasri S 2006 Post-sphaleron baryogenesis *Phys. Rev. Lett.* **97** 131301
[23] Dev P S B and Mohapatra R N 2015 TeV scale model for baryon and lepton number violation and resonant baryogenesis *Phys. Rev.* D **92** 016007
[24] Allahverdi R, Dev P S B and Dutta B 2018 A simple testable model of baryon number violation: baryogenesis, dark matter, neutron–antineutron oscillation and collider signals *Phys. Lett.* B **779** 262–8
[25] Barbier R *et al* 2005 *R*-parity-violating supersymmetry *Phys. Rep.* **420** 1–195
[26] Calibbi L, Ferretti G, Milstead D, Petersson C and Pöttgen R 2016 Baryon number violation in supersymmetry: n-nbar oscillations as a probe beyond the LHC *J. High Energy Phys.* JHEP05(2016)144
Calibbi L, Ferretti G, Milstead D, Petersson C and Pöttgen R 2017 *J. High Energy Phys.* JHEP10(2017)195 (erratum)
[27] Nussinov S and Shrock R 2002 Neutron–antineutron oscillations in models with large extra dimensions *Phys. Rev. Lett.* **88** 171601
[28] Girmohanta S and Shrock R 2020 Baryon-number-violating nucleon and dinucleon decays in a model with large extra dimensions *Phys. Rev.* D **101** 015017
[29] Girmohanta S and Shrock R 2020 Nucleon decay and n-$\bar{n}$ oscillations in a left–right symmetric model with large extra dimensions *Phys. Rev.* D **101** 095012
[30] Berezhiani Z and Bento L 2006 Fast neutron–mirror neutron oscillation and ultra high energy cosmic rays *Phys. Lett.* B **635** 253–9
[31] Berezhiani Z and Gazizov A 2012 Neutron oscillations to parallel world: earlier end to the cosmic ray spectrum? *Eur. Phys. J.* C **72** 2111
[32] Mohapatra R N 2009 Neutron–anti-neutron oscillation: theory and phenomenology *J. Phys. G: Nucl. Part. Phys.* **36** 104006
[33] Berezhiani Z 2016 Neutron–antineutron oscillation and baryonic majoron: low scale spontaneous baryon violation *Eur. Phys. J.* C **76** 705

[34] Arnold J M, Fornal B and Wise M B 2013 Simplified models with baryon number violation but no proton decay *Phys. Rev.* D **87** 075004
[35] Mohapatra R N and Senjanović G 1983 Spontaneous breaking of global $B - L$ symmetry and matter–antimatter oscillations in grand unified theories *Phys. Rev.* D **27** 254
[36] Senjanovic G 1982 Higgs mass scales and matter–antimatter oscillations in grand unified theories *Workshop on Neutrino–Antineutrino Oscillations* vol 4
[37] Baldo-Ceolin M *et al* 1994 A new experimental limit on neutron–antineutron oscillations *Z. Phys.* C **63** 409–16
[38] Brooijmans G *et al* 2015 Expression of interest for a new search for neutron–antineutron oscillations at the ESS
[39] Soldner T, Abele H, Konrad G, Märkisch B, Piegsa F M, Schmidt U, Theroine C and Sánchez P T 2019 ANNI—a pulsed cold neutron beam facility for particle physics at the ESS *EPJ Web Conf.* **219** 10003
[40] Ban G *et al* 2007 A direct experimental limit on neutron: mirror neutron oscillations *Phys. Rev. Lett.* **99** 161603
[41] Serebrov A P *et al* 2008 Experimental search for neutron–mirror neutron oscillations using storage of ultracold neutrons *Phys. Lett.* B **663** 181–5
[42] Altarev I *et al* 2009 Neutron to mirror-neutron oscillations in the presence of mirror magnetic fields *Phys. Rev.* D **80** 032003
[43] Bodek K *et al* 2009 Additional results from the first dedicated search for neutron–mirror neutron oscillations *Nucl. Instrum. Methods Phys. Res.* A **611** 141–3
[44] Serebrov A P *et al* 2009 Search for neutron–mirror neutron oscillations in a laboratory experiment with ultracold neutrons *Nucl. Instrum. Methods Phys. Res.* A **611** 137–40
[45] Berezhiani Z and Nesti F 2012 Magnetic anomaly in UCN trapping: signal for neutron oscillations to parallel world? *Eur. Phys. J.* C **72** 1974
[46] Berezhiani Z, Biondi R, Geltenbort P, Krasnoshchekova I A, Varlamov V E, Vassiljev A V and Zherebtsov O M 2018 New experimental limits on neutron–mirror neutron oscillations in the presence of mirror magnetic field *Eur. Phys. J.* C **78** 717
[47] Abel C *et al* (nEDM Collaboration) 2021 A search for neutron to mirror-neutron oscillations using the nEDM apparatus at PSI *Phys. Lett.* B **812** 135993
[48] Schmidt U 2007 An experimental limit on neutron mirror-neutron oscillation *Search for Baryon and Lepton number Violations Int. Workshop*
[49] Berezhiani Z and Vainshtein A 2015 Neutron–antineutron oscillation as a signal of CP violation (arXiv:1506.05096 [hep-ph])
[50] Dvali G and Gabadadze G 1999 Non-conservation of global charges in the brane universe and baryogenesis *Phys. Lett.* B **460** 47–57
[51] Dutta B, Mimura Y and Mohapatra R 2006 Observable neutron–antineutron oscillation in high scale seesaw models *Phys. Rev. Lett.* **96** 061801
[52] Dvali G and Redi M 2009 Phenomenology of 10^{32} dark sectors *Phys. Rev.* D **80** 055001
[53] Abe K *et al* (Super-Kamiokande Collaboration) 2015 The search for $n - \bar{n}$ oscillation in Super-Kamiokande I *Phys. Rev.* D **91** 072006
[54] Gustafson J *et al* (Super-Kamiokande Collaboration) 2015 Search for dinucleon decay into pions at Super-Kamiokande *Phys. Rev.* D **91** 072009
[55] Sussman S *et al* (Super-Kamiokande Collaboration) 2018 Dinucleon and nucleon decay to two-body final states with no hadrons in Super-Kamiokande (arXiv:1811.12430 [hep-ex])
[56] Girmohanta S and Shrock R 2020 Improved upper limits on baryon-number violating dinucleon decays to dileptons *Phys. Lett.* B **803** 135296
[57] Abe K *et al* (Super-Kamiokande Collaboration) 2021 Neutron–antineutron oscillation search using a 0.37 Megaton·Year exposure of Super-Kamiokande *Phys. Rev.* D **103** 012008
[58] Weinberg S 1979 Cosmological production of baryons *Phys. Rev. Lett.* **42** 850–3
[59] Fry J N, Olive K A and Turner M S 1980 Hierarchy of cosmological baryon generation *Phys. Rev. Lett.* **45** 2074
[60] Yoshimura M 1978 Unified gauge theories and the baryon number of the universe *Phys. Rev. Lett.* **41** 281–4
Yoshimura M 1979 *Phys. Rev. Lett.* **42** 746 (erratum)
[61] Ellis J, Gaillard M K and Nanopoulos D V 1979 Baryon number generation in grand unified theories *Phys. Lett.* B **80** 360
Ellis J R, Gaillard M K and Nanopoulos D V 1979 *Phys. Lett.* B **82** 464 (erratum)

[62] Morrissey D E and Ramsey-Musolf M J 2012 Electroweak baryogenesis *New J. Phys.* **14** 125003
[63] Fukugita M and Yanagida T 1986 Barygenesis without grand unification *Phys. Lett.* B **174** 45–7
[64] Weinberg S 1979 Baryon- and lepton-nonconserving processes *Phys. Rev. Lett.* **43** 1566–70
[65] Mohapatra R N and Senjanović G 1980 Neutrino mass and spontaneous parity nonconservation *Phys. Rev. Lett.* **44** 912
[66] Kuzmin V A, Rubakov V A and Shaposhnikov M E 1985 On anomalous electroweak baryon-number non-conservation in the early universe *Phys. Lett.* B **155** 36
[67] Asaka T and Shaposhnikov M 2005 The νMSM, dark matter and baryon asymmetry of the universe *Phys. Lett.* B **620** 17–26
[68] Asaka T, Blanchet S and Shaposhnikov M 2005 The νMSM, dark matter and neutrino masses *Phys. Lett.* B **631** 151–6
[69] Bento L and Berezhiani Z 2001 Leptogenesis via collisions: the lepton number leaking to the hidden sector *Phys. Rev. Lett.* **87** 231304
[70] Bento L and Berezhiani Z 2002 Baryon asymmetry, dark matter and the hidden sector *Fortschr. Phys.* **50** 489–95
[71] Berezhiani Z 2008 Unified picture of ordinary and dark matter genesis *Eur. Phys. J. Spec. Top.* **163** 271–89
[72] Babu K, Bhupal Dev P and Mohapatra R 2009 Neutrino mass hierarchy, neutron–antineutron oscillation from baryogenesis *Phys. Rev.* D **79** 015017
[73] Babu K S, Bhupal Dev P S, Fortes E C F S and Mohapatra R N 2013 Post-sphaleron baryogenesis and an upper limit on the neutron–antineutron oscillation time *Phys. Rev.* D **87** 115019
[74] Berezhiani Z 2018 Matter, dark matter, and antimatter in our universe *Int. J. Mod. Phys.* A **33** 1844034
[75] Feng J L 2010 Dark matter candidates from particle physics and methods of detection *Annu. Rev. Astron. Astrophys.* **48** 495–545
[76] Berezhiani Z G, Dolgov A D and Mohapatra R N 1996 Asymmetric inflationary reheating and the nature of mirror universe *Phys. Lett.* B **375** 26–36
[77] Mohapatra R N and Teplitz V L 2000 Mirror dark matter and galaxy core densities of galaxies *Phys. Rev.* D **62** 063506
[78] Berezhiani Z, Comelli D and Villante F L 2001 The early mirror universe: inflation, baryogenesis, nucleosynthesis and dark matter *Phys. Lett.* B **503** 362–75
[79] Foot R 2014 Mirror dark matter: cosmology, galaxy structure and direct detection *Int. J. Mod. Phys.* A **29** 1430013
[80] Essig R *et al* 2013 Working group report: new light weakly coupled particles *Proc., 2013 Community Summer Study on the Future of US Particle Physics: Snowmass on the Mississippi (CSS2013)* (Minneapolis, MN, USA 29 July–6 August 2013) arXiv:1311.0029 [hep-ph]
[81] Holdom B 1986 Two U(1)'s and ϵ charge shifts *Phys. Lett.* B **166** 196–8
[82] Berezhiani Z G and Mohapatra R N 1995 Reconciling present neutrino puzzles: sterile neutrinos as mirror neutrinos *Phys. Rev.* D **52** 6607–11
[83] Berezhiani Z G 1996 Astrophysical implications of the mirror world with broken mirror parity *Acta Phys. Polon.* B **27** 1503–16 arXiv:hep-ph/9602326
[84] Berezhiani Z 2004 Mirror world and its cosmological consequences *Int. J. Mod. Phys.* A **19** 3775–806
[85] Berezhiani Z 2005 Through the looking-glass: Alice's adventures in mirror world (arXiv:hep-ph/0508233)
[86] Okun L B 2007 Mirror particles and mirror matter: 50 years of speculations and search *Phys.-Usp.* **50** 380–9
[87] Berezhiani Z 2019 Neutron lifetime puzzle and neutron–mirror neutron oscillation *Eur. Phys. J.* C **79** 484
[88] Berezhiani Z, Biondi R, Kamyshkov Y and Varriano L 2019 On the neutron transition magnetic moment *Physics* **1** 271–89
[89] Wietfeldt F 2018 Measurements of the neutron lifetime *Atoms* **6** 70
[90] Georgi H and Glashow S L 1974 Unity of all elementary-particle forces *Phys. Rev. Lett.* **32** 438–41
[91] Glashow S L 1980 The future of elementary particle physics *NATO Sci. Ser.* B **61** 687
[92] Dolgov A D and Urban F R 2006 Baryogenesis by *R*-parity violating top quark decays and neutron–antineutron oscillations *Nucl. Phys.* B **752** 297–315
[93] Bambi C, Dolgov A D and Freese K 2007 A black hole conjecture and rare decays in theories with low scale gravity *Nucl. Phys.* B **763** 91–114

[94] Schwarz J H 1982 Superstring theory *Phys. Rep.* **89** 223–322
[95] Senjanovic G and Mohapatra R N 1975 Exact left–right symmetry and spontaneous violation of parity *Phys. Rev.* D **12** 1502
[96] Senjanovic G 1979 Spontaneous breakdown of parity in a class of gauge theories *PhD thesis* City Coll, New York
[97] Mohapatra R N and Senjanović G 1981 Neutrino masses and mixings in gauge models with spontaneous parity violation *Phys. Rev.* D **23** 165
[98] de Gouvea A, Herrero-Garcia J and Kobach A 2014 Neutrino masses, grand unification, and baryon number violation *Phys. Rev.* D **90** 016011
[99] Keung W-Y and Senjanović G 1983 Majorana neutrinos and the production of the right-handed charged gauge boson *Phys. Rev. Lett.* **50** 1427
[100] Tello V, Nemevsek M, Nesti F, Senjanovic G and Vissani F 2011 Left–right symmetry: from LHC to neutrinoless double beta decay *Phys. Rev. Lett.* **106** 151801
[101] Babu K S and Mohapatra R N 2015 Determining Majorana nature of neutrino from nucleon decays and $n - \bar{n}$ oscillations *Phys. Rev.* D **91** 013008
[102] Berezhiani Z and Vainshtein A 2019 Neutron–antineutron oscillations: discrete symmetries and quark operators *Phys. Lett.* B **788** 58–64
[103] Berezhiani Z and Vainshtein A 2018 Neutron–antineutron oscillation and discrete symmetries *Int. J. Mod. Phys.* A **33** 1844016
[104] Addazi A, Berezhiani Z and Kamyshkov Y 2017 Gauged $B - L$ number and neutron–antineutron oscillation: long-range forces mediated by baryophotons *Eur. Phys. J.* C **77** 301
[105] Babu K and Mohapatra R N 2016 Limiting equivalence principle violation and long-range baryonic force from neutron–antineutron oscillation *Phys. Rev.* D **94** 054034
[106] Bitter T and Dubbers D 1985 Test of the quasifree condition in neutron oscillation experiments *Nucl. Instrum. Methods Phys. Res.* A **239** 461–6
[107] Schmidt U, Bitter T, El-Muzeini P, Dubbers D and Schärpf O 1992 Long distance propagation of a polarized neutron beam in zero magnetic field *Nucl. Instrum. Methods Phys. Res.* A **320** 569–73
[108] Davis E D and Young A R 2017 Neutron–antineutron oscillations beyond the quasifree limit *Phys. Rev.* D **95** 036004
[109] Bressi G *et al* 1989 Search for free neutron–antineutron oscillations *Z. Phys.* C **43** 175–9
[110] Bressi G *et al* 1990 Final results of a search for free neutron–antineutron oscillations *Nuovo Cimento* A **103** 731–50
[111] Fidecaro G *et al* (CERN-Grenoble-Padua-Rutherford-Sussex Collaboration) 1985 Experimental search for neutron–antineutron transitions with free neutrons *Phys. Lett.* B **156** 122–8
[112] Costa G and Kabir P 1983 Environmental effects on possible neutron–antineutron transitions *Phys. Rev.* D **28** 667–8
[113] Kerbikov B O 2018 Lindblad and Bloch equations for conversion of a neutron into an antineutron *Nucl. Phys.* A **975** 59–72
[114] Gudkov V, Nesvizhevsky V, Protasov K, Snow W and Voronin A 2019 A new approach to search for free neutron–antineutron oscillations using coherent neutron propagation in gas (arXiv:1912.06730 [hep-ph])
[115] Cherry M l, Lande K, Lee C k, Steinberg R i and Cleveland B 1983 Experimental test of baryon conservation: a new limit on neutron antineutron oscillations in oxygen *Phys. Rev. Lett.* **50** 1354–6
[116] Krishnaswamy M R, Menon M G K, Mondal N K, Narasimham V S, Sreekantan B V, Hayashi Y, Ito N, Kawakami S and Miyake S 1986 Results from the KGF proton decay experiment *Il Nuovo Cimento* C **9** 167–81
Krishnaswamy M R, Menon M G K, Mondal N K, Narasimham V S, Sreekantan B V, Hayashi Y, Ito N, Kawakami S and Miyake S 1985 *Conf. Proc. C* vol 850418 p 97
[117] Battistoni G *et al* 1983 Nucleon stability, magnetic monopoles and atmospheric neutrinos in the Mont-Blanc experiment *Phys. Lett.* B **133** 454–60
[118] Jones T W *et al* (Irvine-Michigan-Brookhaven Collaboration) 1984 A search for $N\bar{N}$ oscillation in oxygen *Phys. Rev. Lett.* **52** 720
[119] Takita M *et al* (Kamiokande Collaboration) 1986 A search for neutron–antineutron oscillation in a ^{16}O nucleus *Phys. Rev.* D **34** 902
[120] Berger C *et al* (Frejus Collaboration) 1990 Search for neutron–antineutron oscillations in the Fréjus detector *Phys. Lett.* B **240** 237–42

[121] Chung J *et al* 2002 Search for neutron antineutron oscillations using multiprong events in Soudan 2 *Phys. Rev.* D **66** 032004
[122] Aharmim B *et al* (SNO Collaboration) 2017 Search for neutron–antineutron oscillations at the Sudbury neutrino observatory *Phys. Rev.* D **96** 092005
[123] Abi B *et al* (DUNE Collaboration) 2020 Deep underground neutrino experiment (DUNE), far detector technical design report, volume II DUNE physics (arXiv:2002.03005 [hep-ex])
[124] Barrow J L, Golubeva E S, Paryev E and Richard J-M 2020 Progress and simulations for intranuclear neutron–antineutron transformations in $^{40}_{18}$Ar *Phys. Rev.* D **101** 036008
[125] Hewes J E T 2017 Searches for bound neutron–antineutron oscillation in liquid argon time projection chambers *PhD Thesis* Manchester U. http://lss.fnal.gov/archive/thesis/2000/fermilab-thesis-2017-27.pdf
[126] Labarga L (Hyper-Kamiokande-Proto Collaboration) 2018 Potential of Hyper-Kamiokande at some non-accelerator physics and nucleon decay searches *Potential of Hyper-Kamiokande at some non-Accelerator Physics and Nucleon Decay Searches* vol EPS-HEP2017 (SISSA) p 117
[127] Dover C B, Gal A and Richard J M 1983 Neutron–antineutron oscillations in nuclei *Phys. Rev.* D **27** 1090–100
[128] Alberico W M, Bottino A and Molinari A 1982 A new evaluation of the oscillation time *Phys. Lett.* B **114** 266–70
[129] Alberico W M, Bernabeu J, Bottino A and Molinari A 1984 Neutron–antineutron mixing inside nuclei *Nucl. Phys.* A **429** 445–61
[130] Dover C B, Gal A and Richard J M 1989 Neutron–antineutron oscillations in nuclei *Nucl. Instrum. Methods Phys. Res.* A **284** 13
[131] Alberico W M, De Pace A and Pignone M 1991 Neutron–antineutron oscillations in nuclei *Nucl. Phys.* A **523** 488–98
[132] Hüfner J and Kopeliovich B Z 1998 Neutron–antineutron oscillations in nuclei revisited *Mod. Phys. Lett.* A **13** 2385–91
[133] Friedman E and Gal A 2008 Realistic calculations of nuclear disappearance lifetimes induced by neutron–antineutron oscillations *Phys. Rev.* D **78** 016002
[134] Nussinov S and Shrock R 2020 Using $\bar{p}p$ and e^+e^- annihilation data to refine bounds on the baryon-number-violating dinucleon decays $nn \to e^+e^-$ and $nn \to \mu^+\mu^-$ (arXiv:2005.12493 [hep-ph])
[135] Oosterhof F, Long B, de Vries J, Timmermans R and van Kolck U 2019 Baryon-number violation by two units and the deuteron lifetime *Phys. Rev. Lett.* **122** 172501
[136] Haidenbauer J and Meißner U-G 2020 Neutron–antineutron oscillations in the deuteron studied with NN and $\bar{N}N$ interactions based on chiral effective field theory *Chin. Phys.* C **44** 033101
[137] Wagner T A, Schlamminger S, Gundlach J H and Adelberger E G 2012 Torsion-balance tests of the weak equivalence principle *Class. Quantum Grav.* **29** 184002
[138] Wagman M 2020 private communication
[139] Rinaldi E, Syritsyn S, Wagman M L, Buchoff M I, Schroeder C and Wasem J 2019 Neutron–antineutron oscillations from lattice QCD *Phys. Rev. Lett.* **122** 162001
[140] Rinaldi E, Syritsyn S, Wagman M L, Buchoff M I, Schroeder C and Wasem J 2019 Lattice QCD determination of neutron–antineutron matrix elements with physical quark masses *Phys. Rev.* D **99** 074510
[141] Buchoff M I and Wagman M 2016 Perturbative renormalization of neutron–antineutron operators *Phys. Rev.* D **93** 016005
Buchoff M I and Wagman M 2018 *Phys. Rev.* D **98** 079901 (erratum)
[142] Buchoff M I and Wagman M 2015 Neutron–antineutron operator renormalization *PoS LATTICE2014* p 290 arXiv:1502.00044 [hep-lat]
[143] Dev B 2020 private communication
[144] Nesvizhevsky V, Gudkov V, Protasov K, Snow W and Voronin A Y 2019 Experimental approach to search for free neutron–antineutron oscillations based on coherent neutron and antineutron mirror reflection *Phys. Rev. Lett.* **122** 221802
[145] Kerbikov B O 2019 The effect of collisions with the wall on neutron–antineutron transitions *Phys. Lett.* B **795** 362–5
[146] Chetyrkin K, Kazarnovsky M, Kuzmin V and Shaposhnikov M 1980 Neutron–antineutron oscillations *Pisma Zh. Eksp. Teor. Fiz.* **32** 88–91
[147] Chetyrkin K G, Kazarnovsky M V, Kuzmin V A and Shaposhnikov M E 1981 Neutron–antineutron oscillations: how fast could they be? *Phys. Lett.* B **99** 358–60

[148] Golub R and Yoshiki H 1989 Ultracold antineutrons (UCN-bar). 1: the approach to the semiclassical limit *Nucl. Phys.* A **501** 869–76
[149] Yoshiki H and Golub R 1992 Ultracold antineutrons (UC antineutrons). 2: production probability under magnetic and gravitational fields *Nucl. Phys.* A **536** 648–68
[150] Protasov K, Gudkov V, Kupriyanova E A, Nesvizhevsky V, Snow W and Voronin A Y 2020 Theoretical analysis of antineutron-nucleus data needed for antineutron mirrors in neutron–antineutron oscillation experiments *Phys. Rev.* D **102** 075025
[151] Glashow S L 1986 Positronium versus the mirror universe *Phys. Lett.* B **167** 35–6
[152] Carlson E D and Glashow S L 1987 Nucleosynthesis versus the mirror universe *Phys. Lett.* B **193** 168–70
[153] Gninenko S N 1994 Limit on 'disappearance' of orthopositronium in vacuum *Phys. Lett.* B **326** 317–9
[154] Berezhiani Z 1998 Unified picture of the particle and sparticle masses in SUSY GUT *Phys. Lett.* B **417** 287–96
[155] Belfatto B and Berezhiani Z 2019 How light the lepton flavor changing gauge bosons can be *Eur. Phys. J.* C **79** 202
[156] Belfatto B, Beradze R and Berezhiani Z 2020 The CKM unitarity problem: a trace of new physics at the TeV scale? *Eur. Phys. J.* C **80** 149
[157] Foot R 2004 Mirror matter-type dark matter *Int. J. Mod. Phys.* D **13** 2161–92
[158] Addazi A, Berezhiani Z, Bernabei R, Belli P, Cappella F, Cerulli R and Incicchitti A 2015 DAMA annual modulation effect and asymmetric mirror matter *Eur. Phys. J.* C **75** 400
[159] Cerulli R, Villar P, Cappella F, Bernabei R, Belli P, Incicchitti A, Addazi A and Berezhiani Z 2017 DAMA annual modulation and mirror dark matter *Eur. Phys. J.* C **77** 83
[160] Mohapatra R N, Nasri S and Nussinov S 2005 Some implications of neutron mirror neutron oscillation *Phys. Lett.* B **627** 124–30
[161] Pokotilovski Y N 2006 On the experimental search for neutron $\rightarrow$ mirror neutron oscillations *Phys. Lett.* B **639** 214–7
[162] Berezhiani Z, Frost M, Kamyshkov Y, Rybolt B and Varriano L 2017 Neutron disappearance and regeneration from mirror state *Phys. Rev.* D **96** 035039
[163] Berezhiani Z and Lepidi A 2009 Cosmological bounds on the 'millicharges' of mirror particles *Phys. Lett.* B **681** 276–81
[164] Vigo C, Gerchow L, Radics B, Raaijmakers M, Rubbia A and Crivelli P 2020 New bounds from positronium decays on massless mirror dark photons *Phys. Rev. Lett.* **124** 101803
[165] Ignatiev A Y and Volkas R R 2000 Geophysical constraints on mirror matter within the earth *Phys. Rev.* D **62** 023508
[166] Berezhiani Z 2016 Anti-dark matter: a hidden face of mirror world (arXiv:1602.08599 [astro-ph.CO])
[167] Berezhiani Z, Dolgov A D and Tkachev I I 2013 Dark matter and generation of galactic magnetic fields *Eur. Phys. J.* C **73** 2620
[168] Sharma N, Dahiya H, Chatley P K and Gupta M 2010 Spin $\frac{1}{2}^+$, spin $\frac{3}{2}^+$ and transition magnetic moments of low lying and charmed baryons *Phys. Rev.* D **81** 073001
[169] Broggini C, Giunti C and Studenikin A 2012 Electromagnetic properties of neutrinos *Adv. High Energy Phys.* **2012** 459526
[170] Berezhiani Z 2020 A possible shortcut for neutron–antineutron oscillation (arXiv:2002.05609 [hep-ph])
[171] Golubeva Y S and Kondratyuk L A 1997 Annihilation of low energy antineutrons on nuclei *Nucl. Phys.* B **56** 103–7
[172] Golubeva E S, Barrow J L and Ladd C G 2019 Model of $\bar{n}$ annihilation in experimental searches for $\bar{n}$ transformations *Phys. Rev.* D **99** 035002
[173] Minor E D, Armstrong T A, Bishop R, Harris V, Lewis R A and Smith G A 1990 Charged pion spectra and energy transfer following antiproton annihilation at rest in carbon and uranium *Z. Phys.* A **336** 461–8
[174] Mcgaughey P L *et al* 1986 Dynamics of low-energy antiproton annihilation in nuclei as inferred from inclusive proton and pion measurements *Phys. Rev. Lett.* **56** 2156–9
[175] Baldo-Ceolin M *et al* 1990 A new experimental limit on neutron–antineutron transitions *Phys. Lett.* B **236** 95–101
[176] Bryman D 2014 Two nucleon ($B - L$)-conserving reactions involving tau leptons *Phys. Lett.* B **733** 190–2

[177] Takhistov V *et al* (Super-Kamiokande Collaboration) 2015 Search for nucleon and dinucleon decays with an invisible particle and a charged lepton in the final state at the Super-Kamiokande experiment *Phys. Rev. Lett.* **115** 121803
[178] Girmohanta S and Shrock R 2019 Improved lower bounds on partial lifetimes for nucleon decay modes *Phys. Rev.* D **100** 115025
[179] Tanabashi M *et al* (Particle Data Group Collaboration) 2018 Review of particle physics *Phys. Rev.* D **98** 030001
[180] Peggs S *et al ESS Technical Design Report* ESS-DOC-274 ESS Lund University 2013 https://europeanspallationsource.se/documentation/tdr.pdf
[181] Santoro V *et al* 2016 Neutronic design of the bunker *ESS General Document, ESS-0052649* ESS, Lund University
[182] Andersen K *et al* 2018 The ESS instrument suite, a capability gap analysis https://europeanspallationsource.se/instruments/capability-gap-analysis
[183] Zanini L, Andersen K H, Batkov K, Klinkby E B, Mezei F, Schönfeldt T and Takibayev A 2019 Design of the cold and thermal neutron moderators for the European Spallation Source *Nucl. Instrum. Methods Phys. Res.* A **925** 33–52
[184] Andersen K H, Bertelsen M, Zanini L, Klinkby E B, Schönfeldt T, Bentley P M and Saroun J 2018 Optimization of moderators and beam extraction at the ESS *J. Appl. Crystallogr.* **51** 264–81
[185] CORDIS HighNESS https://cordis.europa.eu/project/id/951782
[186] Santoro V *et al* 2020 Development of high intensity neutron source at the European Spallation Source *J. Neutron Res.* **22** 209–19
[187] Klinkby E, Batkov K, Mezei F, Schønfeldt T, Takibayev A and Zanini L 2014 Voluminous D2 source for intense cold neutron beam production at the ESS (arXiv:1401.6003 [physics.ins-det])
[188] Nielsen T R, Markvardsen A J and Willendrup P K 2016 McStas and Mantid integration (arXiv:1607.02498 [physics.ins-det])
[189] Broussard L J *et al* 2017 New search for mirror neutrons at HFIR *Proc., Meeting of the APS Division of Particles and Fields (DPF 2017): Fermilab* (Batavia, Illinois, USA 31 July–4 August 2017) arXiv:1710.00767 [hep-ex]
[190] Snow W M *et al* 2015 A slow neutron polarimeter for the measurement of parity-odd neutron rotary power *Rev. Sci. Instrum.* **86** 055101
[191] Abel C *et al* 2018 Statistical sensitivity of the *n*EDM apparatus at PSI to neutron mirror-neutron oscillations *Int. Workshop on Particle Physics at Neutron Sources 2018 (PPNS 2018)* (Grenoble, France 24–26 May 2018) arXiv:1811.01906 [nucl-ex]
[192] Broussard L J *et al* 2019 New search for mirror neutron regeneration *EPJ Web Conf.* **219** 07002
[193] Altarev I *et al* 2015 A large-scale magnetic shield with 10^6 damping at mHz frequencies *J. Appl. Phys.* **117** 183903
[194] Frost M J 2019 Searching for baryon number violation at cold neutron sources *PhD Thesis* University of Tennessee https://trace.tennessee.edu/utk_graddiss/5951
[195] Waters L S, McKinney G W, Durkee J W, Fensin M L, Hendricks J S, James M R, Johns R C and Pelowitz D B 2007 The MCNPX Monte Carlo radiation transport code *AIP Conf. Proc.* **896** 81–90
[196] Kamyshkov Y 1995 Use of a cold source and large reflector mirror guide for a neutron–antineutron oscillation search *Proc. of the ICANS-XIII Meeting* (Villigen: PSI)
[197] Mezei F 1976 Novel polarized neutron devices: supermirror and spin component amplifier *Commun. Phys.* **1** 81–5
[198] Institut Laue-Langevin 2008 *ILL Yellow Book*
[199] Bergmann R M, Filges U, Kiselev D, Klauser C, Rantsiou E, Talanov V, Wohlmuther M and Yamada M 2018 Simulation methods and results of the SINQ cold neutron source upgrade study *J. Phys.: Conf. Ser.* **1021** 012081
[200] Muhrer G, Schönfeldt T, Iverson E B, Mocko M, Baxter D V, Hügle T, Gallmeier F X and Klinkby E B 2016 Demonstration of a single-crystal reflector-filter for enhancing slow neutron beams *Nucl. Instrum. Methods Phys. Res.* A **830** 454–60
[201] Sato T *et al* 2013 Particle and heavy ion transport code system, phits, version 2.52 *J. Nucl. Sci. Technol.* **50** 913–23
[202] Korneev D A, Pasyuk V V, Petrenko A V and Jankovski H 1992 Absorbing sublayers and their influence on the polarizing efficiency of magnetic neutron mirrors *Nucl. Instrum. Methods Phys. Res.* B **63** 328

[203] Nikova E S, Salamatov Y A, Kravtsov E A, Bodnarchuk V I and Ustinov V V 2019 Experimental determination of gadolinium scattering characteristics in neutron reflectometry with reference layer *Physica* B **552** 58
[204] Agostinelli S *et al* (GEANT4 Collaboration) 2003 GEANT4: a simulation toolkit *Nucl. Instrum. Methods Phys. Res.* A **506** 250–303